HIGH STRAIN RATE STUDIES OF ARMOR MATERIALS

By

Ghaznafar Mohamed Nazimuddin

A Thesis submitted to the Faculty of Graduate Studies of

The University of Manitoba

in partial fulfillment of the requirements of the degree of

MASTER OF SCIENCE

Department of Mechanical and Manufacturing Engineering

University of Manitoba

Winnipeg, Manitoba

ABSTRACT

This thesis focuses on the high strain rate behavior of Maraging steel 300, High Hardness Armor (HHA) and Aluminum 5083 – H131 Alloy. These materials are used by the Department of National Defense (DND) of Canada as armor plate materials in military applications. The aim of the research is to investigate the dynamic shear-strain response of these armor materials at high strain rate loading to study the occurrence of Adiabatic Shear Bands and the subsequent failure. The effects of impact momentum and strain rates on the dynamic stress-strain curve and on the adiabatic shear failure of these armor materials under impact and torsion loading need to be investigated to evaluate their capability to withstand military conditions.

Specimens of these materials were subjected to direct impact and torsion loading using the Split Hopkinson Pressure Bar (SHPB) – Direct Impact and Torsion Split Hopkinson Bar (TSHB) respectively. The dynamic stress-strain curves were generated to study the plastic deformation behavior during impact and torsion loading. High strain rate loading affects the mechanical properties in a wide range of metals and alloys by thermo-mechanical instability. A phenomenon called Adiabatic Shear Bands (ASBs) occurs due to extreme strain localization as a result of thermo-mechanical instability in the microstructure at high strain rate loading conditions. The presence of ASBs acts as a precursor to failure as they are harder and more brittle than the bulk material.

The impact loading experiments involved striking cylindrical specimens at very high impact momentum using a projectile. The strain rates achieved on impact of a specimen is a function of impact momentum. The influence of strain rate and impact

momentum on the occurrence of ASBs in the materials of interest was investigated. Microstructural evaluation of these armor materials showed that the formation of ASB requires a threshold level of impact momentum. ASBs in the form of white-etching bands and deformed bands at its tail end were observed in Maraging steel 300 subjected to an impact momentum of 44.54 kg.m/s. On the other hand, deformed bands were observed in HHA specimens subjected to an impact momentum between 32.91 kg.m/s and 45.49 kg.m/s. Deformed bands were also visible in Aluminum 5083 – H131 Alloy specimens subjected to impact loading. The deformed bands in aluminum were governed by plastic flow due to thermal softening.

Thin-walled tube specimens of Aluminum 5083 – H131 Alloy and Maraging steel 300 were subjected to 4°, 6° and 8° angles of twist using the TSHB. Deformed ASBs accompanied by cracks were found in aluminum subjected to 8° angles of twist. On the other hand, ASBs were not visible in Maraging steel 300 and the specimens failed at high angles of twist.

The mechanisms for the occurrence of ASB in steels and aluminum are presented in this thesis. Optical, Scanning Electron Microscopy (SEM) and Atomic Force Microscopy (AFM) were used. The utilization of AFM to study the characteristic of the white-etching band in Maraging steel 300 provides information on the atomistic evolution of ASBs and it is also discussed in this thesis. The dynamic stress-strain response from impact and torsion loading experiments supplemented with microstructural investigation form a basis for evaluation of the resistance of these materials to high strain rate loading conditions.

ACKNOWLEDGEMENTS

I would like to express my heartfelt gratitude and thanks to my advisor, Professor M. Nabil Bassim for giving me the opportunity to pursue my graduate studies. I am grateful to Professor Bassim who has enriched the knowledge of materials science through his teaching during my undergraduate and graduate days. This thesis has been made a possibility through his valuable guidance, support and understanding over the many challenges that I had to overcome. My appreciation and gratitude goes to the Department of National Defense, for sponsoring the research and providing research assistantship during my second year of graduate studies.

I would also like to extend my sincere thanks to Dr. Akindele Odeshi for his support and valuable advice during my graduate studies. My appreciation also goes to Dr. Akindele Odeshi and Mr. J. P. Burak for their time, support and technical expertise in conducting the research experiments. I am very grateful to Dr. Douglas Thomson and Mr. Dwayne Chrusch for their guidance and help in using the Atomic Force Microscopy and Nano Systems Fabrication Laboratory. I would like to thank my examiners, Dr. Douglas Thomson and Dr. Olanrewaju Ojo for their time as committee members.

This journey to acquire knowledge and education has been a possibility through the immense support by my father, Dr. AV. M. Nazimuddin and my mother, Mrs. Rukhsana Nazimuddin. Their constant motivation, love and encouragement gave me the strength and enthusiasm to make all things possible. I couldn't have achieved my engineering education without their unconditional love and support.

Lastly, I would also like to thank the department technicians, office support staff and my friends, Mr. Ian Polyzois and Ms. Sahar Mirfakhraei for their support in this work.

TABLE OF CONTENTS

TABLE OF FIGURES

LIST OF TABLES

CHAPTER ONE: INTRODUCTION

High strain rate investigations of materials using the Split Hopkinson Bar deal with strain rates in the range of 10^3 s^{-1} to 10^4 s^{-1}. The strains and strain rates are large enough to cause plastic deformation and subsequent fracture that is different from quasi-static loading conditions. Plastic deformation of many metallic materials at high strain rate produces localised shear strain within a narrow region in a material. These regions of extreme strain localization are called Adiabatic Shear Bands (Bassim 2001). The presence of Adiabatic Shear Bands (ASBs) is considered undesirable as they are microstructural defects that lead to failure at high loading rates. Adiabatic shear bands have been identified in a variety of materials including steel and aluminum alloys that are commonly used in service for many engineering applications.

The heat generated as a result of plastic deformation is retained in narrow regions in the material. The term adiabatic heating is referred to the entrapment of heat that leads to a significant rise in temperature and causes mechanical instability in the microstructure. The thermal softening effect in the microstructure leads to stress collapse in the material and contributes to extreme strain localization in the narrow regions. These narrow bands are referred in the literature as either deformed bands or white-etching bands (transformed bands by some authors). The appearance of deformed bands consists of highly distorted and elongated grains in the microstructure than the rest of the bulk material. The white-etching bands when viewed under an optical microscope appear as a fine and narrow white region. Several researchers have attributed the appearance of white in the band as due to the phase transformation of austenite to untempered martensite. The

characteristics of ASB are generally associated with increased hardness than the surrounding material and thus a material becomes brittle at high loading rates.

High strain rate loading conditions are often encountered in high velocity projectile impact and plate used for armor protection in military vehicles. It is very important to make design consideration for materials used in such tough service conditions. There are many factors that affect the formation of ASB that includes strain rate exponent, strain rate sensitivity, hardness, microstructure and presence of imperfections such as precipitates and inclusion (Bassim and Odeshi 2007). Therefore, understanding these material variables is crucial to better mechanical design of materials used in military applications.

This investigation focuses on three materials provided by the Department of National Defense, Defence Research and Development Canada (DRDC) Valcartier, to evaluate the dynamic mechanical response at high strain rate loading. These armor materials: Maraging steel 300 (Mars 300), High Hardness Armor (HHA) and Aluminum 5083 – H131 Alloy, are used as armor plate protection in combat vehicles in the military. The objective of this thesis is to investigate the behavior of these materials at high strain rate loading conditions similar to those experienced in defense conditions and to study the factors that contribute to the formation of ASB and occurrence of failure.

CHAPTER TWO: LITERATURE REVIEW

2.1 Strength of Materials

A material under an applied stress may undergo elastic followed by plastic deformation. In elastic deformation, the change in geometry of the material is momentary when the stress is removed. With respect to the atomic interface, a material undergoing elastic deformation causes atoms to vibrate and move from their original position. When the applied stress is removed, atoms return to their initial position thereby maintaining their shape and geometry. On an atomic scale, macroscopic elastic strain is manifested as small changes in the interatomic spacing and the stretching of interatomic bonds (Callister 2003). For a material undergoing plastic deformation, the applied stress is large enough to break the bonds in their atomic arrangement. Upon removal of the applied stress, the material does not revert back to its original shape. In plastic deformation, the change in geometry is permanent as the atoms rearrange in their new atomic positions.

During a quasi-static tension loading, a brittle material, on reaching its ultimate stress, fractures as the load carrying capacity of the material is exceeded. A brittle material does not show any warning in the form of plastic deformation and fails at its yield point. For brittle materials, localized stresses continue to build up leading to stress concentration with the absence of local yielding (Dieter 1976). However, even if no stress concentration is present, fracture would occur when the yield stress and tensile strength is practically identical (Dieter 1976). Most materials having a Body-Centered Cubic (BCC) or Face-Centered Cubic (FCC) structure exhibit some ductility when undergoing quasi-static loading. The deformation process in ductile materials is governed by an initial

elastic deformation followed by plastic deformation based on the applied stress. From a stress-strain curve point of view, there are three distinctive regions: Elastic region, Strain hardening and Plastic deformation, followed by necking and stress collapse leading to failure.

When a material is subjected to high strain rate loading, it initially exhibits strain hardening as a result of adiabatic heating in a localized region. Adiabatic heating promotes loss in strength as softening of material becomes greater than strain hardening. The competition between strain hardening and thermal softening leads to thermo-mechanical instability in the microstructure. Zener and Hollomon brought into focus the concept of adiabatic heating resulting in strain localization that contributes to the formation of narrow regions called shear bands at high strain rate deformation ((Al-Ameeri 2005, Schoenfeld and Wright 2003, Zener and Hollomon 1944). For many years, there has been considerable interest to understand the capabilities of materials in various applications such as high speed bullet penetration, ballistic impact, high speed machining and blanking operations and so on. Microstructural evolution due to high strain rates are a major factor in the formation of shear bands that act as a precursor to failure.

This image has been removed due to copyright issues. Refer to its source.

Figure 2.1: Schematic representations of tensile stress-strain behaviour for brittle and ductile materials loaded to fracture (Callister 2003)

2.2 The Phenomenon of Adiabatic Shear Bands

Materials subjected to high strain rates produce regions of extreme localized deformation called Adiabatic Shear Bands (ASBs). The term ‘adiabatic’ in adiabatic heating refers to excess heat that is generated than it is conducted away from the material. Thermo-mechanical instability arises due to the extreme heat generated in a localised region and does not have enough time for the heat to be conducted away from the local region. The heat is trapped in the region causing a rise in temperature and softens the material thermally that in turn leads to strain localization in the material. Adiabatic shear bands affect the mechanical properties in a material and become a source for crack initiation and propagation during mechanical loading.

Investigation by Marchand and Duffy shows that high strain rate plastic deformation occurs in three stages (Marchand and Duffy 1988). The first stage is referred to as the homogenous strain state which begins after yield point. The second stage is the competition between strain hardening and thermal softening and is referred to as an inhomogeneous strain state. In the final stage, extreme localisation of strain to fine narrow bands has been reported (Marchand and Duffy 1988).

The third stage of plastic deformation is also referred to as the stress collapse and is attributed to the state of thermo-mechanical instability in the material (Schoenfeld and Wright 2003, Marchand and Duffy 1988, Wright and Walter 1987, Wright 1987). Strain localisation and stress collapse occurring in a material due to rapid deformation occur in the most important non homogeneous section in a material structure (Schoenfeld and

Wright 2003). Feng and Bassim (1999) also suggested that the presence of geometrical imperfection in a material could promote the initiation of ASBs.

Figure 2.2: The three stages of deformation at high strain rate (Bai and Dodd 1992)

Figure 2.3 shows the condition for isothermal, adiabatic and localization behavior in a stress versus nominal plastic strain curve (Schoenfeld and Wright 2003). Plastic deformation at low strain rates causes the material to harden as the strain keeps increasing and therefore strain hardening effects dominates in the isothermal condition. During high strain rate plastic deformation, strain hardening effects dominate the deformation process till the material experiences the maximum flow stress at γ_{max} stress. The effect of thermal softening dominates the deformation process beyond the maximum flow stress and flow stress decreases with increasing strain. Thermal softening may continue indefinitely for a material with uniform distribution of stress, strain and temperature (Schoenfeld and Wright 2003). However, most materials have non uniformities that could lead to stress collapse, strain localization and formation of ASBs (Schoenfeld and Wright 2003).

This image has been removed due to copyright issues. Refer to its source.

Figure 2.3: Typical response to plastic deformation (Schoenfeld and Wright 2003)

2.3 Characteristics of Adiabatic Shear Bands

Marchand and Duffy (1988) have shown that plastic deformation at high strain rates causes heat generation to rise the local temperature to several hundred degrees in the material. The flow stress is dependent on the temperature rise and further increase in temperature during deformation lowers the flow stress. There are two distinctive types of ASBs that are identified in metallic materials: Deformed bands and Transformed bands (see Figure 2.4). The deformed bands are narrow bands and appear similar to the bulk material. They are described as a region of intense plastic deformation in a form of flow localization caused by weakening effects of thermal softening (Bai and Dodd 1992). The deformed bands consist of highly distorted and elongated grains running parallel to the direction of applied stress (see Figure 2.5) (Mirfakhraei 2008).

Deformed bands are visible in Face Centered Cubic (FCC) materials such as aluminum and in denser metals Body Centered Cubic (BCC) materials such as steel. There is a possibility for the formation of single or multiple shear bands depending on the nucleation sites. Multiple shear bands spread homogeneously across the material when there is more than one nucleation site within close proximity. Factors affecting nucleation sites are phase boundaries of two dissimilar phases, precipitates, thin sections on the sample, presence of voids and machining scratches. Studies have shown the presence of deformed bands in regions ahead of the tail ends of white transformation bands (Bassim, Odeshi and Al-Ameeri, et al. 2005).

The transformed bands appear differently than the bulk material and have a distinctive white appearance on the sample when viewed with an aid of an optical microscope. The phase transformation from austenite to untempered martensite during

adiabatic heating presents the prominent white color in appearance and is also referred to as the white etching bands (Glenn and Leslie 1971). A Transmission Electron Microscopy (TEM) study by Derep (1987) shows that the microstructure of transformed bands in armored steel consists of very fine martensites, iron carbides and ferrites with grains size below 300 nm. Zurek (1994) also suggested that the appearance of white-etching bands in steels is due to the resolution limit of optical microscopy in resolving the fine nano substructures in shear bands.

Meyers et al (2003) studied the microstructural evolution in stainless steels at high strain rates and revealed that shear bands are comprised of two regions; firstly a region of ultra fine grains (0.1 – 0.2 μm) with well defined grain boundaries and dislocations, and secondly a region of glassy structure (solid state amorphitization). In their study Meyers et al (2003) also revealed that at high strain rates, microstructural evolution begins with homogeneous distribution of dislocations. These dislocations rearrange themselves into dislocation cells and eventually become elongated subgrains, following which they are sub-divided into equiaxed grains as the strain increases.

Figure 2.4: The effect of tempering temperature on formation of ASBs in oil-quenched AISI 4340 steel (Odeshi, Al-Ameeri and Mirfakhraei, et al. 2006, Al-Ameeri 2005)

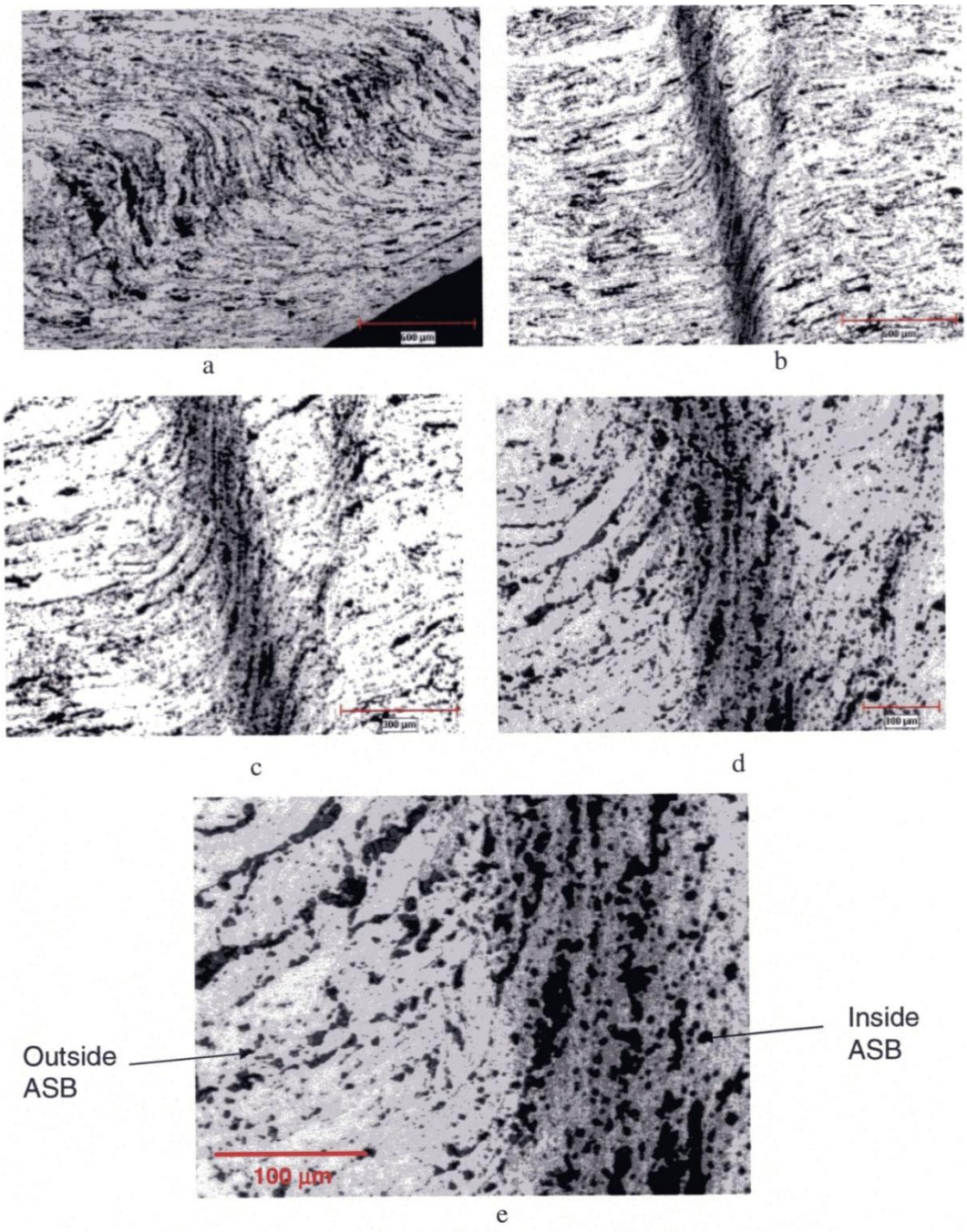

Figure 2.5: Optical micrographs showing ASBs along transverse section of Aluminum 5083 H131 alloy impacted at 40.1 kg.m/s (Mirfakhraei 2008)

Image reproduced with permission from Sahar Mirfakhraei, April 7, 2010.

2.4 Initiation and Propagation Mechanism of Adiabatic Shear Bands (ASBs)

Microstructural analysis of ASBs brings into understanding the complex mechanism of initiation and propagation of shear bands in a material. Figure 2.6 shows possible shear band initiation mechanism such as (a) grain size inhomogeneity, (b) geometrical softening, (c) Peirce-Asaro-Needleman texture localisation (Peirce, Asaro and Needleman 1984), and (d) dislocation pile-up release. Under dynamic loading, the larger grains may be more susceptible to deformation and act as initiation sites as they exhibit a lower yield than smaller grains. Crystallographic rotation of grains cause geometrical softening leading to localised softening and initiation of shear bands (Li, et al. 2006, Nesterenko, Meyers and Wright 1998). The localised deformation of a grain can result in extended strain localised band through cooperative plastic deformation of grains. This mechanism was proposed by Peirce et al. (1984), Anand and Kalinidi (1994) and further reviewed by Nesterenko et al. (1998). The fourth mechanism was proposed by Armstrong and Zerilli (1994) that a dislocation pile-up can pierce through a grain boundary, causing a local rise in temperature and softening. It is schematically presented in Figure 2.6 (d) by Nesterenko et al (1998).

Feng and Bassim (1999) predicted the occurrence of ASB in high strength low alloy steel through finite element modeling. The material deforms in three stages where there is no plastic deformation during the initial stage. The competition between strain hardening and thermal softening governs the second stage. In the final stage, thermal softening dominates the deformation process leading to stress collapse, strain localisation and formation of ASB (Dao and Schockey 1979).

This image has been removed due to copyright issues. Refer to its source.

Figure 2.6: Possible shear-band initiation mechanism in single-phase homogeneous materials. (a) Grain size inhomogeneity, (b) Geometrical softening, (c) Peirce-Asaro-Needleman textural localisation (d) Dislocation pile-up release (Nesterenko, Meyers and Wright 1998)

Odeshi et al. (2005) also stated that the flow stress increases with strain and strain hardening effects dominate the deformation process till the maximum flow stress is reached. On reaching the maximum flow stress, thermal softening dominates the process that causes the stresses to decrease with an increase in strain. Shear bands begin to form as a result of the thermo-mechanical instability during stress collapse and strain localization on reaching the critical strain.

Mishra et al. (2005) investigated the microstructural evolution during severe plastic deformation. Figure 2.7 shows the sequence of the formation of ultrafine grains. Initially, there is a homogeneous distribution of high dislocation density and formation of twins (Figure 2.7a). The grouping of dislocation begins to form sub-grains as seen in Figure 2.7b. The reorientation of cell wall acts as a barrier for propagation of dislocation motion (Figure 2.7c). This increases the formation of elongation sub-grains (Figure 2.7d). In the last stage, the reorientation of sub-grains and boundaries produces ultrafine grain size (Figure 2.7e).

Recent investigation by Bassim et al. (2005) reveals that two cones that are mirror images of one another are formed by the dynamically propagating adiabatic shear bands in the samples. It has been reported that cracks initiate and propagate along the one conical shaped shear band and penetrate through the matrix to the other cone resulting in shear failure along planes that are inclined at an angle of about 45° to the direction of applied stress. The presence of shear bands on the surface creates a site for micro voids that coalesce, become large and develop into a crack.

Figure 2.7: Schematic representation of evolution of microstructure during plastic deformation: (a) Homogeneous distribution of dislocation (b) elongated cell formation (c) Hindrance by sub-grain boundaries for dislocation motion (d) division of elongated sub-grains (e) reorientation of sub-grains and formation of ultrafine grain size (Mishra, et al. 2005)

Figure 2.8: The fracture path in samples subjected to impact loading (Odeshi, Al-Ameeri and Mirfakhraei, et al. 2006)

Figure 2.9: Longitudinal section of an impacted sample showing the two cones formed by adiabatic shear bands (Bassim, Odeshi and Al-Ameeri, et al. 2005)

2.5 Factors Influencing the Formation of Adiabatic Shear Bands (ASBs)

There are several factors that contribute to the formation of ASBs in materials. Various parameters such as loading conditions, material microstructure, heat capacity, heat conductivity, strength level, geometry, defects and effects of strain rate are some important conditions that affect the mechanism behind ASBs (Zhang, et al. 1998, Bassim 2001, Hartley, Duffy and Hawley 1987). Materials with low strain hardening coefficient, low strain-rate sensitivity, low thermal conductivity, high thermal softening and high strength/ hardness value are more susceptible to form ASBs (Zurek 1994, Hartley, Duffy and Hawley 1987). It was also reported by Feng and Bassim (1999) that the presence of microstructural imperfections, inclusions or geometrical defects propagate the formation of ASBs.

Armstrong and Zerilli (1994) reported that a local rise in temperature and softening produces dislocation pile-ups that penetrate through grain boundaries and thereby creating an initiation site for shear bands. The role of microstructure is very significant in the formation of ASBs during high strain rate deformation. An investigation by Zhang et al (1998) also reveals that the formation of adiabatic shear bands during ballistic impact loading appear more readily in tempered martensite than austenitic microstructures.

Recent studies by Odeshi et al. (2006) confirmed the formation of ASB in heat treated AISI 4340 steel samples. Quench-hardened steel samples tempered at 300 °C and 400 °C have been reported to show white-etching bands and in samples tempered above 500 °C formed deformed bands (Al-Ameeri 2005).

Stacking Fault Energy (SFE) contributes to the formation of ASBs in Face Centered Cubic (FCC) materials. It has been stated that in materials with low SFE, cross-slip dislocations are difficult due to partial dislocations that are widely separated with their recombination onto the new slip plane requires considerable energy (Vecchio and Hertzberg 1988). When the SFE is large, partial dislocations are closer together and recombine readily to form cross-slip. Thus a material with high SFE contributes to multiple cross-slips which in turn increase the possibility of more deformed bands. The study by Vecchio and Hertzberg (1988) shows that decreasing SFE reduces the size and extent of microvoids as a result of restricted dislocation motion.

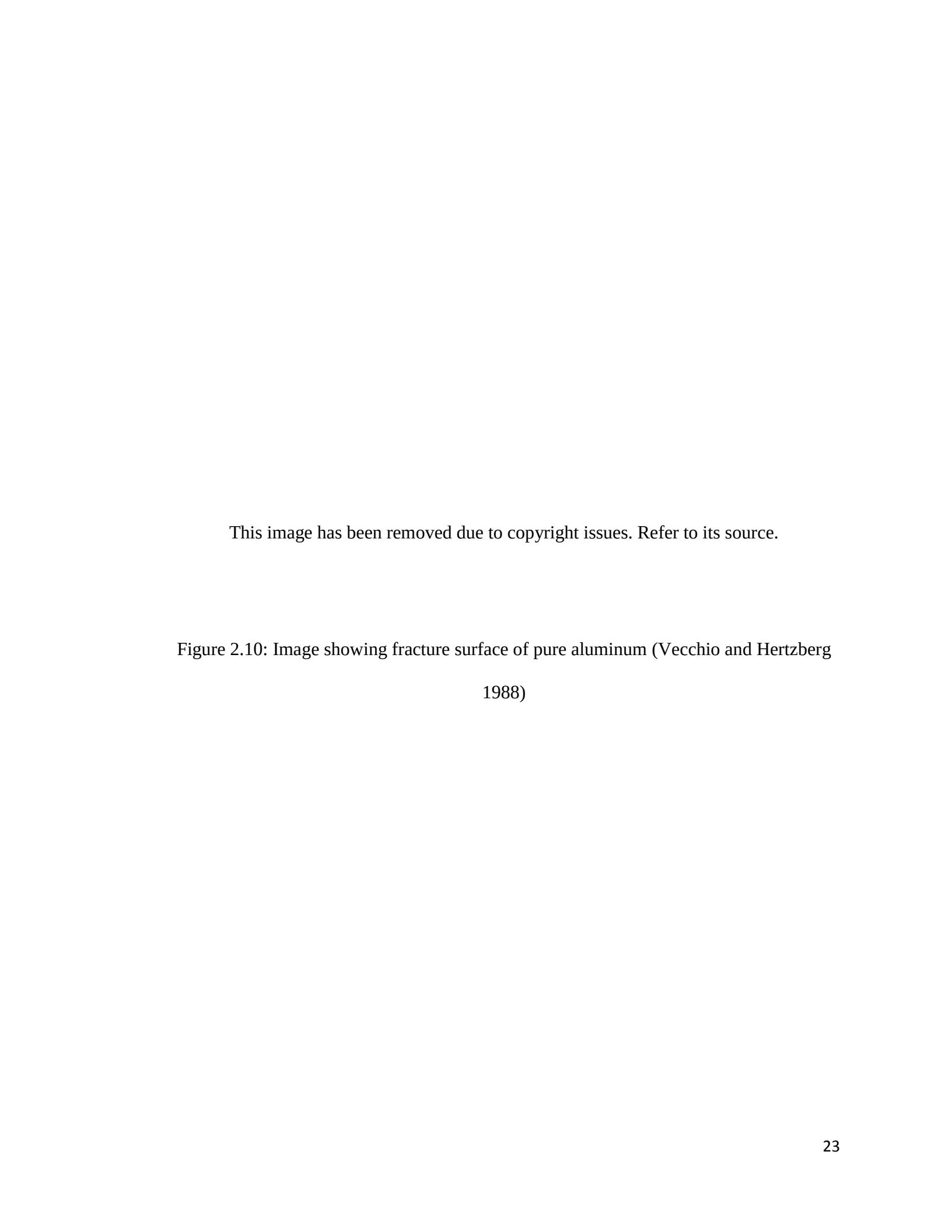

Figure 2.10: Image showing fracture surface of pure aluminum (Vecchio and Hertzberg 1988)

2.6 Failure of the Material

The presence of ASBs in a material is an undesirable state as they act as preferential sites for failure, either by ductile void nucleation followed by growth and coalescence, or by crack growth. Understanding the behavior of the microstructure is important in high strain rate studies to better design armor applications. It has been reported that ductile fracture occurs when the ASB was hot, i.e. during the formation of ASB; whereas brittle fracture occurs in the cool band, after deformation (Bai and Dodd 1992). In general, ductile materials are associated with formation of voids and susceptible to develop cracks more often with brittle materials.

Investigation by Xue et al (2002) on the damage evolution within shear bands in Ti-6Al-4V alloy shows that void evolution occurs in three stages (Figure 2.11). Initially, the void nucleates within a shear band and grows continuously into the surrounding matrix. The second stage is characterised by elongation of void and rotation along the direction of shear band. During the final stages, the voids coalesce and result in the formation of cracks. Investigation by Meyers and Wittman (1990) shows that the failure of quenched and tempered AISI 8620 steel under ballistic impact resulted in fracture of sample due to shear bands.

From the study by Lach and Nahme (1997), it was found that Maraging steel 300 specimen contained a high density of adiabatic shear bands within the fractured zone. Lach and Nahme (1997) reported that the presence of cracks and shear bands is the result of the complex stress distribution within the areas near the sample edge or the fractured surface. Figure 2.13 shows the presence of cracks running parallel to the loading direction and is accompanied by shear failure (Lach and Nahme 1997).

Figure 2.11: Image showing void nucleation and growth within a shear band in Ti-6Al-4V alloy (a) nucleation of void, (b) growth of voids, (c) elongation and rotation of voids, (d) coalescence of voids to form crack (Xue, Nesterenko and Meyers 2002)

Figure 2.12: Representation of ballistic impact damage (Meyers and Wittman 1990)

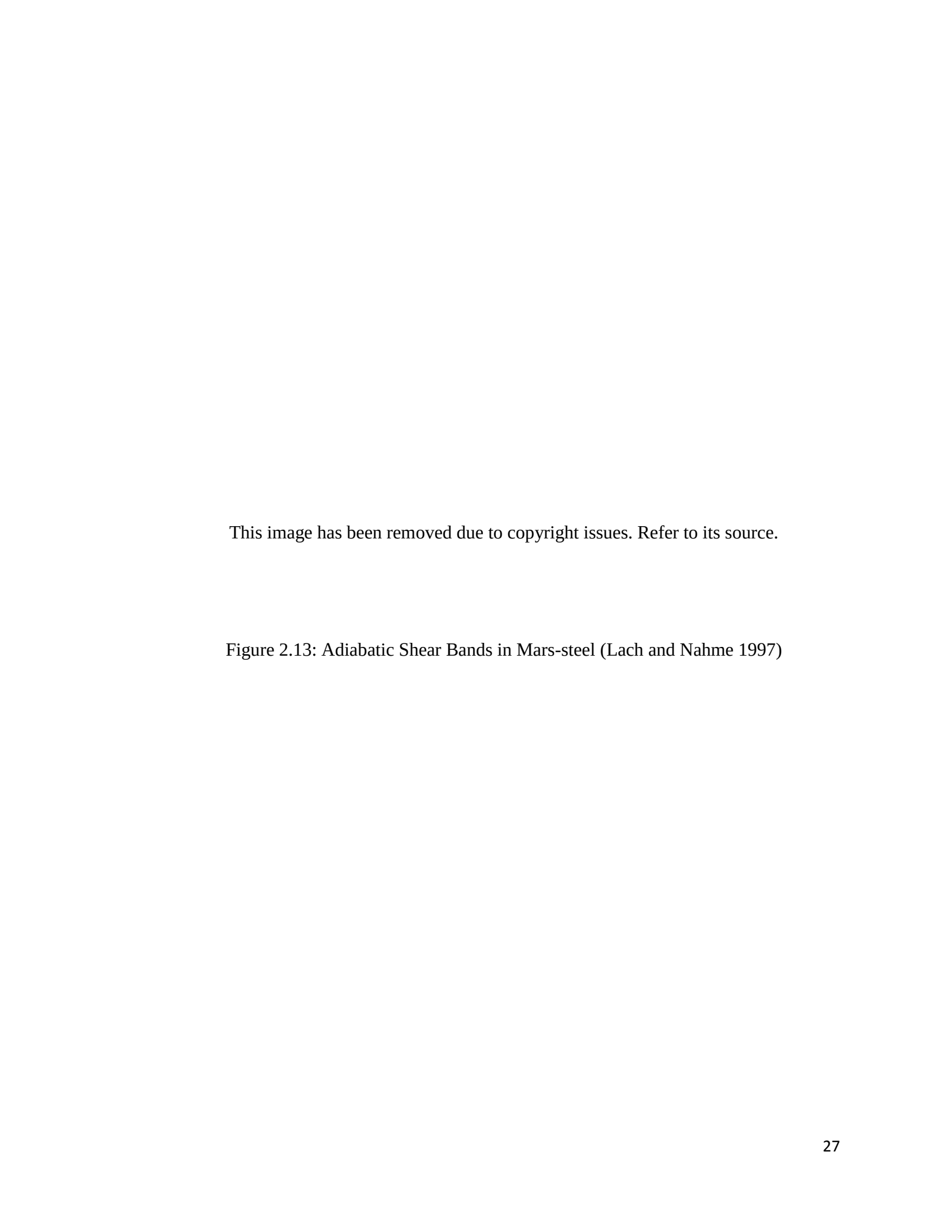

Figure 2.13: Adiabatic Shear Bands in Mars-steel (Lach and Nahme 1997)

CHAPTER THREE: EXPERIMENTAL PROCEDURES

3.1 Introduction

This section focuses on:

- Materials investigated in this thesis
- The geometry of the specimens
- Use of the Split Hopkinson Pressure Bar – Direct (Impact loading)
- Use of the Torsional Split Hopkinson Bar (Torsion loading)
- Preparation of specimen for microstructural analysis
- Microstructural analysis using
    - Optical Microscopy
    - Scanning Electron Microscopy
    - Atomic Force Microscopy

3.2 Materials

The following materials were supplied by the Department of National Defense (DND) for investigation:

- Maraging Steel 300 (Mars 300)
- High Hardness Armor (HHA) Steel
- Aluminum 5083-H131 Alloy (Al 5083)

The required specimens were machined from these materials.

3.3 Geometry of the specimens

- Specimens for direct impact (compression) experiments

  Cylindrical specimens machined for Split Hopkinson Pressure Bar impact testing were 10.5 mm in length and 9.5 mm in diameter. Maximum strain and strain rate are achieved with these dimensions during impact loading, based on earlier work by Bassim (2001).

Figure 3.1: Cylindrical specimens

- Specimens for torsion experiments

  Hexagonal shaped specimens were machined for Torsional Split Hopkinson Bar (TSHB) experiments. The specimens had an internal diameter of 12.8 mm and an external diameter of 13.8 mm. Both Maraging Steel 300 and Aluminum 5083 – H131 Alloy specimens were subjected to TSHB experiments.

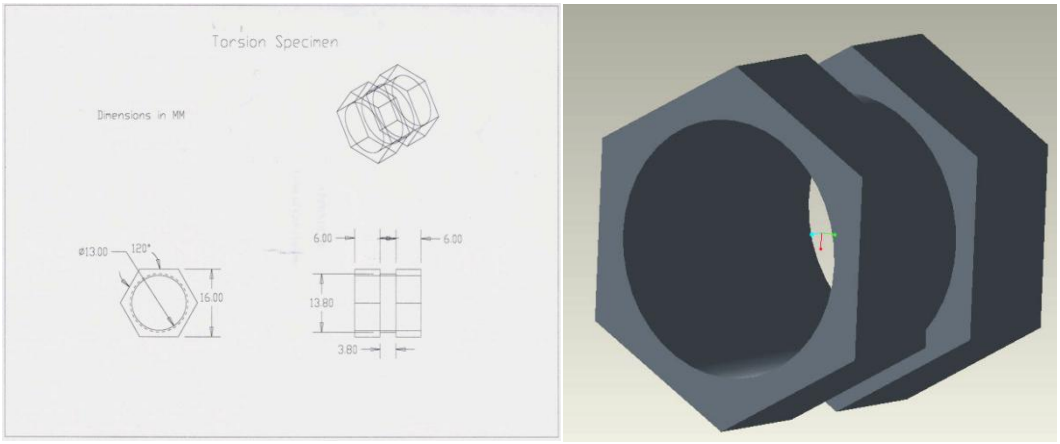

Figure 3.2: Hexagonal Shaped Steel Rings

3.4 Impact experiments

The three different materials were subjected to direct impact loading using the Split Hopkinson Pressure Bar (SHPB). The range of firing pressure for Mars 300 was 100 – 200 kPa, for HHA was 100 – 200 kPa and for Aluminum 5083 – H131 Alloy was 60 – 150 kPa. The high strain rate investigation of dynamic mechanical loading has a direct relation between the firing pressure and the response through the impact momentum of the projectile. The relationship between firing pressure and impact momentum of the projectile were based on previous experiments conducted at the University of Manitoba. All SHPB experiments were conducted at atmospheric pressure and room temperature.

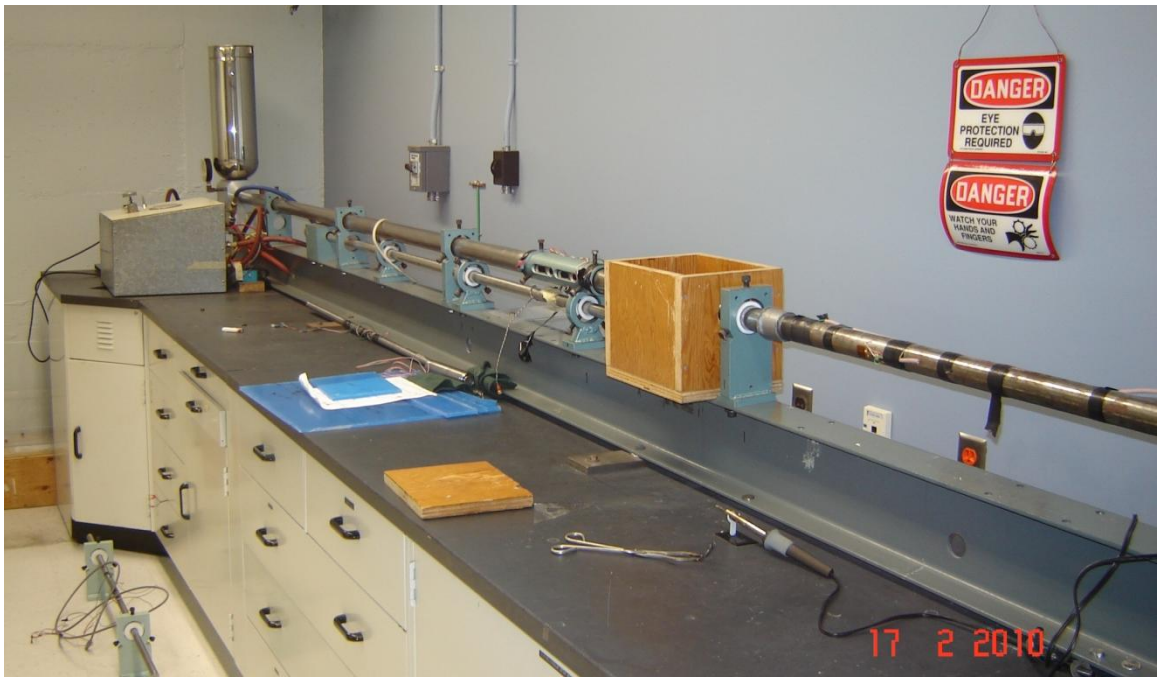

Figure 3.3: Split Hopkinson Pressure Bar

3.4.1 Operation of the Split Hopkinson Pressure Bar (Direct Impact)

The original SHPB was developed from the Bertram Hopkinson Bar by Kolsky in 1949 and remains the common equipment for measuring the response of engineering materials to high strain rate deformation. The SHPB is commonly used in the investigation of materials under high strain rate deformation, in the range of strain rates between 10^3 to 10^4 s^{-1}. A schematic diagram of the SHPB is presented in Figure 3.5. The equipment consists of the following parts:

a. Accumulator and Firing Chamber

   Compressed air in the accumulator produces the pressure in the fire barrel to force the projectile. The projectile then strikes the sample at very high impact momentum. A pressure gage attached to the accumulator measures the firing pressure.

b. Control Box

   The control unit consist of a Power Switch button, Retract/ Reset button that serve to bring the projectile to its start point, a Charge button for initiating the charging process before firing, an Accumulator Pressure button for controlling the firing pressure, a Fire button for firing the projectile and a Pressure Gage to select the desired pressure before firing.

c. Gun Barrel

   A hollow cylinder connected to the gun barrel to direct the projectile towards the specimen at very high velocity.

d. Timer

The timer consists of two sets of gages connected to the gun barrel at 250 mm apart from each other. It measures the time taken for the projectile to travel between these two locations. The velocity of the projectile is then calculated based on the time taken and the distance travelled (250 mm).

e. Projectile

The projectile is machined out of cylindrical AISI 4340 steel bar with a 230 mm in length. The cylindrical projectile is heat treated to a Rockwell Hardness of 47 HRC and weighs 1.905 kg. The projectile upon impact causes compressive stress waves to travel through the specimen to the transmitter bar.

f. Transmitter Bar

The transmitter bar is machined out of AISI 4340 steel and heat treated to a hardness of 45 HRC. The transmitter bar is connected to a strain gage and pulse amplifier that captures the transmitting waves from impact. The signal is amplified and sent to the oscilloscope where the strain wave data are stored in the form of voltage versus time data. The data are then processed to obtain the stress-strain curves/ data for impact loading experiments. Wooden blocks at the end of the transmitter bar act as suspension during impact and reduce vibrations.

Figure 3.4: Image showing the control box, accumulator and firing chamber

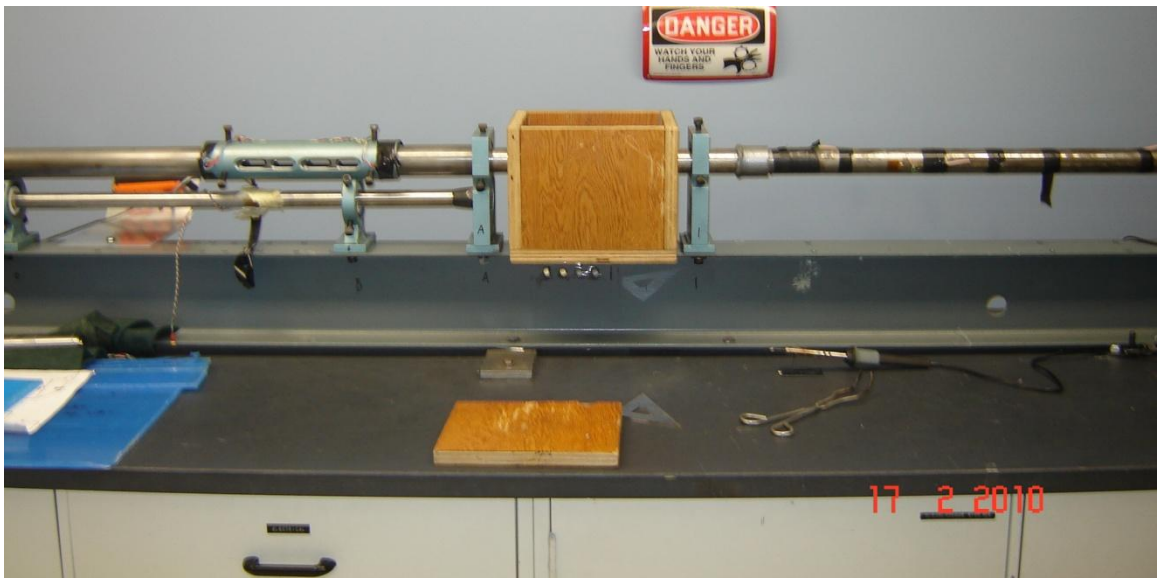

Figure 3.5: Strain gage and transmitted bar

Figure 3.6: Sample placement on transmitted bar

Figure 3.7: Projectile

3.4.2 Calculation of Stress, Strain and Strain Rates for Impact Loading Experiments

The oscilloscope captures the signal in the form of voltage versus time data from the strain gages at the transmitter bar. The relationship between the load and signal voltage is given by the following equation from equipment calibration

Load (kN) = Voltage (mV) * 0.13735 Eq (3.1)

The true stress and true strain with respect to time are given by the following equations:

$$\varepsilon(t_s) = \ln \frac{L_i}{L_i - (L_i - L_f)\left(\frac{t_s}{t_f}\right)} \quad \text{Eq (3.2)}$$

where L_i and L_f are initial and final lengths, respectively of the specimen.

$$\sigma(t_s) = \frac{P_i\,[L_i - (L_i - L_f)\left(\frac{t_s}{t_f}\right)]}{A_i\,[L_i]} \quad \text{Eq (3.3)}$$

Assuming constant volume, linear variation of displacement with time and constant strain rate, the maximum strain in a specimen is directly proportional to the strain rate and length of the striker bar.

The strain rate is calculated for each specimen using equation 3.4

$$\varepsilon = 2\dot{\varepsilon}\frac{l}{C_o} \qquad \dot{\varepsilon} = \varepsilon\frac{C_o}{2l} \quad \text{Eq (3.4)}$$

Where C_o is the longitudinal wave propagation velocity in the transmitter bar. Dynamic stress strain curves at high strain rates are generated using equations 3.2 – 3.4 and results are presented in Table 4.1.

Firing Pressure (KPa)	Time (sec)	Impact Momentum (Kg.m/s)
100	16.23	32.91
100	16.18	28.79
150	13.30	40.16
150	13.33	40.07
200	12.03	44.39
200	11.99	44.54
100	16.23	32.91
100	16.18	28.79
150	13.32	40.10
150	13.27	40.24
200	11.74	45.49
200	11.74	45.49
100	16.23	32.91
100	16.18	28.79
150	13.34	40.04
150	13.34	40.04
200	11.58	45.07
200	11.99	44.54
200	12.03	44.39
100	16.23	32.91
100	16.18	28.79
150	13.32	40.10
150	13.27	40.24
200	11.74	45.49
200	11.74	45.49
80	18.55	28.63
80	18.65	29.09
100	16.23	32.91
100	16.18	28.79
150	13.34	40.04
150	13.29	40.19

Table 3.1: Relation between firing pressure and impact momentum (Mirfakhraei 2008)

3.5 Torsion experiments

The Torsional Split Hopkinson Bar (TSHB) is a modified version of the Split Hopkinson Pressure Bar used to deform the specimen at a shear strain rate in excess of $10^3 s^{-1}$, depending on the amount of applied torque. The TSHB was first used by Baker and Yew in 1966 (Mechanical Testing and Evaluation 2000, Bai and Dodd 1992). The TSHB is used to investigate the thin-walled sections of materials subjected to high strain rate torsion loading. While in the Split Hopkinson Pressure Bar, the specimen is impacted at high velocity that allows for radial expansion in the specimen, in TSHB experiments, the specimen undergoes a homogeneous shear deformation at the thin-walled sections. Also, due to the absence of Poisson's ratio effect, inertial and frictional effects in torsion experiments are not present. On the other hand, there is a limit to the applied torque that could be stored in the incident bar. Hence, the strain rates achieved in torsion loading are lower compared to impact loading.

Figure 3.8: Torsional Split Hopkinson Bar

3.5.1 Operation of the Torsional Split Hopkinson Pressure Bar

As seen in Figure 3.8, the TSHB equipment consists of two bars: the incident and the transmitted bar. Both bars are made from Aluminum 6061-T6 alloy and are of 25.4mm in diameter. Each bar is 1.829 m long and suspended on Teflon bushings at equal distance and in turn attached to a 4 m long I-beam. There is one strain gage attached at equidistance from the sample to each incident and transmitted bar. This ensures incident and transmitted waves do not overlap.

The following steps explain the procedure for torsion experiments:

- The loading pin at the bottom of the clamp is loosened
- A notched bolt made from Aluminum 6061-T6 is placed at the top hole in the clamp and securely tightened by bolts
- Using a wrench, the pin in front of the clamp is tightened to prevent the incident bar from rotating
- Torsion load is applied by a hydraulic jack connected to a rotating wheel that is attached to the loading end of the incident bar. This stores the applied torque in the clamped section of the bar.
- The specimen is then placed in the hexagonal socket and transmitted bar turned clockwise until there is no further movement
- The trigger is set on the data acquisition system to the desired trigger voltage
- The loading pin at the bottom of the clamp is further tightened using a wrench
- The notched bolt fractures and the bar rotates to release the stored torque rapidly to produce high strain rates

- The elastic wave generated continues as incident wave at the incident bar till it reaches the specimen. This wave is captured by the strain gage on the incident bar as Incident wave.
- On reaching the specimen, the incident wave decomposes into Transmitted wave and Reflected wave.
- Partial energy from the incident wave is used in deforming the specimen and the strain gage at the transmitted bar captures the signal as Transmitted wave.
- The wave reflected back to the incident bar is captured by the strain gage as Reflected wave.

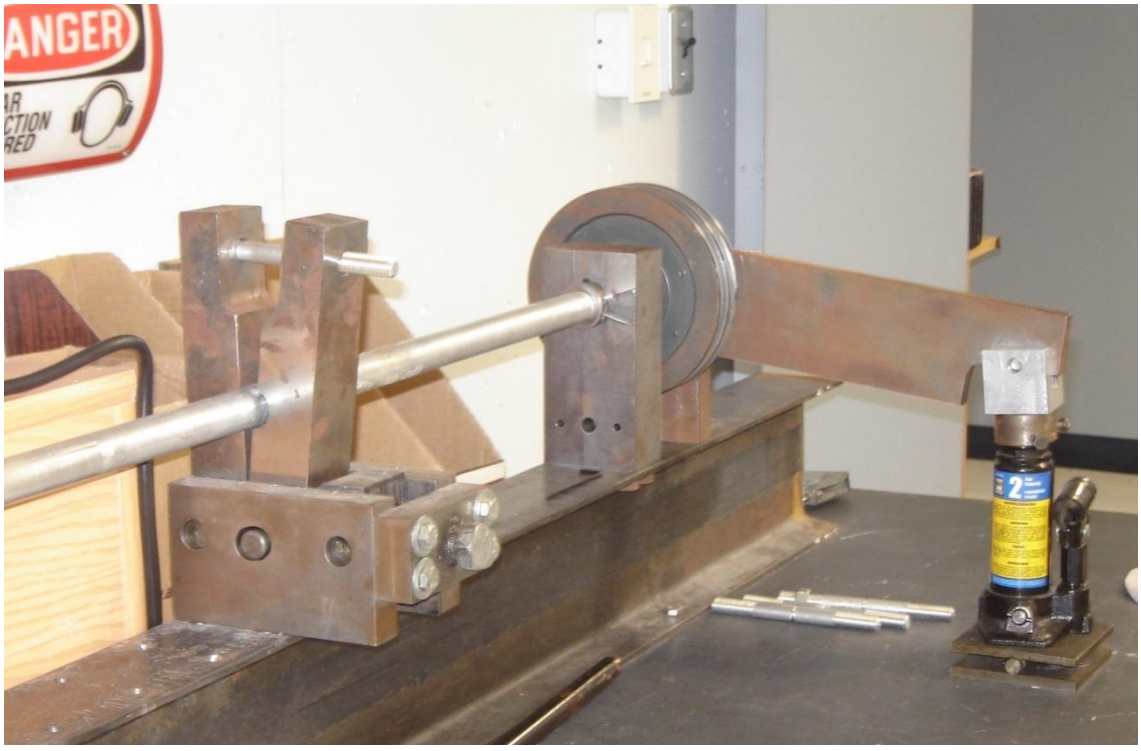

Figure 3.9: Clamping device and loading mechanism consisting of hydraulic jack and rotating wheel

This image has been removed due to copyright issues. Refer to its source.

Figure 3.10: The clamping mechanism (Cepus 1995)

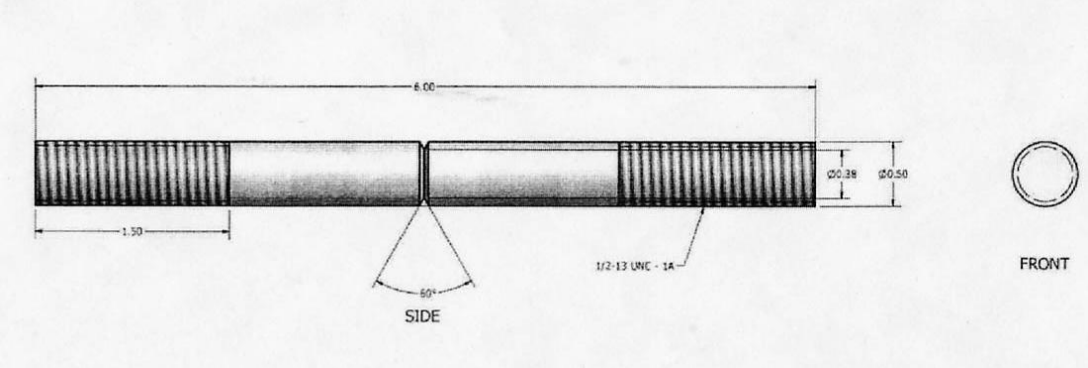

Figure 3.11: Schematic for Aluminum notch

Figure 3.12: The TSHB showing incident bar, transmitted bar and data acquisition device

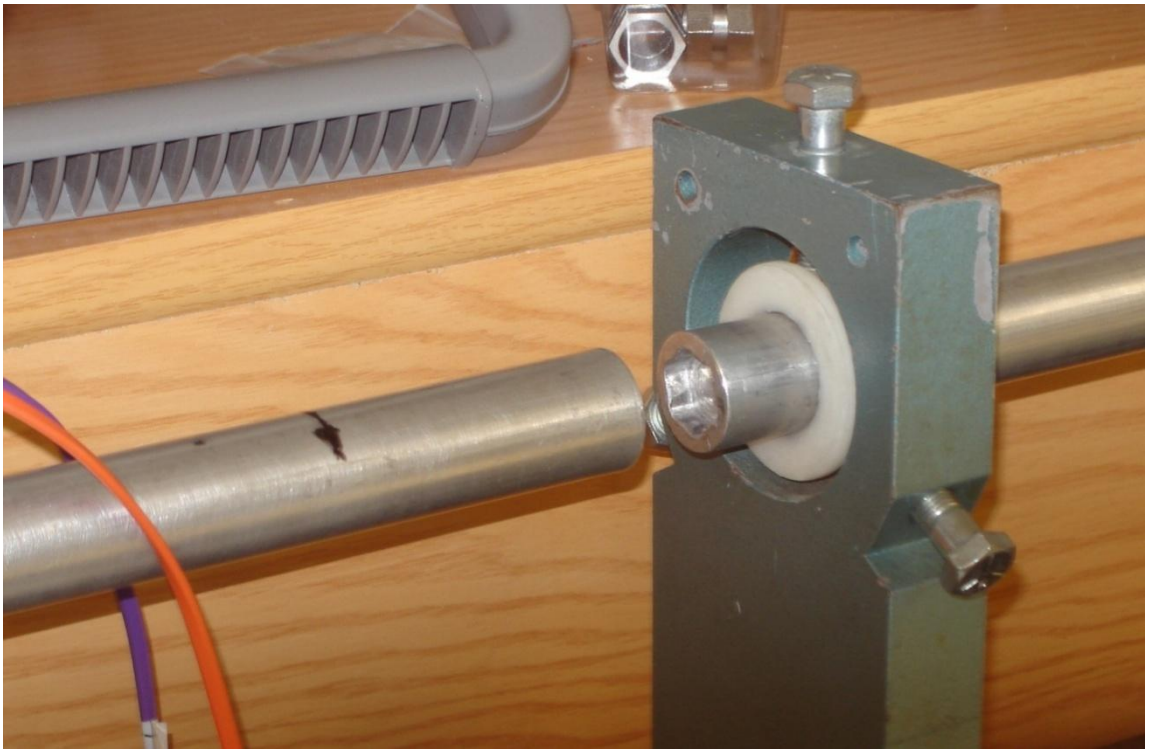

Figure 3.13: Hexagonal socket holder at the centre between incident and transmitted bar

3.5.2 Calculation of Stress, Strain and Strain Rates for Torsion Loading

The calibration of the TSHB gives the mathematical relation between the shear strain and the voltage recorded by the strain gages. The equipment calibration involves placing of a solid hexagonal rod in between the incident and the transmitter bar. The end of the transmitter bar is fixed and the torque is applied at increasing angles of twist. The two strain gages record the corresponding voltage measurements. The mathematical relationship between the voltage measured by the strain gages and the corresponding value of shear strains on the bars is given by the linear plot of shear strain against the strength of signal voltage.

The corresponding maximum shear strain on the surface of the bar as the torque is applied is given by:

$$\gamma = \frac{c\phi}{L} \qquad \text{Eq (3.5)}$$

The shear strain in the specimen is given by equation (3.6)

$$\gamma_s = \frac{D_s\phi_2 - D_s\phi_1}{2L_s} \qquad \text{Eq (3.6)}$$

Where ϕ_1 and ϕ_2 are the angles of twist in the incident and transmitter bars respectively. The mean diameter of the thin walled specimen is given by D_s and its length by L_s. The value of ϕ_2 can be determined at the surface of the transmitter bar using the following equation.

$$\gamma_s = \frac{D}{2}\frac{\partial\phi_2}{\partial x} = \frac{D}{2C}\frac{\partial\phi_2}{\partial t} \qquad \text{Eq (3.7)}$$

D is the diameter of the incident and transmitter bar

$$C = \sqrt{\frac{G}{\rho}} \qquad \text{Eq (3.8)}$$

C is given by the velocity of wave propagation in the bar

$$\phi_2 = \frac{2C}{D}\int_0^t \gamma_T(t)dt \qquad \text{Eq (3.9)}$$

Calculating the difference in strains due to the incident and reflected pulse gives the angle of twist in the incident bar ϕ_2.

$$\phi_1 = \frac{2C}{D}\int_0^t [\gamma_T(t) - \gamma_R(t)]dt \qquad \text{Eq (3.10)}$$

Differentiating equation (3.6) and substituting equations (3.9) and (3.10) gives the following equation. The negative sign is due to the travel of reflected pulse in the opposite direction of the incident pulse.

$$\dot{\gamma}_s(t) = \frac{CD_s}{L_s D}[\gamma_T(t) - \{\gamma_I(t) - \gamma_R(t)\}] \qquad \text{Eq (3.11)}$$

We also know that the total torque (T) stored in the bar before loading of the test specimen is

$$T = \frac{\phi JG}{L} \qquad \text{Eq (3.12)}$$

The transmitted pulse is the difference between the incident and the reflected pulses for a state of homogeneous strain. Equation (3.12) reduces to:

$$\dot{\gamma}_s(t) = \frac{2CD_s}{L_s D}\gamma_R(t) \qquad \text{Eq (3.13)}$$

Integrating equation (3.11) gives the value of strain $\gamma_s(t)$ at time, t

$$\gamma_s(t) = \int_0^t \frac{C}{L_s}\frac{D_s}{D}[\gamma_T(t) - \{\gamma_I(t) - \gamma_R(t)\}]dt \quad \text{Eq (3.14)}$$

Simplifying equation (3.14) shows

$$\gamma_s(t) = \frac{CD_s}{L_s D}\sum[\gamma_T(t) - \{\gamma_I(t) - \gamma_R(t)\}]\Delta t \quad \text{Eq (3.15)}$$

The stress in thin-walled tube is given by the following equation based on Kolsky's work

$$\tau_s = \frac{2Ts}{(\pi D_s^2)t_s} \quad \text{Eq (3.16)}$$

Where t_s and T_s are wall thickness and average torque respectively. The average torque is calculated by:

$$T_s = \frac{1}{2}(T_1 + T_2) \quad \text{Eq (3.17)}$$

T_1 is given by the torque at the surface of the incident bar in terms of strain

$$T_1 = \frac{\pi G D^3(\gamma_I - \gamma_R)}{16} \quad \text{Eq (3.18)}$$

T_2 is given by the torque at the surface of the transmitter bar in terms of strain

$$T_2 = \frac{\pi G D^3 \gamma_T}{16} \quad \text{Eq (3.19)}$$

The stress in the thin-walled sample is given by equation (3.20) after substituting equation (3.17), (3.18) and (3.19).

$$\tau_{s(t)} = \frac{GD^3(\gamma_{I(t)} - \gamma_{R(t)} + \gamma_{T(t)})}{16 D_s^2 t_s} \quad \text{Eq (3.20)}$$

The transmitter pulse can be expressed as the difference between the incident and reflected pulses for a homogeneous state of strain. Equation (3.20) can be simplified to:

$$\tau_{s(t)} = \frac{GD^3}{8 D_s^2 t_s}\gamma_T \quad \text{Eq (3.21)}$$

Therefore, using equations (3.11), (3.15) and (3.20) can be used to determine strain rate, strain and stress respectively in a sample as a function of time.

3.6 Specimen preparation for microstructural analysis

Specimens subjected to impact loading experiments were mounted using black phenolic powder (Bakelite), grinded and polished to obtain a mirror surface finish. The specimens are then etched for microstructural investigation. Specimen preparation for hexagonal shaped samples included cutting in longitudinal sections using wire EDM technique for a smooth surface. This was followed by mounting, grinding, polishing and etching.

- Mounting

  Specimens were mounted using the LECO PR – 25 equipment. The specimen is placed in the chamber and black phenolic powder is added. Mounting requires high temperature and pressure to bind the powder to form a solid circular mass with a specimen in the centre. Temperatures and pressures of approximately 150°C and 3500 psi respectively are required to mount the specimens.

- Grinding and Polishing

  The specimens are grinded on emery paper from coarse 120 microns to fine 1200 microns. The grinding process removes scratches and produces a fine and smooth surface. Steel specimens are then polished using the 6 micron and 1 micron diamond polishing solution on the 6 micron and 1 micron polishing wheel respectively. Aluminum specimens were polished using soap and colloidal silica

solution of 50 nm – 164 nm on the 6 micron and 1 micron polishing wheel. The specimens are then rinsed with distilled water and immersed in ethyl alcohol in an ultrasonic rinsing bath to remove fine particles on the surface. All specimens had a mirror surface finish prior to etching.

- Etching

  A 2% Nital etching agent was used for both Mars 300 and HHA specimens for approximately 35 – 45 seconds. Aluminum specimens were etched using Aluminum Etch (1960, CPG Grade) for approximately 17 – 19 minutes. The Aluminum Etch is composed of 60% - 80% Phosphoric Acid, 10% - 25% Acetic Acid and 0.1% - 5% Nitric Acid. This was followed by rinsing in distilled water and dried.

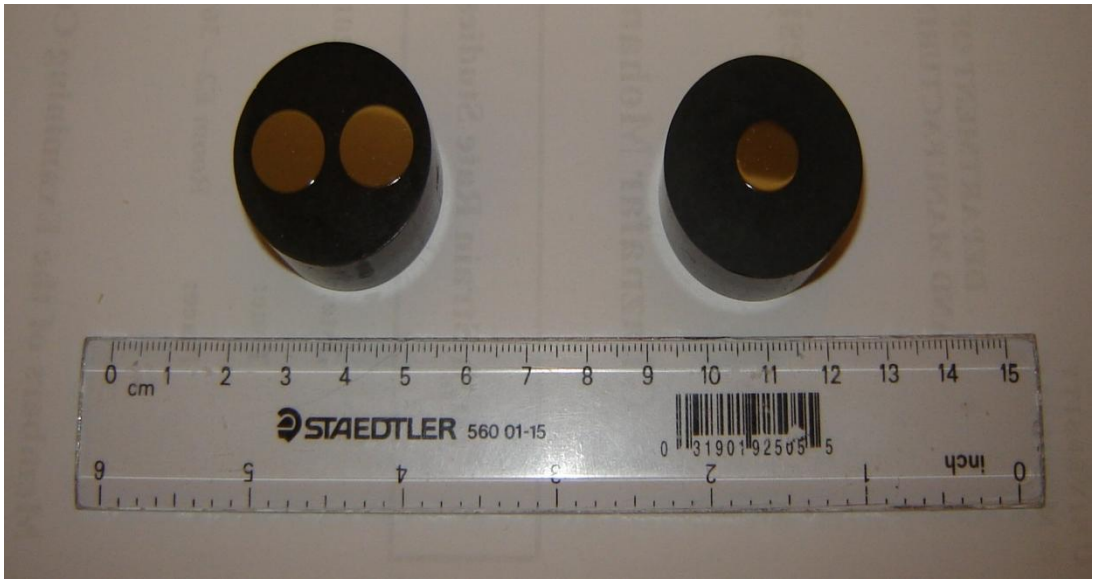

Figure 3.14: Specimen mounted from impact loading experiments

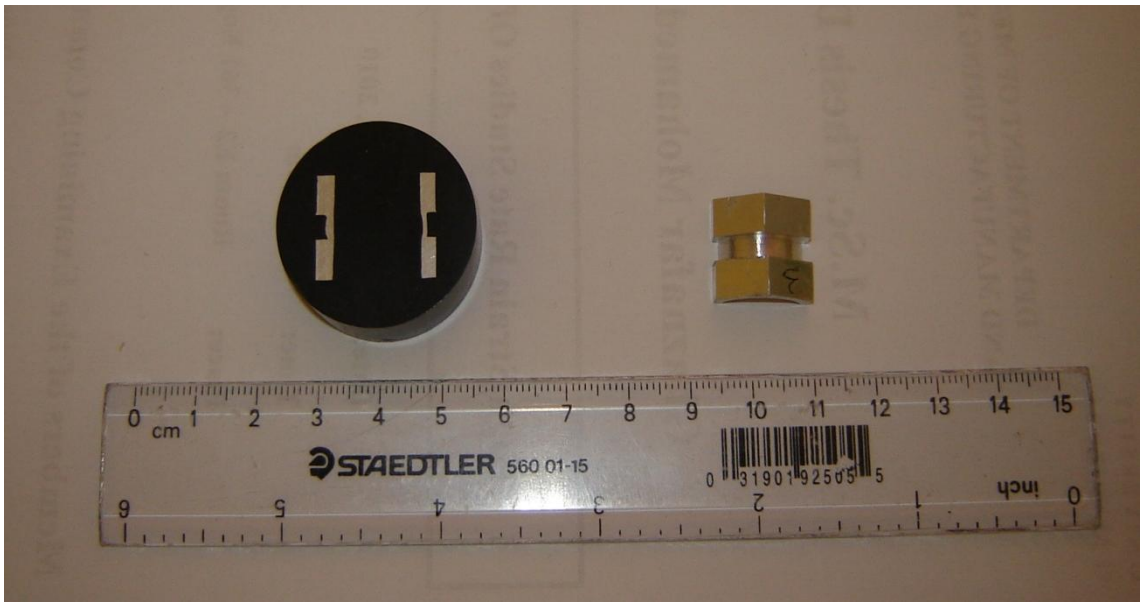

Figure 3.15: Specimen mounted from torsion loading experiments

3.7 Microstructural Investigation using Optical Microscopy

All specimens prepared for microstructural examination were studied using the Zeiss optical microscope with Clemex Vision Analyzer. Specimens from impact and torsion loading experiments were thoroughly examined for defects in microstructure such as micro-cracks, shear bands and cracks. A detailed specimen examination consisted of imaging a section of the microstructure at a magnification of 50x to 200x or 500x depending on the resolution and clarity of the image. Most valuable information such as deformation to reorientation of grains and presence of shear bands were evaluated using the optical microscopy technique. The images from optical microscopy are presented in Chapter 4 and discussed in Chapter 5.

3.8 Microstructural Investigation using Scanning Electron Microscopy (SEM)

A fractured specimen from impact loading experiments was studied using the SEM technique. The two halves of a fractured specimen (HHA) were investigated using an applied voltage of 20V on JELO JSM-5900 LV SEM. The images from SEM are presented in Chapter 4.

3.9 Microstructural Investigation using Atomic Force Microscopy

The Atomic Force Microscopy (AFM) is an advanced technique to produce high resolution and three-dimensional images from examining the surface of a material. It is performed by the Dimension 3100 Scanning Probe Microscope by scanning a sharp tip over the specimen surface (Dimension 3100 Manual 2003). The process involves the tip (flexible cantilever) mounted on one end of a cylindrical piezo-electric tube which in turn is mounted near the top of the microscope (Dimension 3100 Manual 2003). The piezo-electric tube contains X, Y and Z electrodes to detect the applied voltages. The X and Y electrodes on detecting the voltage, deflects the tube horizontally while the Z electrode upon the applied voltage detects the vertical height of the tip. There is a stepper motor attached to a lead screw that moves the specimen and a separate motor drive to control the height of the microscope and tip with respect to the material surface.

A TappingMode AFM with etched silicon cantilever substrates was utilized to perform the scans. When the cantilever comes near the material surface, the piezo stack continues to excite the cantilever substrate with the same energy and causes the tip to deflect on contact with the surface (Dimension 3100 Manual 2003). The reflected laser beam provides information such as height and characteristic of the material in a specified region. Scans are performed by selecting a region (inside or outside the shear band) 100μm x 100μm and optimizing the set point amplitude that increases the force at which the scan tip performs the TappingMode. The scan rate is also optimized so that it does not skip a region due to uneven surface texture. AFM scans were performed with both etched and unetched specimen (Mars 300) to study the characteristic of the microstructure. Due

to the size of the tip, it was not possible to perform AFM scans on a deformed banded region (HHA and Al 5083 samples).

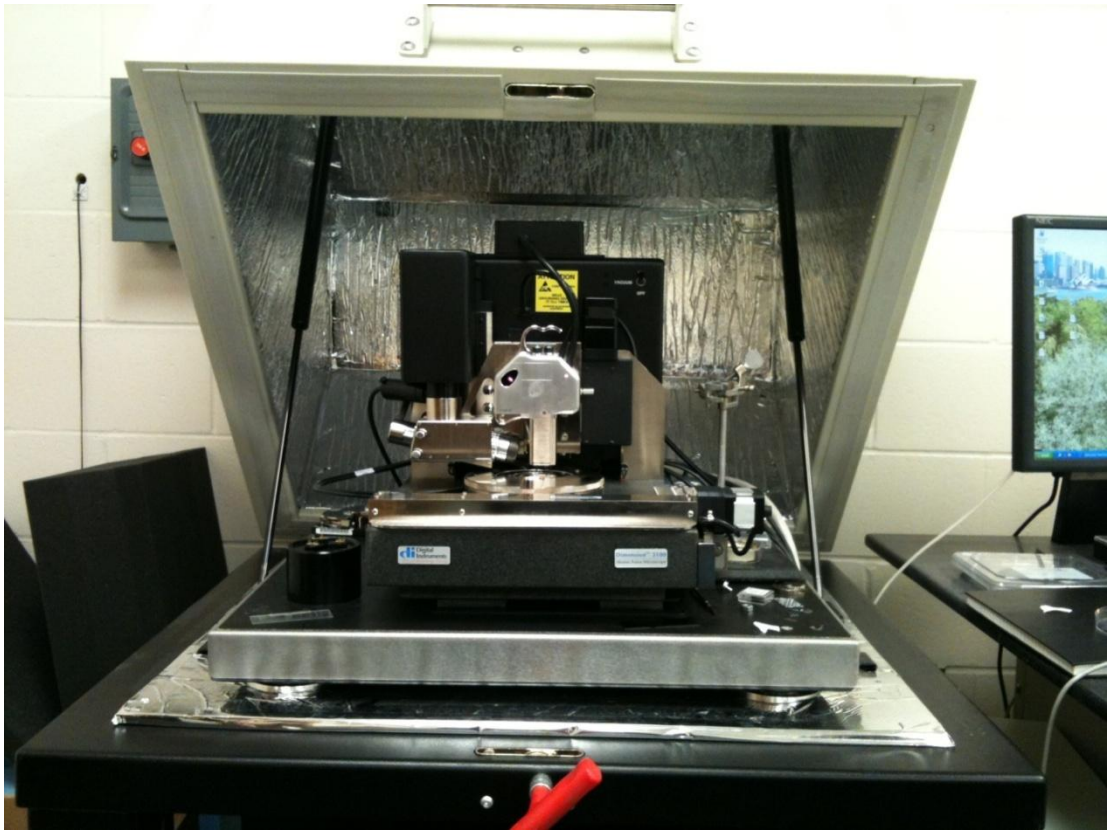

Figure 3.16: The Dimension 3100 SPM – Atomic Force Microscopy equipment

This image has been removed due to copyright issues. Refer to its source.

Figure 3.17: Dimension 3100 SPM Head (Dimension 3100 Manual 2003)

This image has been removed due to copyright issues. Refer to its source.

Figure 3.18: Shape of cantilever tip used for TappingMode scans (Dimension 3100 Manual 2003)

CHAPTER FOUR: EXPERIMENTAL RESULTS

4.1 Introduction

This chapter will focus on

1. The results of the dynamic mechanical tests at high strain-rates on the following armor materials:
    - Maraging steel (Mars 300)
    - High Hardness Armor (HHA)
    - Aluminum 5083-H131 Alloy
2. The deformation behavior of the specimens under different impact and torsion loading
3. Investigation of strain localization and occurrence of Adiabatic Shear Bands (ASB) under impact and torsion loading
4. Investigation of microstructural evolution during deformation using
    - Optical Microscopy
    - Atomic Force Microscopy (AFM)
    - Scanning Electron Microscopy (SEM)
5. Comparison of results from the mechanical tests and microstructural analysis

4.2 Dynamic Stress-Strain Curves for Impact Loading Experiments

The experimental data for impact loading using the Split Hopkinson Pressure Bar – Direct Impact (SHPB) are presented in Table 4.1 for the three materials. The relationship between the firing pressure and impact momentum had been computed in a previous investigation (see Table 3.1) (Mirfakhraei 2008) and was utilized in this thesis. The behavior of the materials subjected to impact loading is studied with respect to impact momentum. Typical stress-strain curves for each material at different impact momentums are presented in Figures 4.1 to 4.3.

The stress-strain curves for Maraging steel 300 (Mars 300) subjected to impact loading are shown in Figure 4.1. It could seen clearly that as the impact momentum is increased from 32.91 kg.m/s to 40.04 kg.m/s, the maximum flow stress increases from 1200 MPa to 1600 MPa. Analysing the data presented from Table 4.1 shows as the impact momentum is increased from 32.91 kg.m/s to 44.54 kg.m/s, the values for strain rate increases from 546.13 /s to 1158.61 /s. Referring to Figures 4.4 and 4.5, it is observed that an increase in impact momentum increases the maximum flow stress and strain rate for Mars 300.

Similarly, Figures 4.2 and 4.3 shows the stress-strain curve for High Hardness Armor (HHA) and Aluminum 5083-H131 Alloy specimens respectively. Referring to Table 4.1 and Figure 4.4, it is observed that the strain rate for HHA also increases with increasing impact momentum. When compared with Mars 300, the maximum flow stress for HHA is higher and in the range of 1800 MPa. From Figure 4.5, it could be seen that the maximum flow stress for HHA remains constant when the impact momentum is

increased from 30 kg.m /s to 40 kg.m/s but has a slight drop at 45 kg.m/s. The drop in flow stress at high impact momentum could be attributed to the material losing its strength due to thermal softening.

Observing Figures 4.3 to 4.5 and Table 4.1 for Aluminum 5083 – H131 Alloy, it is also evident that as the impact momentum is increased, the maximum flow stresses and strain rate increases. Aluminum, which is a rather ductile material, has a large plastic deformation region in the stress-strain curve (Figure 4.3) before the flow stress reaches the maximum stress. When the impact momentum is increased, the work in plastic strain region is larger as it can be seen by a gradual transition of the flow stress to reach the ultimate or maximum stresses. The effect of impact momentum on maximum flow stress has no effect on Aluminum 5083 – H131 Alloy as seen in Figure 4.5.

Figure 4.6 shows the stress-strain curve for Mars 300, HHA and Aluminum 5083 – H131 Alloy at a comparable impact momentum of 40 kg.m/s. It is clearly evident that Aluminum 5083 – H131 Alloy having a much larger plastic strain region than Mars 300 and HHA. Stress collapse in the latter materials occurs while Aluminum 5083 – H131 Alloy is still undergoing strain hardening. On the other hand, maximum flow stresses are significantly high in Mars 300 and HHA than for Aluminum 5083 – H131 Alloy. Detailed description on the behavior of the three materials based on the stress-strain curves are discussed in Chapter 5.

Sample No	Material	L_o (mm)	L_f (mm)	D_o (mm)	Area (mm^2)	Pressure (KPa)	Time (sec)	Impact Momentum (Kg.m/s)	Strain Rate (/s)
1	Mars 300	10.54	8.58	9.49	70.78	100	16.23	32.91	400.9
2	Mars 300	10.55	8.67	9.51	71.08	100	16.18	28.79	503.51
3	Mars 300	10.55	7.93	9.43	69.84	150	13.30	40.16	664.34
4	Mars 300	10.40	7.83	9.51	71.08	150	13.33	40.07	547.87
5	Mars 300	10.50	7.22	9.55	71.58	200	12.03	44.39	713.63
6	Mars 300	10.55	7.17	9.52	71.18	200	11.99	44.54	720.15
1	HHA	10.63	9.33	9.40	69.40	100	16.23	32.91	558.65
2	HHA	10.54	9.33	9.45	70.14	100	16.18	28.79	349.05
3	HHA	10.53	8.79	9.48	70.63	150	13.32	40.10	523.77
4	HHA	10.52	8.81	9.43	69.80	150	13.27	40.24	927.32
5	HHA	10.57	6.52	9.51	71.00	200	11.74	45.49	2437.03
6	HHA	10.61	6.51	9.48	70.58	200	11.74	45.49	1725.99
1	Mars 300	10.53	8.48	9.51	70.98	100	16.23	32.91	546.13
2	Mars 300	10.44	8.42	9.45	70.09	100	16.18	28.79	547.8
3	Mars 300	10.45	7.74	9.48	70.53	150	13.34	40.04	747.6
4	Mars 300	10.54	7.78	9.48	70.58	150	13.34	40.04	747.41
5	Mars 300	10.48	6.95	9.48	70.63	200	11.58	45.07	928.03
6	Mars 300	10.53	6.00	9.48	70.63	200	11.99	44.54	1158.61
7	Mars 300	10.49	6.87	9.44	70.04	200	12.03	44.39	785.13
1	HHA	10.50	9.16	9.43	69.89	100	16.23	32.91	475.78
2	HHA	10.52	9.21	9.51	70.98	100	16.18	28.79	465.96
3	HHA	10.51	8.65	9.48	70.53	150	13.32	40.10	570.82
4	HHA	10.48	8.66	9.50	70.88	150	13.27	40.24	584.81
5	HHA	10.51	5.98	9.50	70.83	200	11.74	45.49	3156.95

6	HHA	10.58	5.80	9.44	69.99	200	11.74	45.49	3884.9
1	Aluminum	10.39	4.59	9.50	70.83	80	18.55	28.63	953.91
2	Aluminum	10.46	4.47	9.52	71.13	80	18.65	29.09	1001.83
3	Aluminum	10.45	4.05	9.50	70.83	100	16.23	32.91	1114.98
4	Aluminum	10.49	5.92	9.50	70.88	100	16.18	28.79	748.87
5	Aluminum	10.47	2.98	9.52	71.13	150	13.34	40.04	1445.25
6	Aluminum	10.50	2.91	9.52	71.13	150	13.29	40.19	1471.27
7	Aluminum	10.43	6.04	9.50	70.88	60	19.85	20.34	843.31
8	Aluminum	10.49	6.05	9.51	71.03	60	19.85	20.34	688.97

Table 4.1: Summary of results for impact loading experiments

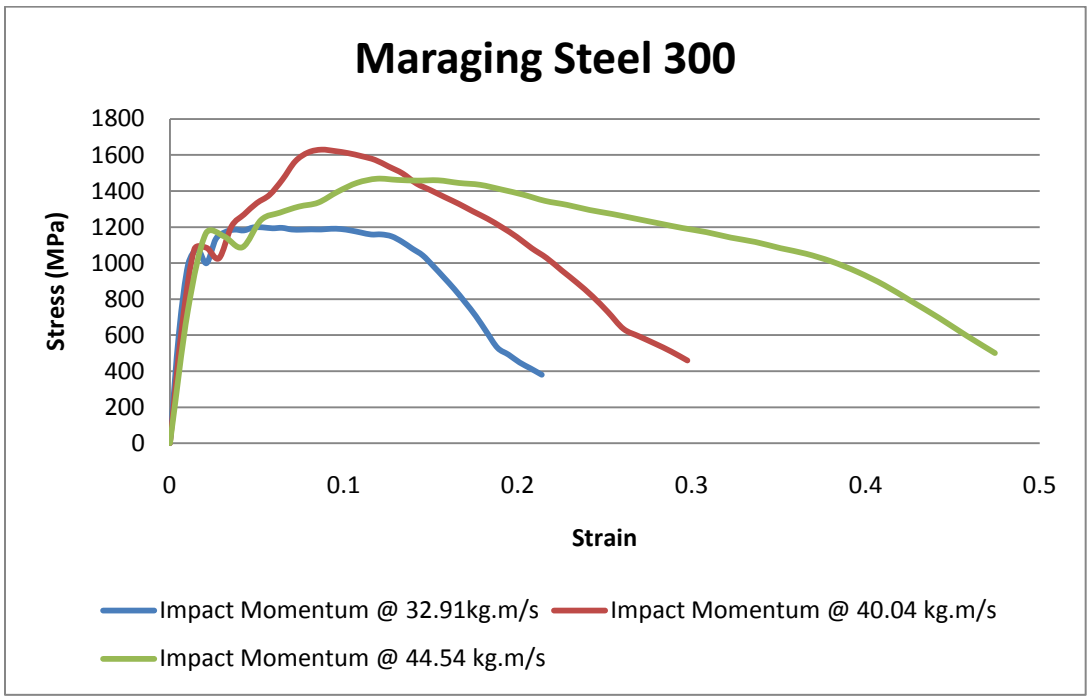

Figure 4.1: Dynamic stress-strain curve for Mars 300 specimens at different impact momentum

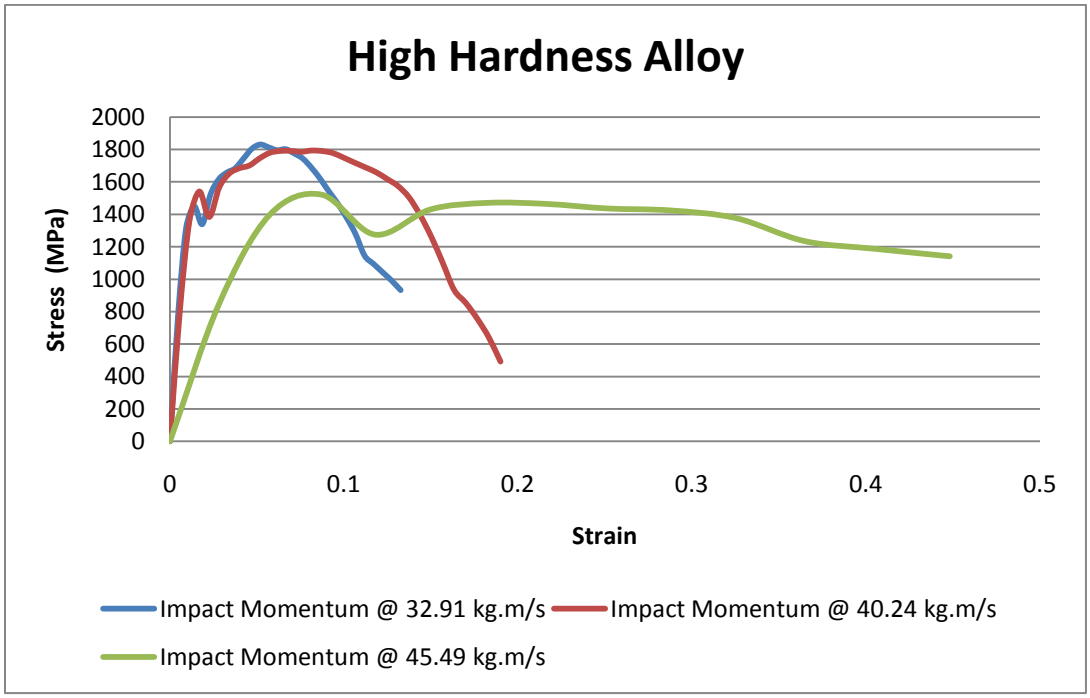

Figure 4.2: Dynamic stress-strain curve for HHA specimens at different impact momentum

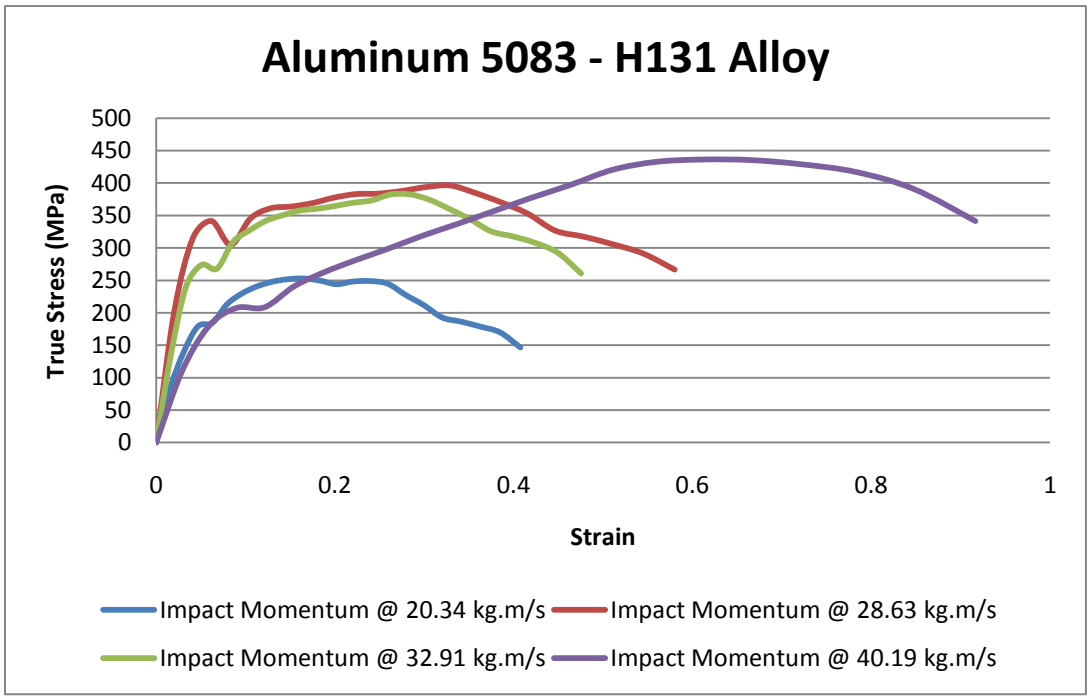

Figure 4.3: Dynamic stress-strain curve for aluminum specimens at different impact momentum

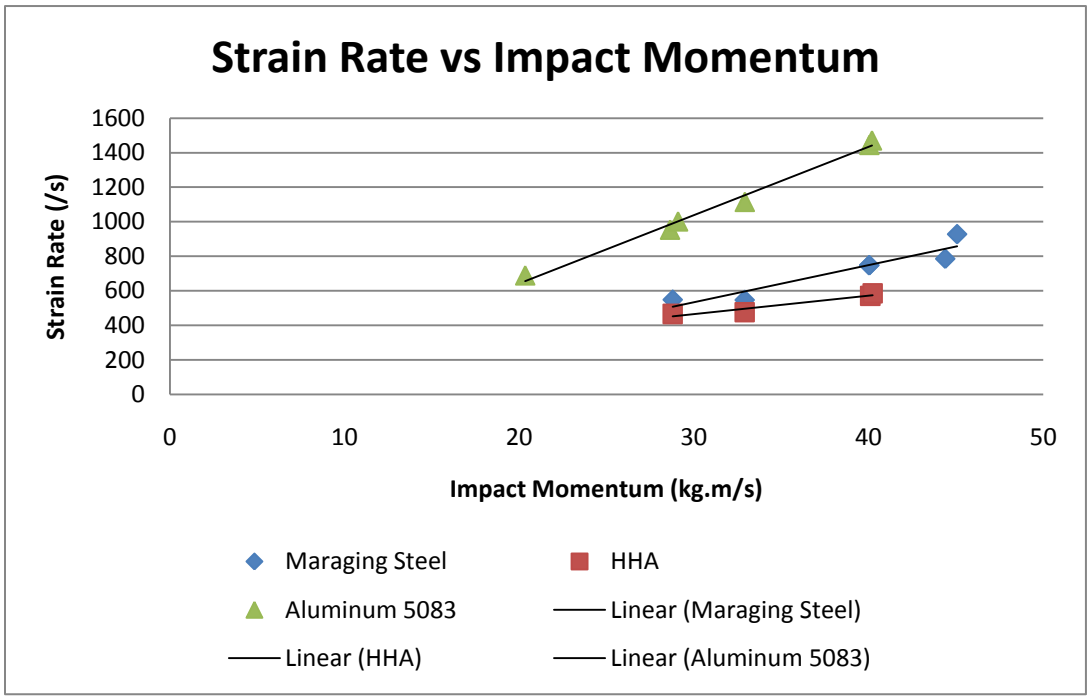

Figure 4.4: The effect of impact momentum on strain rates for all three materials

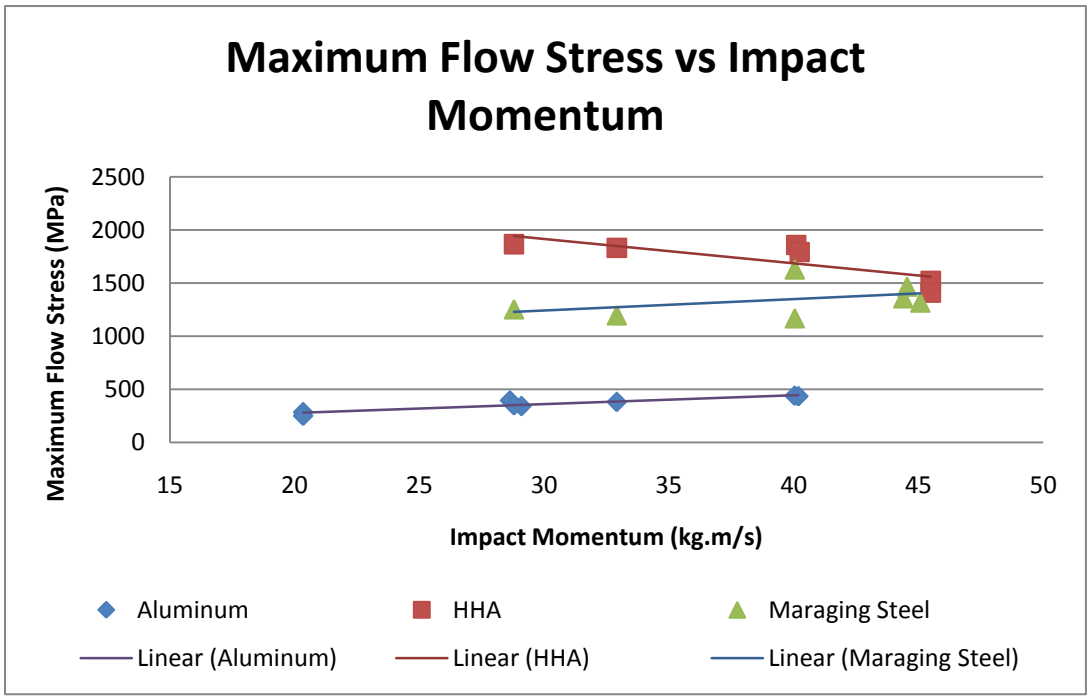

Figure 4.5: The effect of impact momentum on maximum flow stress for all three materials

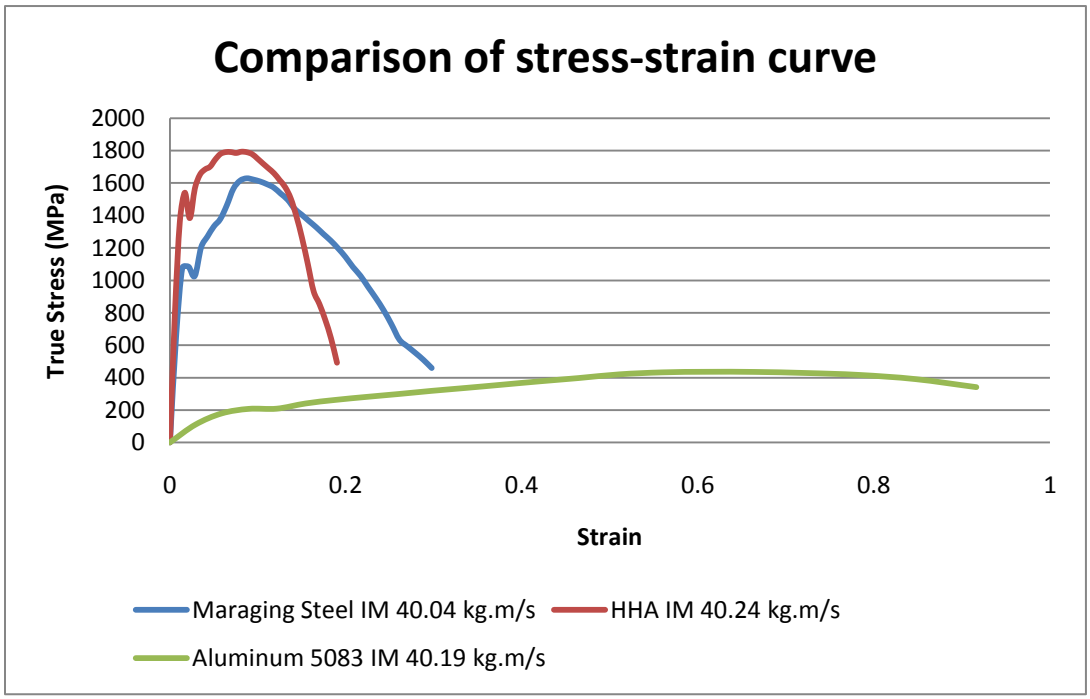

Figure 4.6: Comparison of stress-strain curve at 40 kg.m/s (Impact Momentum)

4.3 Dynamic Stress-Strain Curves for Torsion Loading Experiments

The two strain gauges attached on to the Torsional Split Hopkinson Bar capture the signals during the torsion experiments. The captured data on the oscilloscope is presented in the form of voltage versus time and is processed to obtain the incident, reflected and transmitted waves. Figures 4.7 and 4.8 show the incident, reflected and transmitted waves in a voltage versus time graph. For the aluminum specimen, the fraction of transmitted waves is relatively smaller than for the Mars 300. Using the calculation procedures mentioned in Chapter 3 for TSHB experiment, stress-strain graphs and strain rates were determined for Mars 300 and Aluminum 5083 – H131 Alloy specimens.

The behavior of the materials during torsion loading can be studied by the three segments in a stress-strain graph. The three segments are namely the elastic deformation region followed by regions of adiabatic heating and stress collapse. All data from experiments are processed to obtain stress-strain graphs and are shown in Table 4.2. Typical stress-strain curves from each of three applied angle of twist for the respective materials (Figures 4.9 to 4.14) and compared for engineering analysis.

The first set and second set comprising of Aluminum 5083 – H131 Alloy and Mars 300 specimens, respectively, were subjected to 6° angle of twist. Likewise, Aluminum 5083 – H131 Alloy and Mars 300 samples were also subjected to 4° and 8° angle of twist using the TSHB. Figure 4.9 to 4.14 show a typical stress-strain graph and information such as yield stress, strain at yield, maximum shear stress and maximum strain rate are computed.

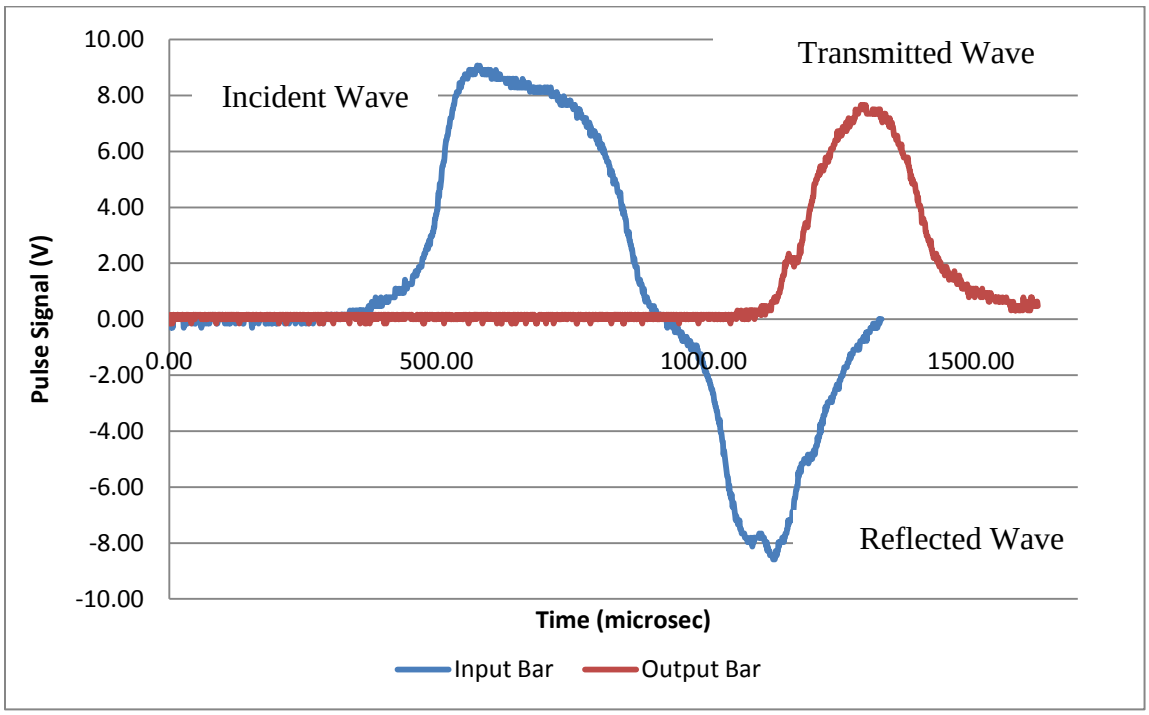

Figure 4.7: Phase Signal versus Time chart showing incident, reflected and transmitted waves recorded by the oscilloscope for Mars 300

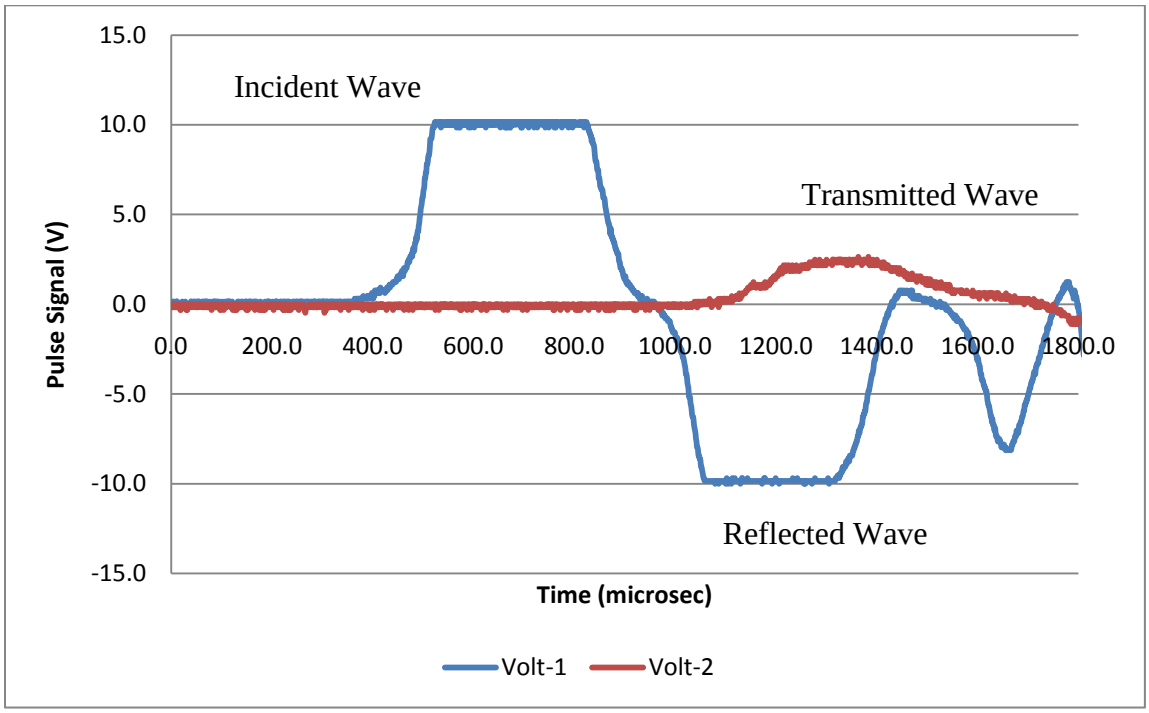

Figure 4.8: Phase Signal versus Time chart showing incident, reflected and transmitted waves recorded by the oscilloscope for Aluminum 5083 – H131 Alloy

The summary of results from torsion loading experiments is given in Table 4.2. From the stress-strain curves, a 2% yield offset was used in determining the yield stress and strain at yield. The region between the yield point and maximum flow stress is where plastic deformation occurs. The process of strain hardening dominates the plastic deformation region and is succeeded by thermal softening upon reaching the maximum flow stress. The region of thermal softening is important as the competition between strain hardening and thermal softening causes localised heating referred to as adiabatic heating. The flow stress decreases with increasing strain to a certain point when there is a drastic drop in the flow stress leading to a region of stress collapse.

The comparison of the three different angles of twist is shown in Figures 4.15 and 4.16 to study the stress-strain behaviour of Mars 300 and Aluminum 5083 – H131 Alloy as the angle of twist is increased. For Aluminum 5083 – H131 Alloy specimens, it can be seen that as the angle of twist is increased, the maximum flow stress and the maximum strain rate increases. The range of strain for adiabatic heating was larger in 6° and 8° angle of twist than in 4° angle of twist. In comparison, Mars 300 specimens, exhibited higher maximum flow stress when the angle was increased from 4° angle of twist to 6° or 8° angle of twist. The strains for adiabatic heating range for Mars 300 were lower than that of Aluminum 5083 – H131 Alloy for any given angle of twist. It could also be seen that Mars 300 had larger maximum flow stresses than Aluminum 5083 – H131 Alloy and the occurrence of these large stresses at relatively low strain of 0.04 when compared with Aluminum 5083 – H131 Alloy. It should also be noted that Mars 300 specimens showed a lower range of plastic deformation zone than Aluminum 5083 – H131 Alloy specimens.

Sample No	Material	Angle of Twist	Max Strain Rate (/s)	Max Shear Stress (MPa)	Yield Point (MPa)	Strain at Yield
1	Aluminum	6°	1111.5	1096.4	1040	0.055
2	Aluminum		1127.7	1117.7	1000	0.060
3	Aluminum		1105.5	1181.0	1040	0.050
4	Aluminum		1087.1	1077.9	980	0.050
5	Aluminum	4°	1064.9	1011.4	880	0.055
6	Aluminum		1105.4	1050.7	960	0.055
7	Aluminum		1017.1	1003.5	900	0.050
8	Aluminum		1035.7	998.0	920	0.050
9	Aluminum	8°	1189.5	1095.6	960	0.045
10	Aluminum		1139.6	1142.8	900	0.045
11	Aluminum		1191.5	1130.6	1000	0.045
1	Maraging Steel	6°	1072.4	1393.4	1320	0.01
2	Maraging Steel		1120.4	1431.2	1320	0.005
3	Maraging Steel		1154.2	1342.6	1320	0.01
4	Maraging Steel	4°	614.6	1164.0	1040	0.024
5	Maraging Steel		643.8	1419.0	1280	0.015
6	Maraging Steel		957.4	698.6	580	0.060
7	Maraging Steel		687.3	1148.8	880	0.036
8	Maraging Steel	8°	1023.7	1390.2	1200	0.030
9	Maraging Steel		1072.1	1380.1	1300	0.020
10	Maraging Steel		1045.6	1378.9	1280	0.025

Table 4.2: Summary of results from torsion loading experiments

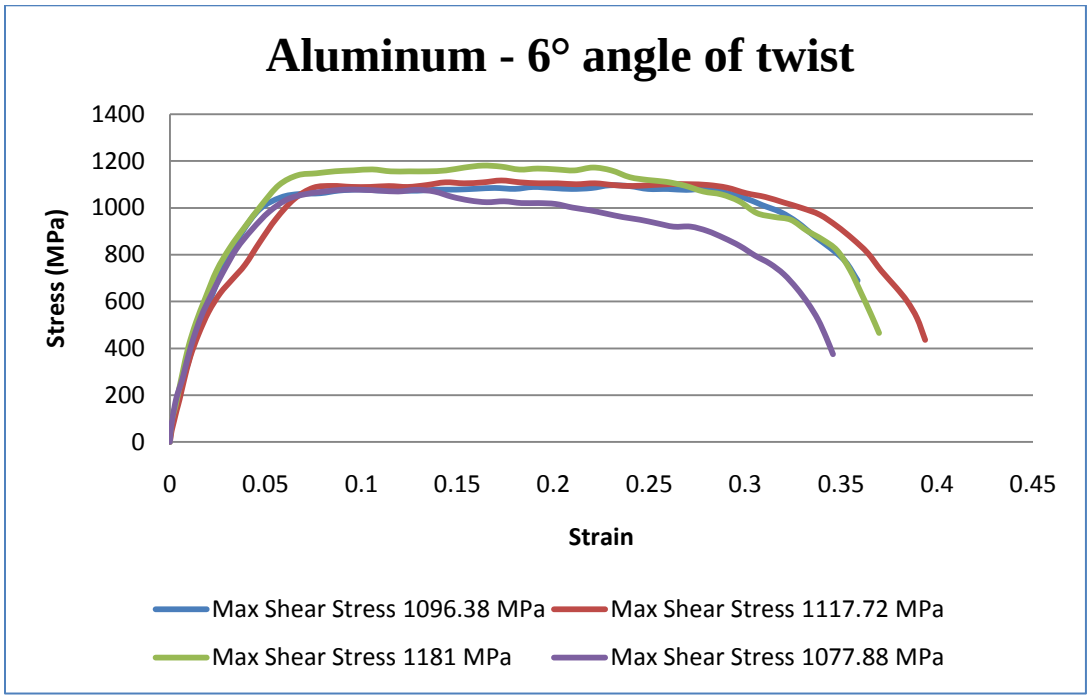

Figure 4.9: Stress-strain curves for Aluminum 5083 – H131 Alloy specimens

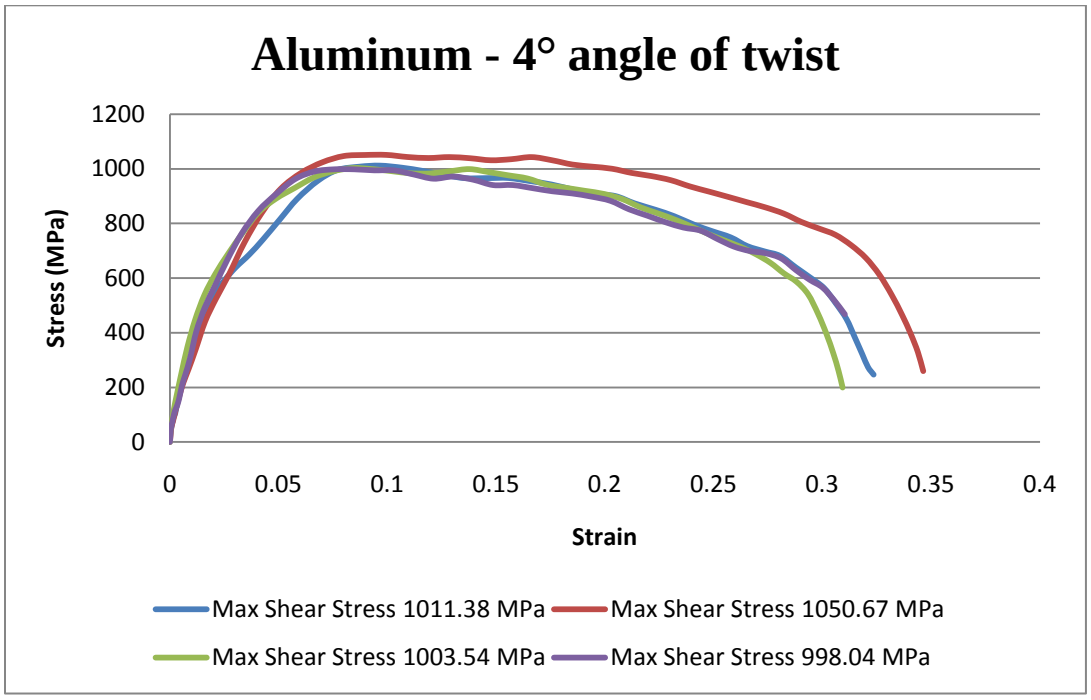

Figure 4.10: Stress-strain curves for Aluminum 5083 – H131 Alloy specimens

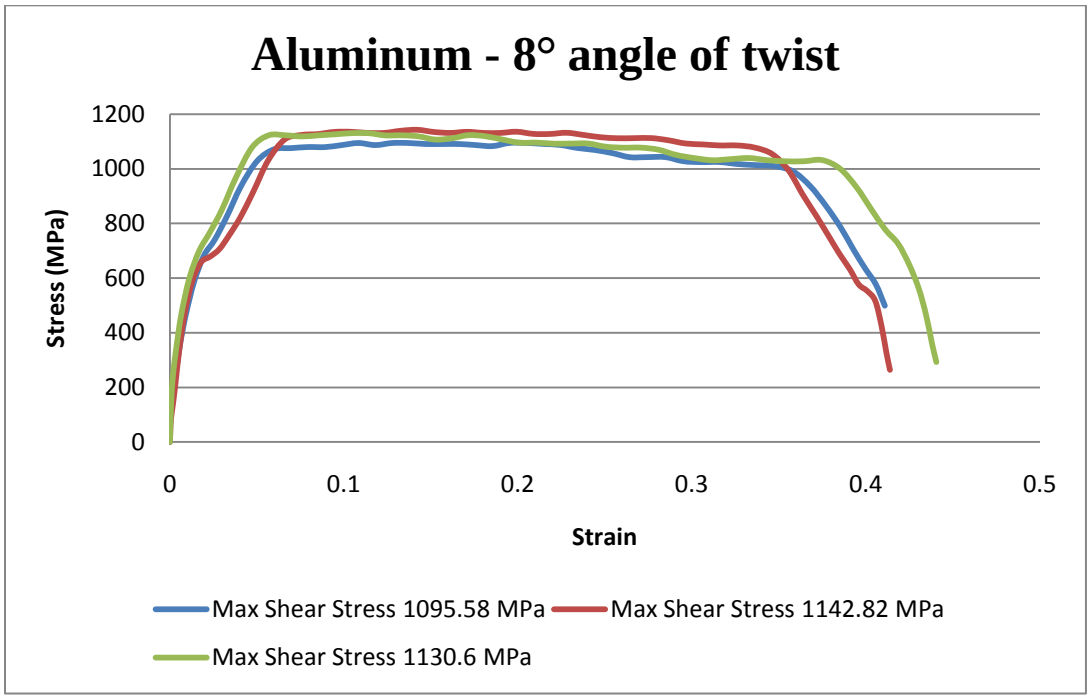

Figure 4.11: Stress-strain curves for Aluminum 5083 – H131 Alloy specimens

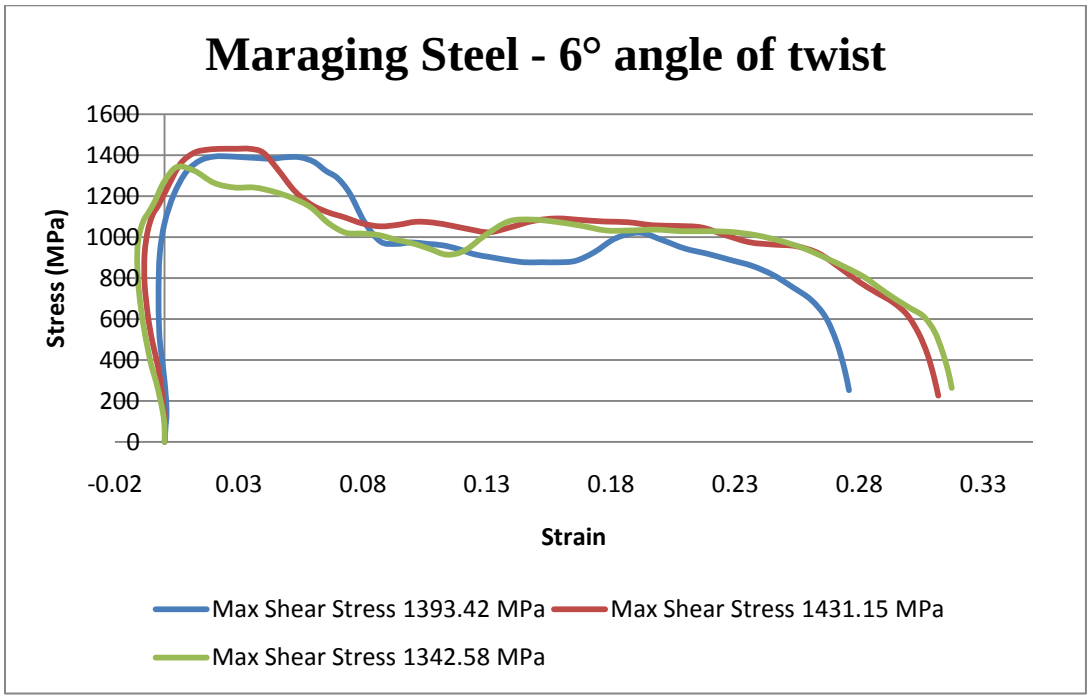

Figure 4.12: Stress-strain curves for Mars 300 specimens

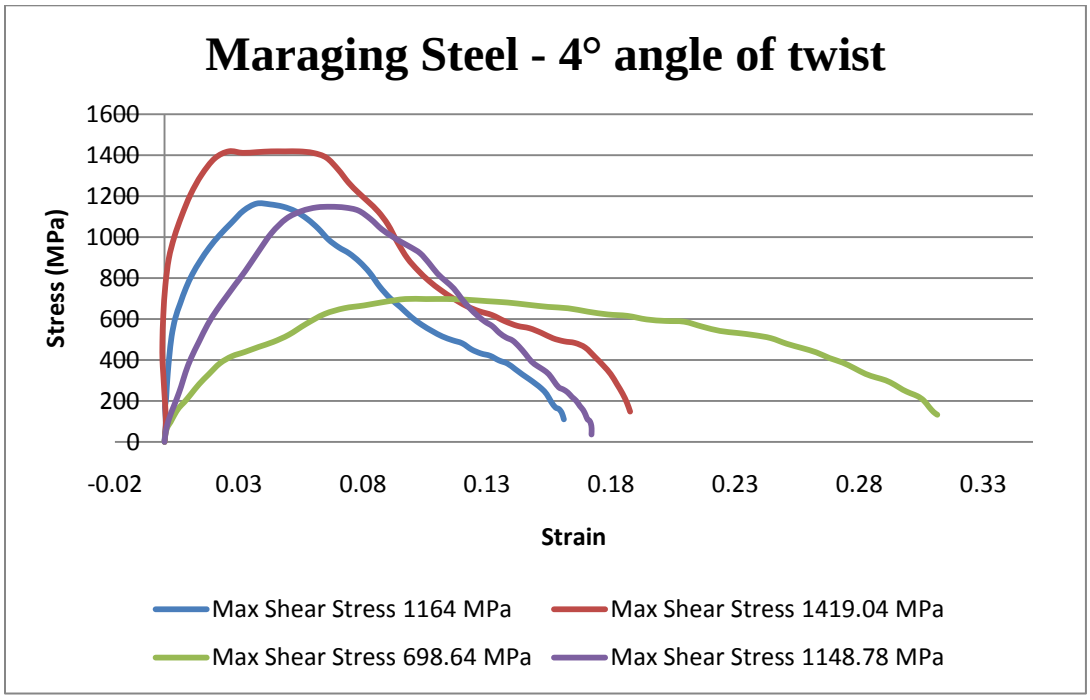

Figure 4.13: Stress-strain curves for Mars 300 specimens

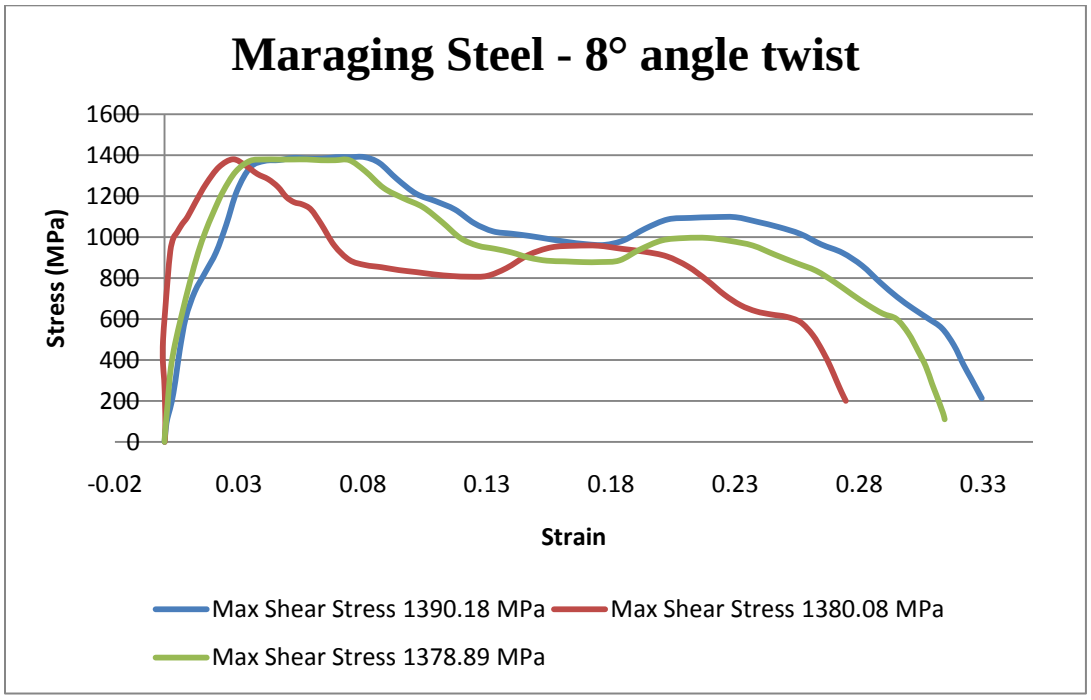

Figure 4.14: Stress-strain curves for Mars 300 specimens

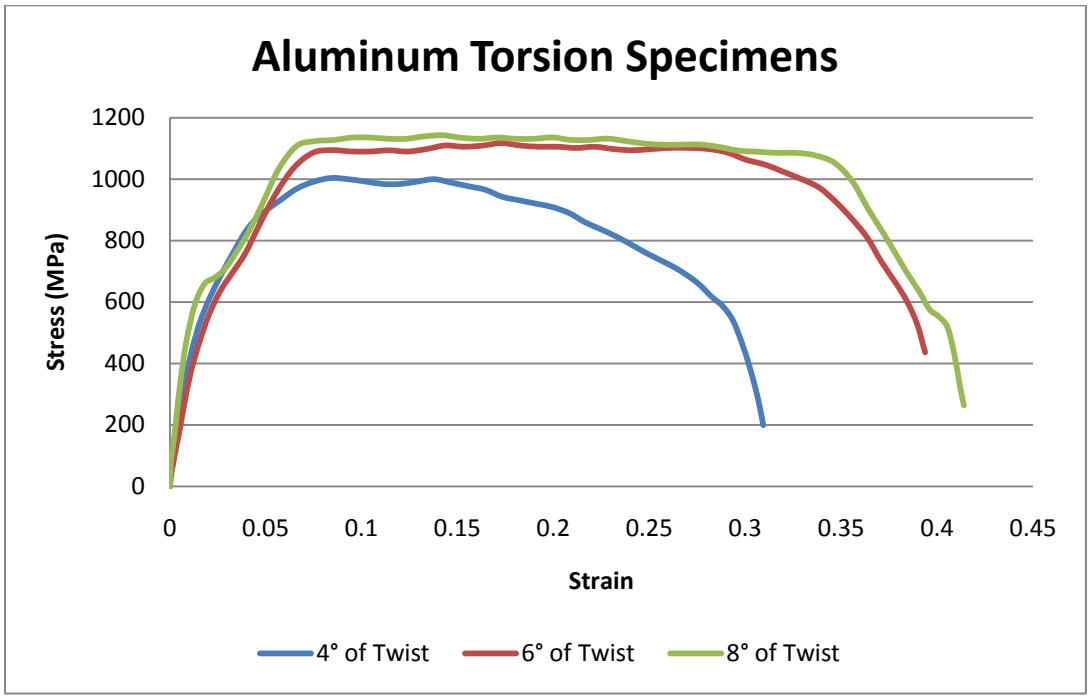

Figure 4.15: Typical stress-strain curves for selected Aluminum 5083 – H131 Alloy specimens at different angle of twist

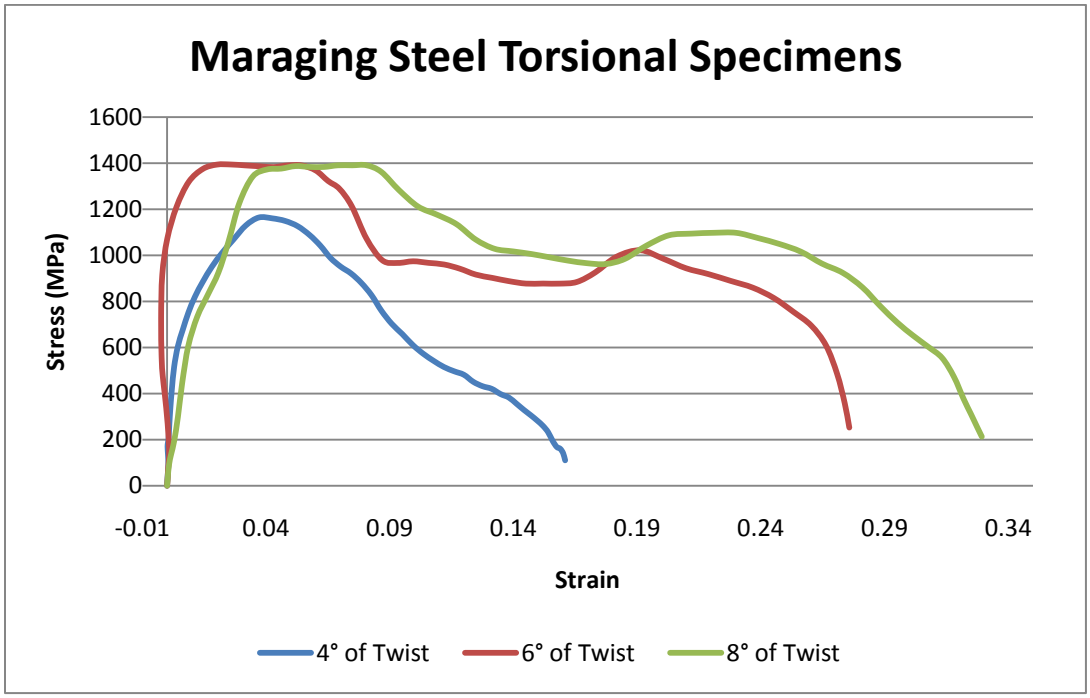

Figure 4.16: Typical stress-strain curves for selected Mars 300 specimens at different angle of twist

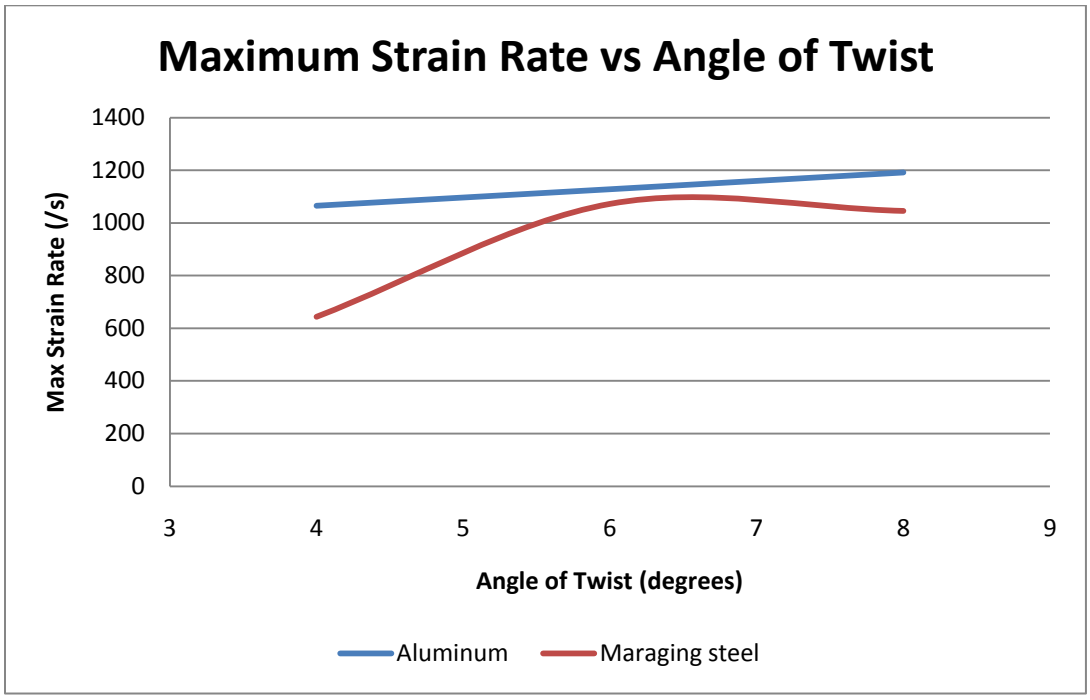

Figure 4.17: Comparison on the effect of maximum strain rate on angle of twist

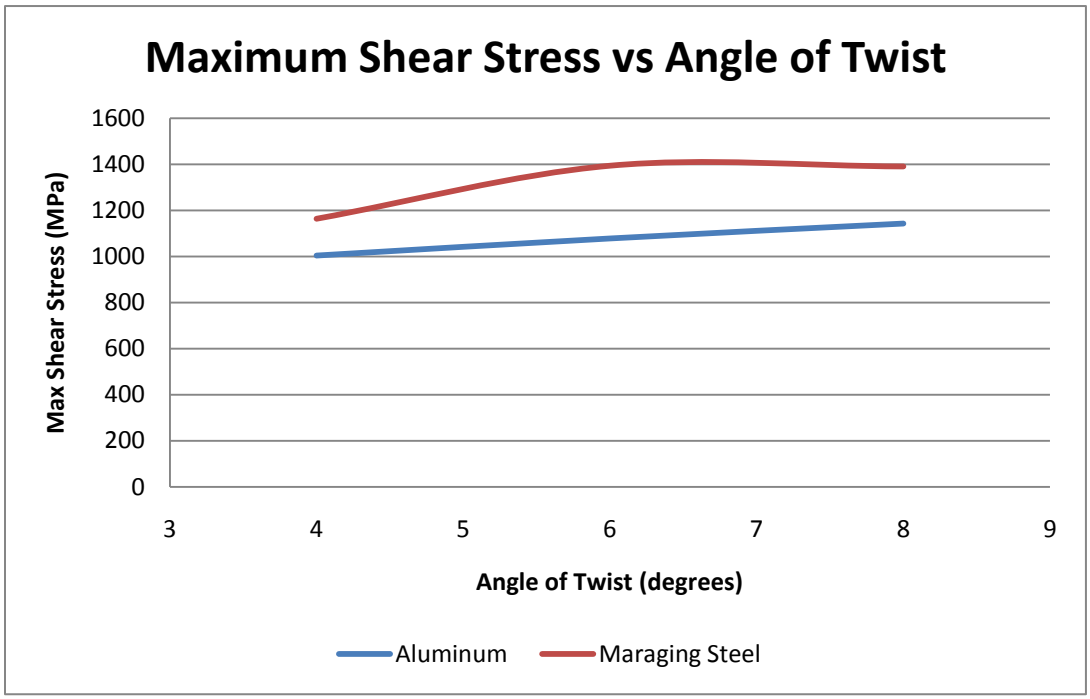

Figure 4.18: Comparison on the effect of maximum shear stress on angle of twist

The strain rate sensitivity of a material is calculated based on the natural logarithm shear stress versus the natural logarithm of strain rate at a fixed shear strain (Shen, et al. 2006) and is given by the slope, m:

$$m = \left(\frac{\partial log\tau}{\partial log\,\dot{\gamma}}\right)_{\gamma}$$

Based on the study by Mercier and Molinari (1997) and Wright (2003), materials with high strain rate sensitivity have higher stability and are less likely to form adiabatic shear bands than materials with low strain rate sensitivity.

Three different strains of 0.07, 0.10 and 0.15 were chosen for Aluminum 5083 – H131 Alloy specimens. The first constant strain is selected after the strain at yield followed by selection of the second constant strain at maximum flow stress and the third constant strain before stress collapse. The natural logarithm of shear stress against the natural logarithm of average strain rate for all curves is plotted. The strain rate sensitivity of the materials is given by the resulting slope, m, of the plot. Similarly, strain rate sensitivity is calculated for Mars 300 and presented in Table 4.3.

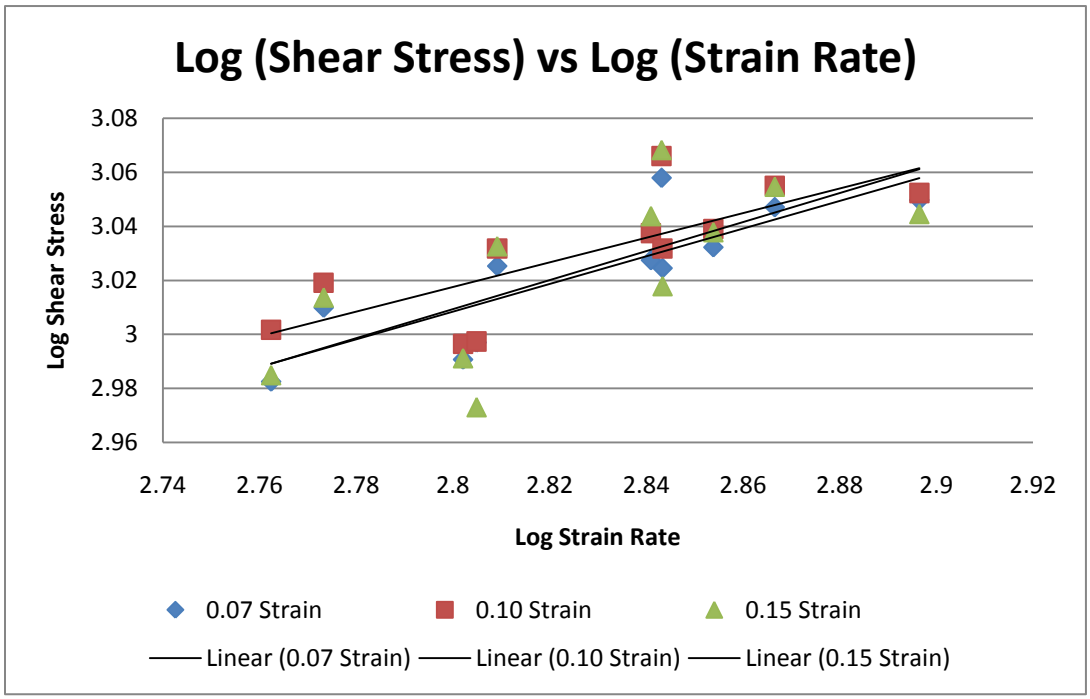

Figure 4.19: The logarithmic plot of shear stress versus strain rate to obtain Strain Rate Sensitivity for Aluminum 5083 – H131 Alloy specimens

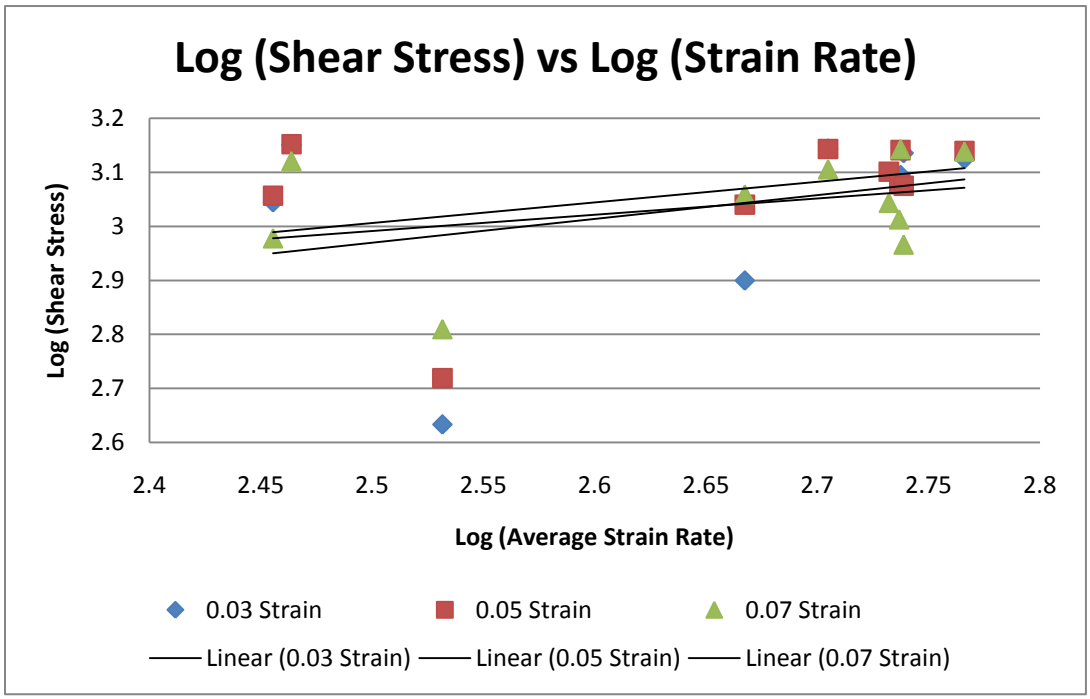

Figure 4.20: The logarithmic plot of shear stress versus strain rate to obtain Strain Rate Sensitivity for Mars 300 specimens

Material	Strain Rate Sensitivity		
	Strain = 0.07	Strain = 0.10	Strain = 0.15
Aluminum 5083 – H131 Alloy	0.51	0.46	0.54
	Strain = 0.03	Strain = 0.05	Strain = 0.07
Maraging Steel	0.44	0.38	0.30

Table 4.3: Strain rate sensitivities for Aluminum and Maraging steel specimens

4.4 Microscopic Investigation using Optical Microscopy

Specimens from impact loading (SHPB) and torsion loading (TSHB) experiments were investigated for evaluation on the formation of ASBs. The specimens were investigated using optical microscopy for microstructural study and occurrence of ASBs. Advanced microscopic techniques such as Atomic Force Microscopy (AFM) and Scanning Electron Microscopy (SEM) were used for detailed analysis on the microstructure.

4.4.1 Maraging Steel 300 specimens from impact loading

Observation on optical microscopy images for Mars 300 specimens showed no shear bands between impact momentums of 32.91 kg.m/s and 40.04 kg.m/s. From Figures 4.21 to 4.23, the microstructure of Mars 300 appears to have needle like martensitic structures. As the impact momentum is increased to 44.54 kg.m/s, ASB were found in Mars 300. Figures 4.24 and 4.25 show the microstructure of Mars 300 with the presence of deformed bands and white etching bands at a magnification of 100x. Figure 4.26 shows the initiation region of deformed bands in Mars 300 while Figure 4.27 shows the distinctive white-etching (transformed) band at a magnification of 200x.

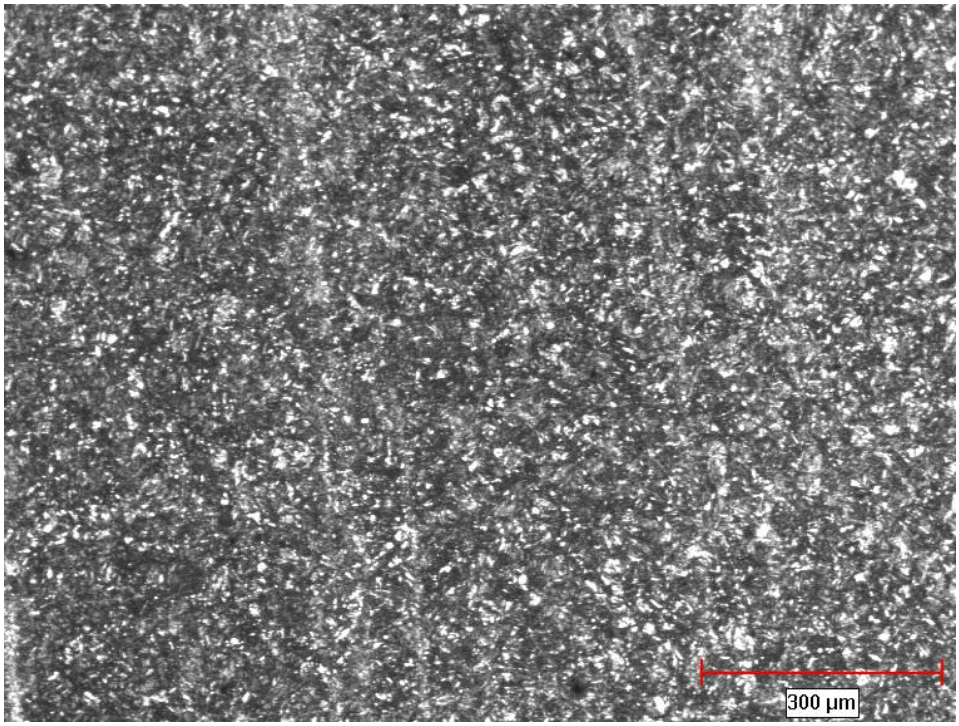

Figure 4.21: Mars 300 specimen (1) impacted at 32.91 kg.m/s (no ASB)

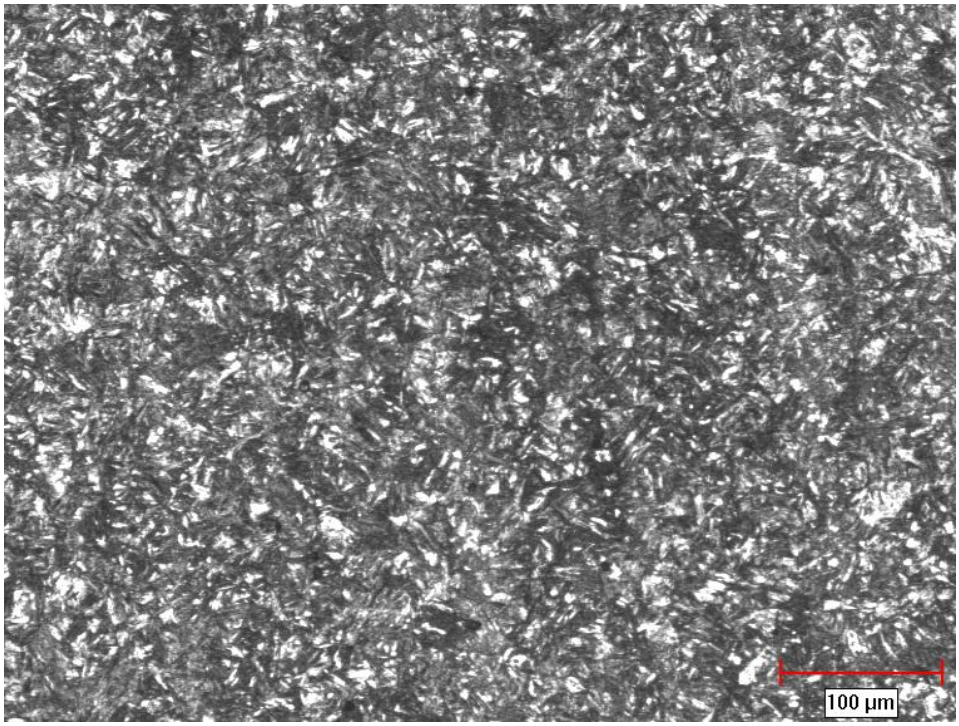

Figure 4.22: Mars 300 specimen (4) impacted at 40.04 kg.m/s (no ASB)

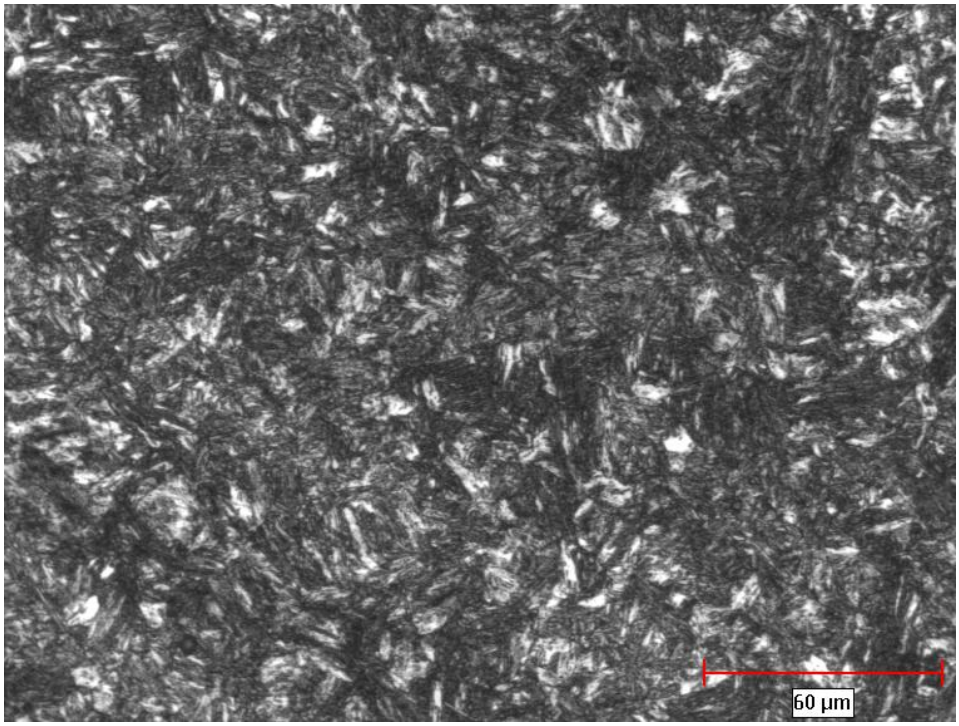

Figure 4.23: Mars 300 specimen (4) impacted at 40.04 kg.m/s (no ASB)

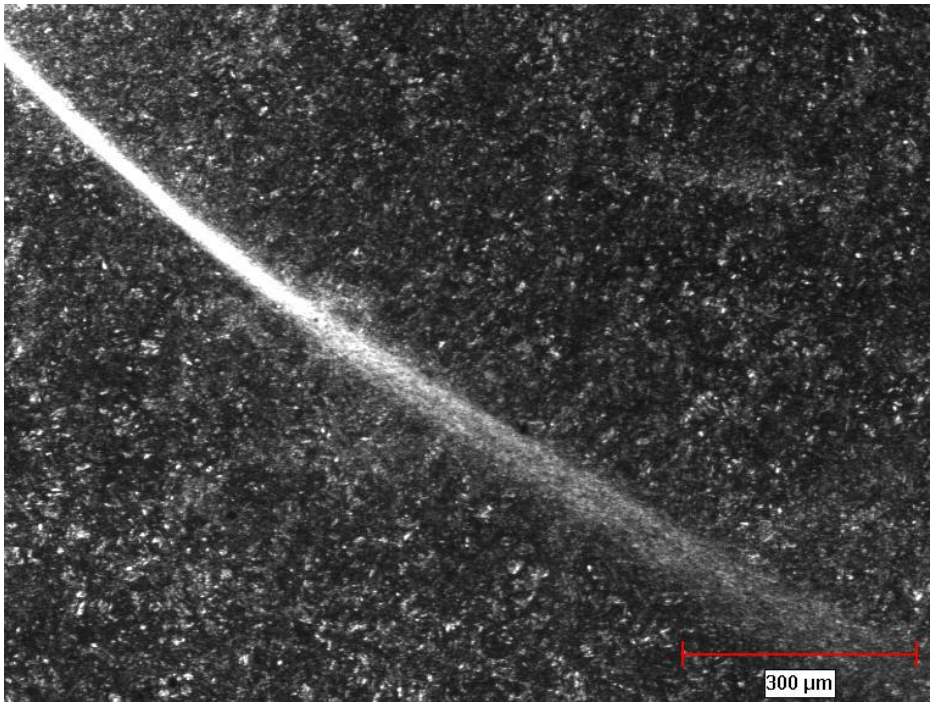

Figure 4.24: Mars 300 specimen (5) impacted at 44.54 kg.m/s (showing deformed and white etching bands)

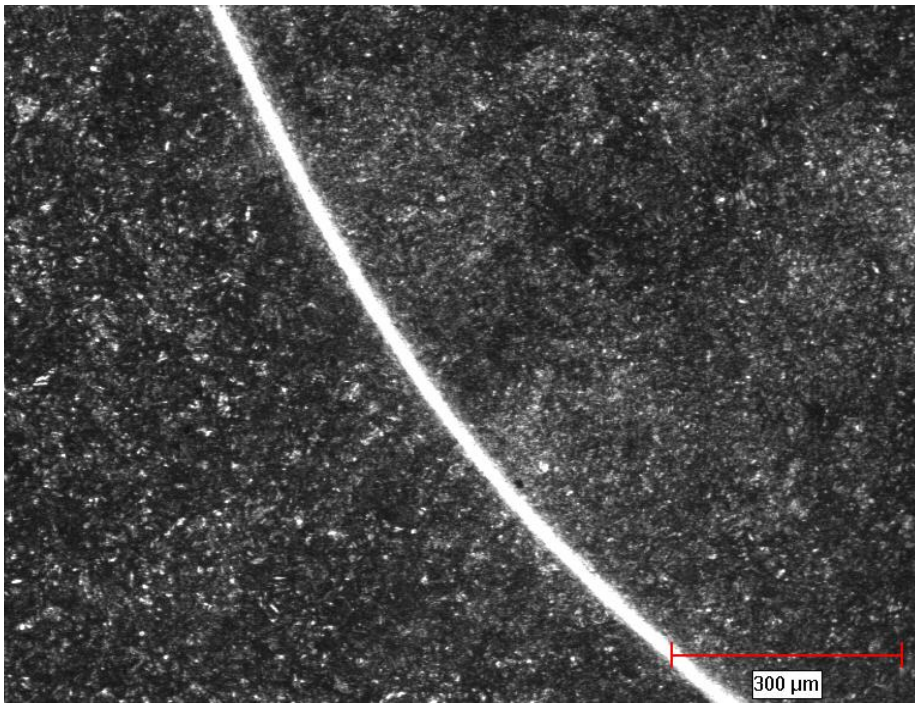

Figure 4.25: Mars 300 specimen (5) impacted at 44.54 kg.m/s (showing white etching bands)

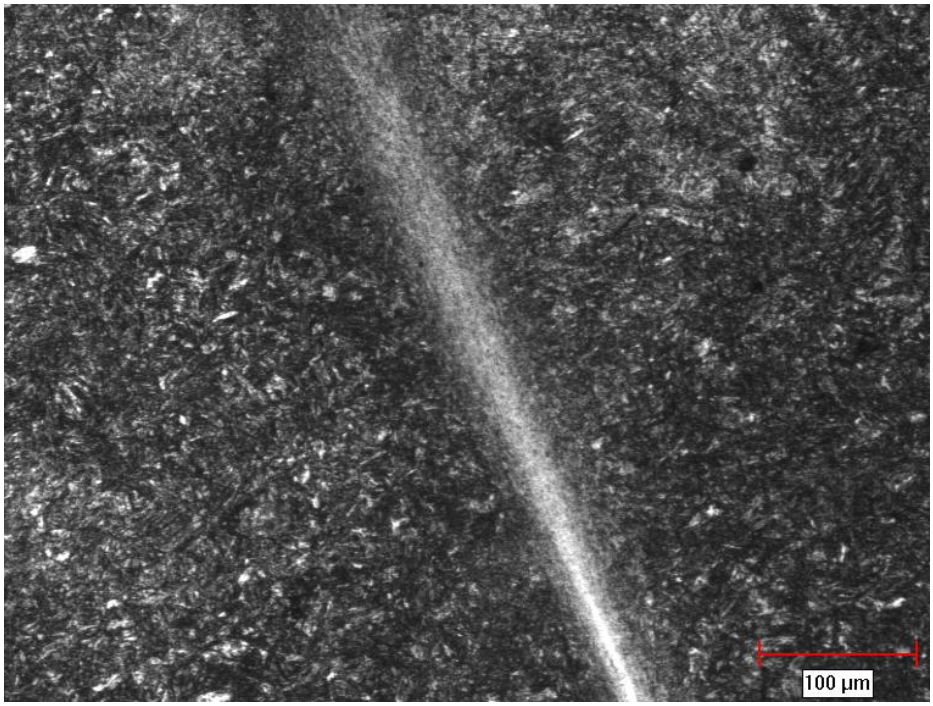

Figure 4.26: Mars 300 specimen (5) impacted at 44.54 kg.m/s (showing deformed bands)

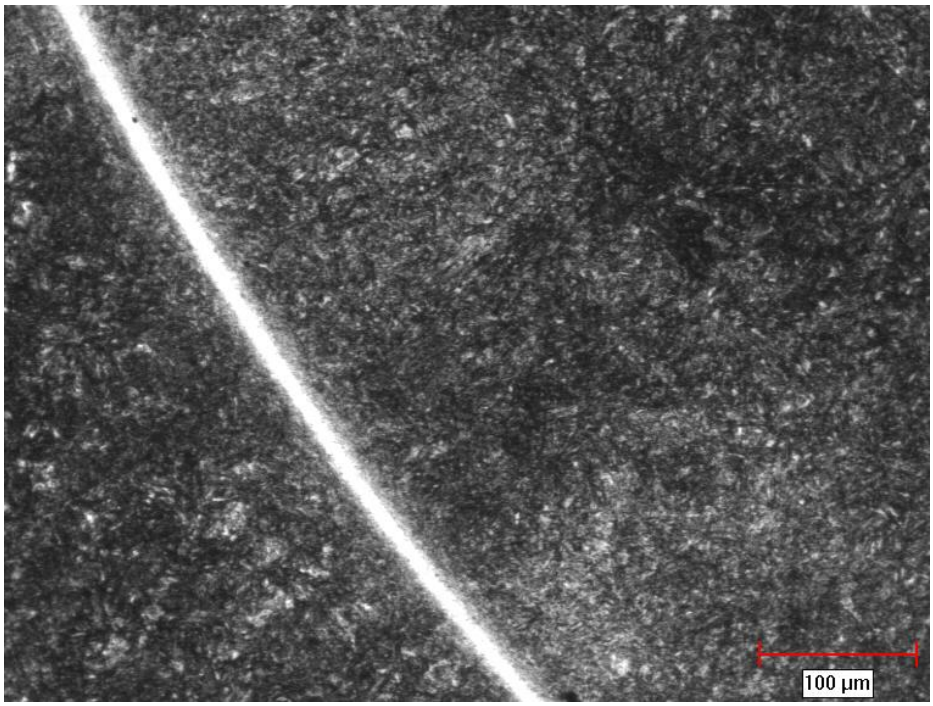

Figure 4.27: Mars 300 specimen (5) impacted at 44.54 kg.m/s (showing white etching bands)

4.4.2 High Hardness Armor (HHA) specimens from impact loading

HHA specimens showed deformed ASB at impact momentums of 32.91 kg.m/s, 40.1 kg.m/s and 45.49 kg.m/s. Figure 4.28 shows that sample subjected to an impact momentum of 32.91 kgm/s showed deformed bands at the edge of the circular specimen. Figures 4.29 and 4.30 shows the deformed bands when the impact momentum is increased to 40.1 kgm/s. As the impact momentum is further increased to 45.49 kgm/s deformed bands appeared more distinctive than at lower impact momentums. Therefore, at higher impact momentums, ASBs in HHA appear thicker and subsequent increase leads to fracture of specimen.

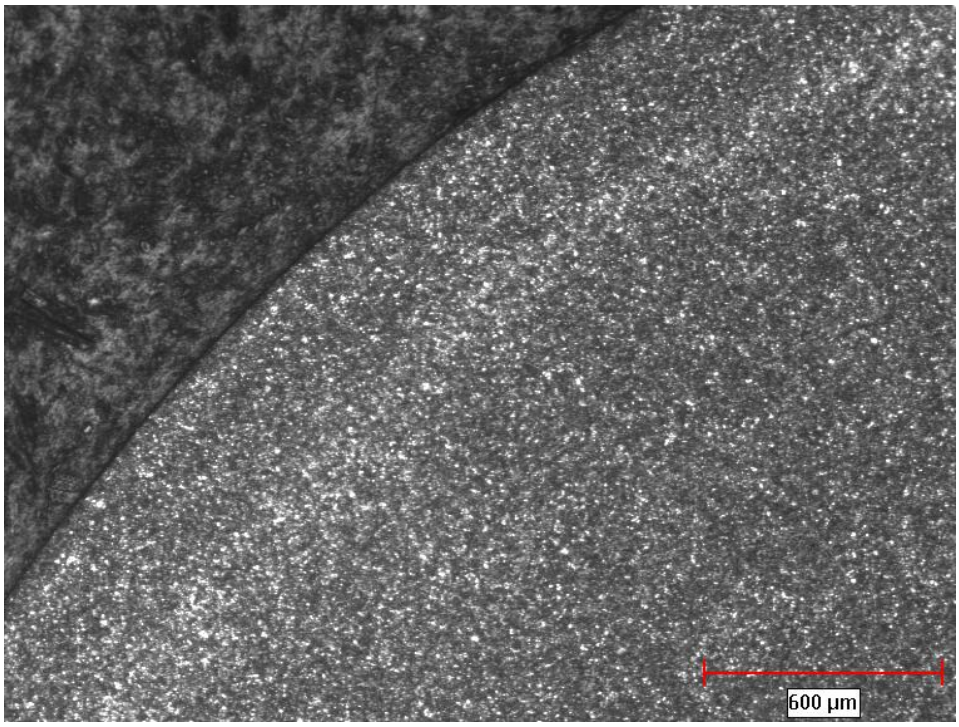

Figure 4.28: HHA specimen (2) impacted at 32.91 kg.m/s (showing deformed bands)

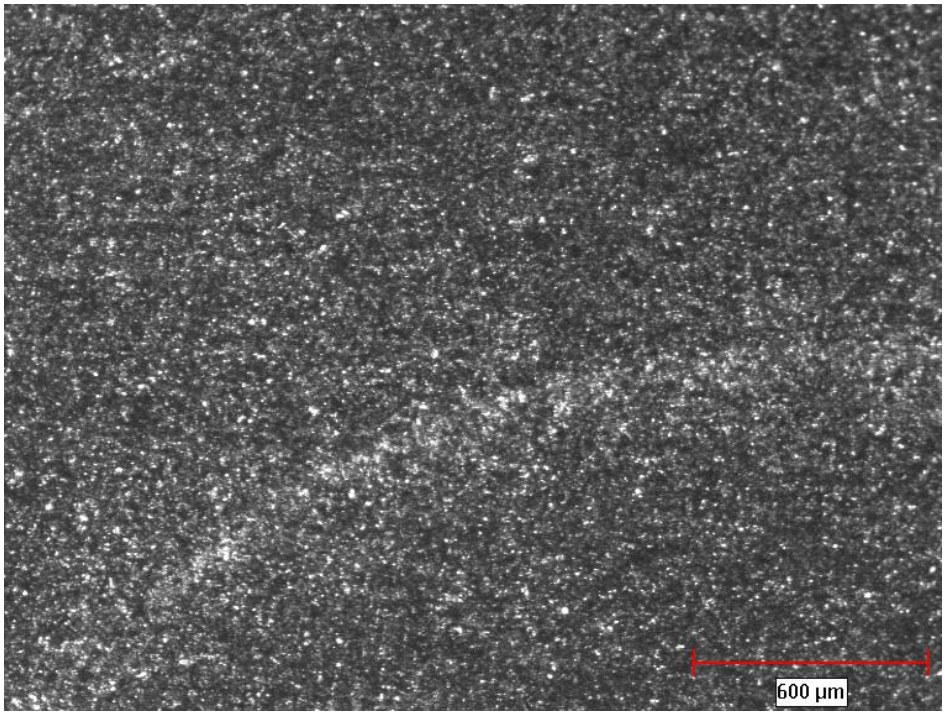

Figure 4.29: HHA specimen (4) impacted at 40.1 kg.m/s (showing deformed bands)

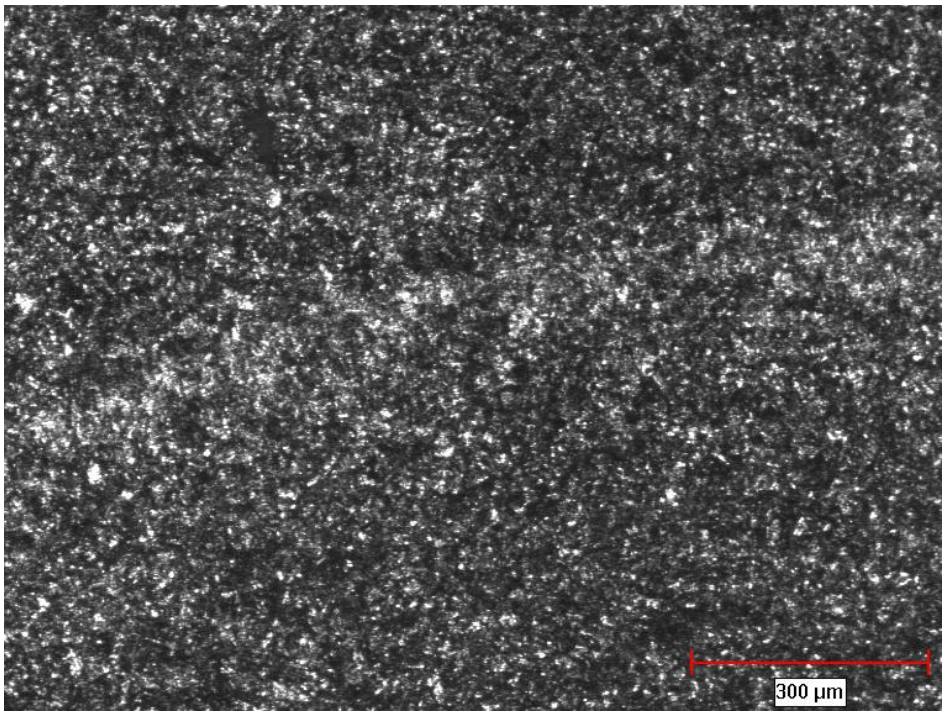

Figure 4.30: HHA specimen (4) impacted at 40.1 kg.m/s (showing deformed bands)

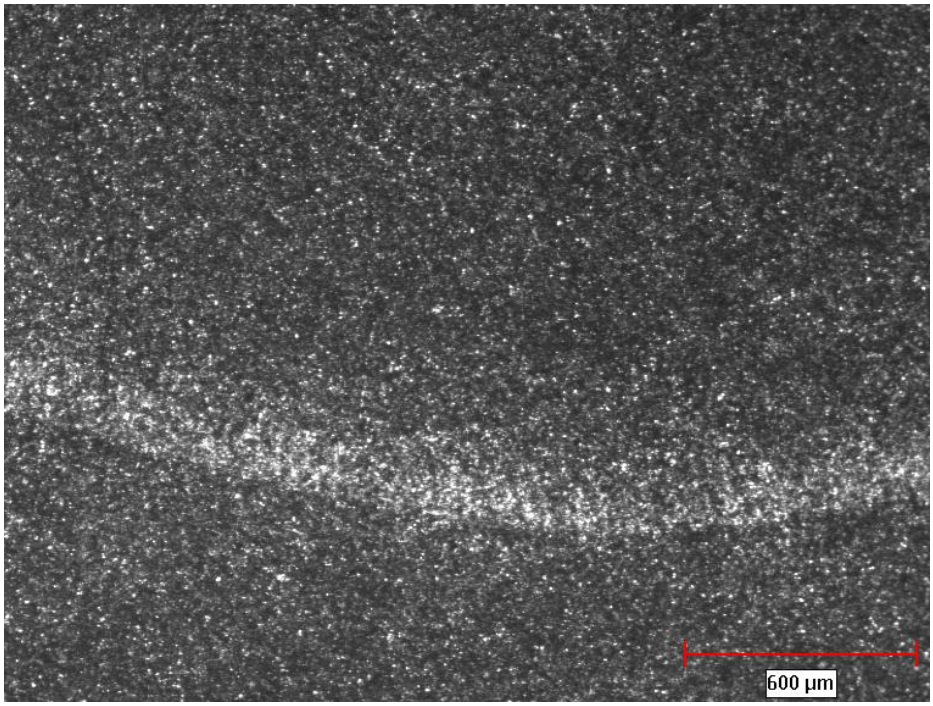

Figure 4.31: HHA specimen (5) impacted at 45.49 kg.m/s (showing deformed bands)

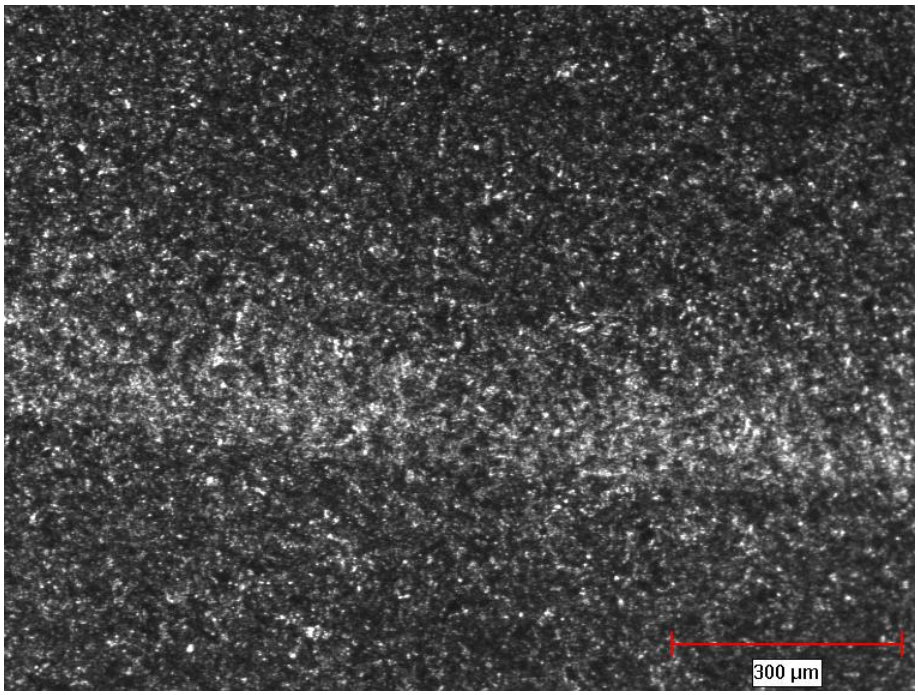

Figure 4.32: HHA specimen (5) impacted at 45.49 kg.m/s (showing deformed bands)

4.4.3 Aluminum 5083 – H131 Alloy specimens from impact loading

A select few samples subjected to impact loading experiments were prepared for microscopic analysis. Figure 4.33 shows the presence of deformed bands in Aluminum 5083 – H131 Alloy specimen subjected to impact momentum of 28.63 kg.m/s. The deformed bands were observed at the edge of the circular specimen. The optical microscopy images show clear evidence on reorientation of grains in the region of deformed bands (Figures 4.34 – 4.35). From Figures 4.36 – 4.37, it is also seen that increasing the impact momentum to 32.91 kg.m/s showed thick deformed bands.

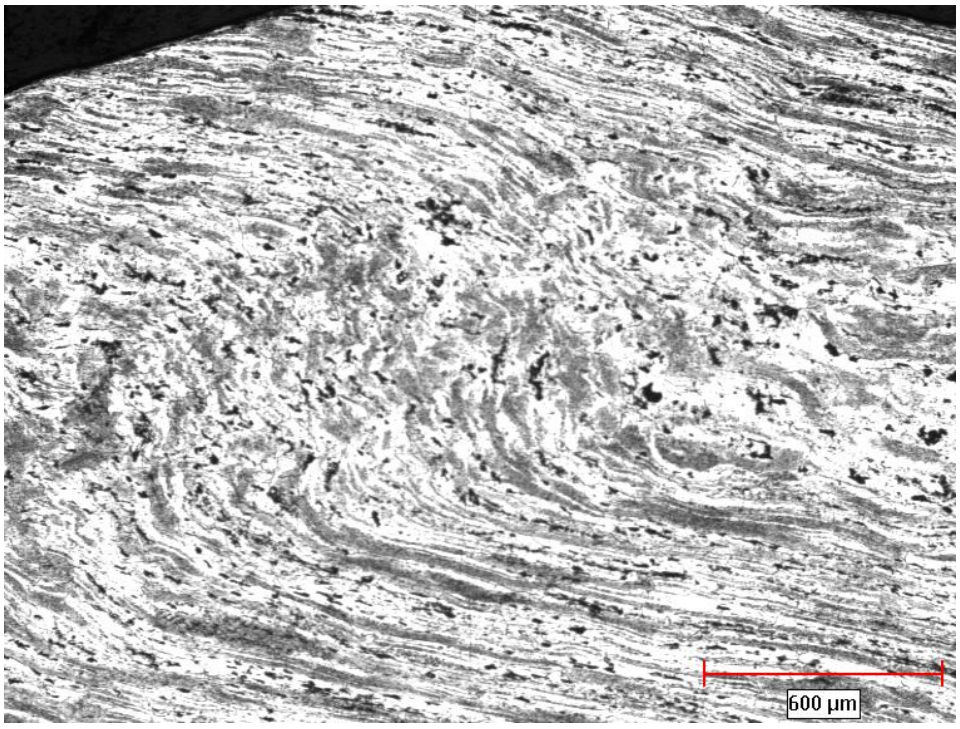

Figure 4.33: Aluminum specimen (3) impacted at 28.63 kg.m/s (showing deformed band)

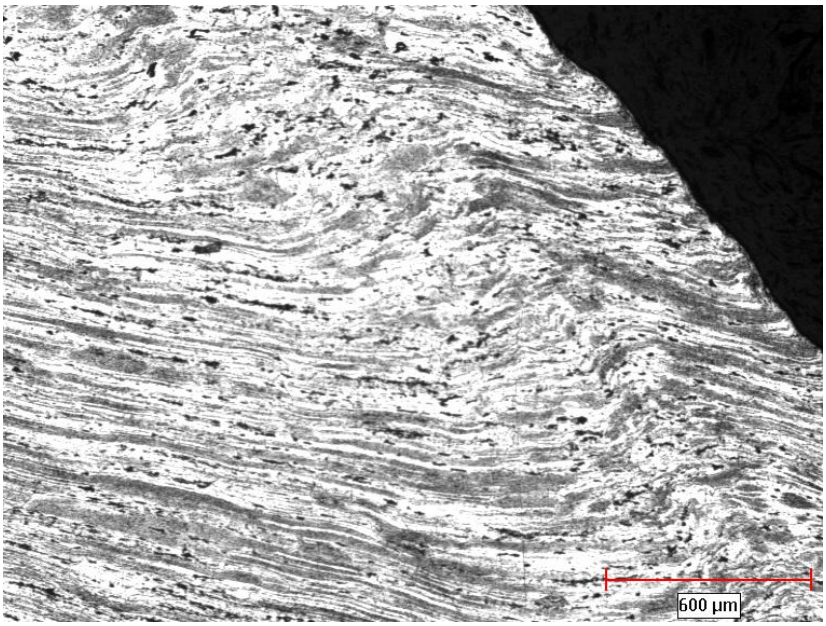

Figure 4.34: Aluminum specimen (3) impacted at 28.63 kg.m/s (showing deformed band)

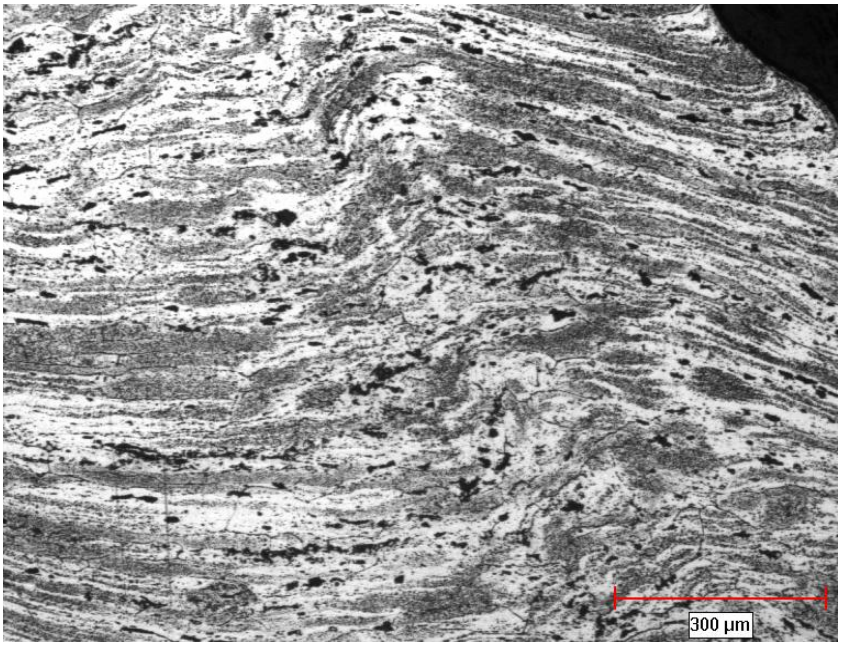

Figure 4.35: Aluminum specimen (3) impacted at 28.63 kg.m/s (showing deformed band)

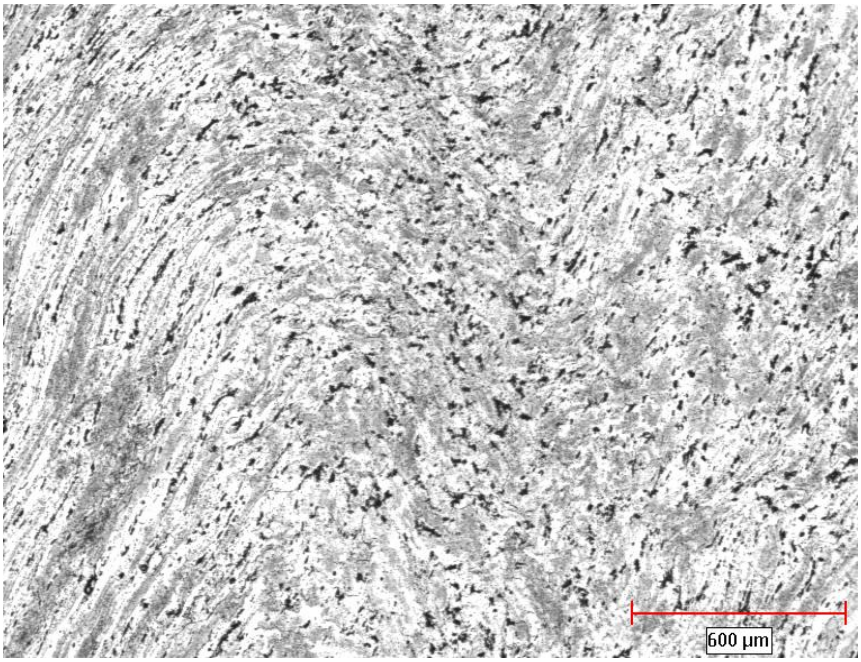

Figure 4.36: Aluminum specimen (1) impacted at 32.91 kg.m/s (showing deformed bands)

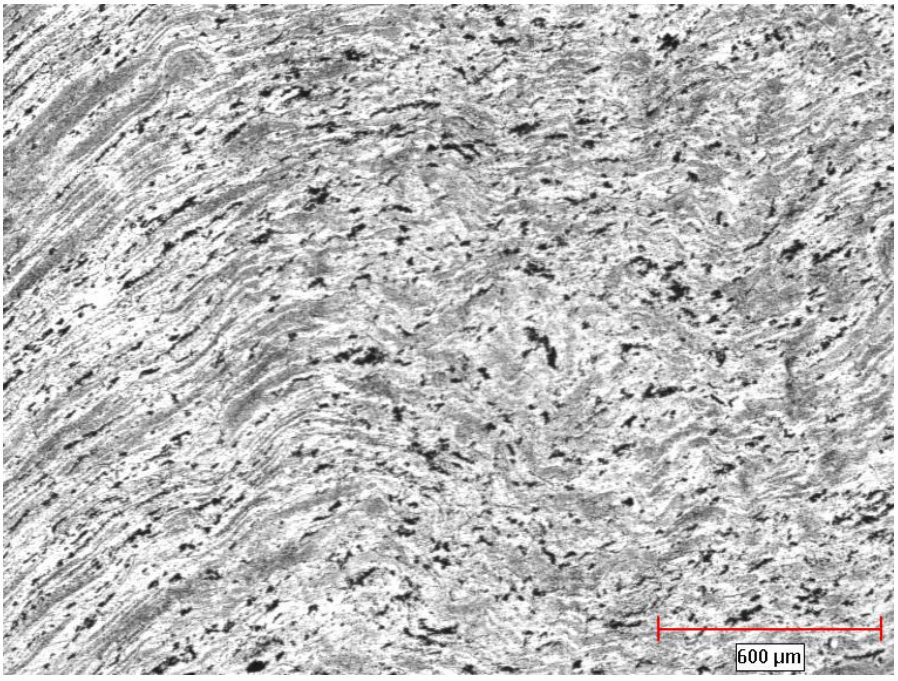

Figure 4.37: Aluminum specimen (2) impacted at 32.91 kg.m/s (showing deformed bands)

4.4.4 Aluminum 5083 – H131 Alloy specimens from torsion loading

Hexagonally shaped Aluminum 5083 – H131 Alloy specimens were subjected to 4°, 6° and 8° angle of twist and sectioned longitudinally for microscopic analysis. Specimens subjected to 8° angle of twist showed clear deformed bands at the narrow sections of the thin-walled tube specimen. Figures 4.38 and 4.39 shows the reorientation of grains at the thin sections. Fracture of specimen occurred at the other end of the specimen along the direction of the shear bands. From Figures 4.40 and 4.41, it is evident that a change in grain direction is an important factor for the initiation of crack sites. Figure 4.42 also shows the crack propagation at the thin sections of another Aluminum 5083 – H131 Alloy specimen.

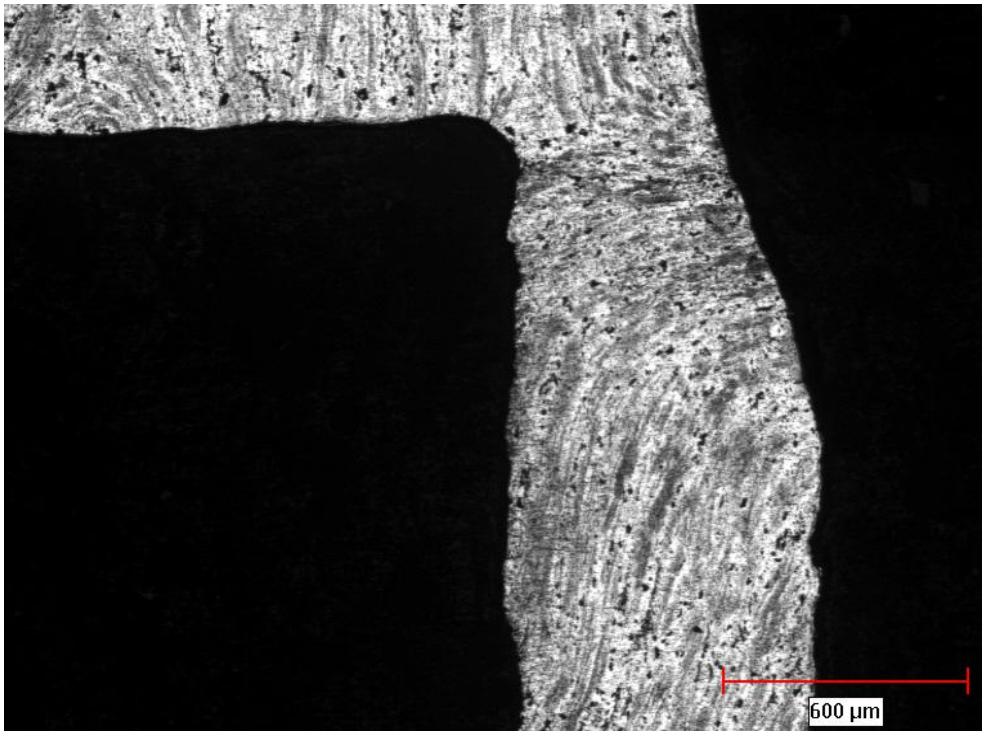

Figure 4.38: Aluminum specimen (10) showing deformed bands at 8° angle of twist

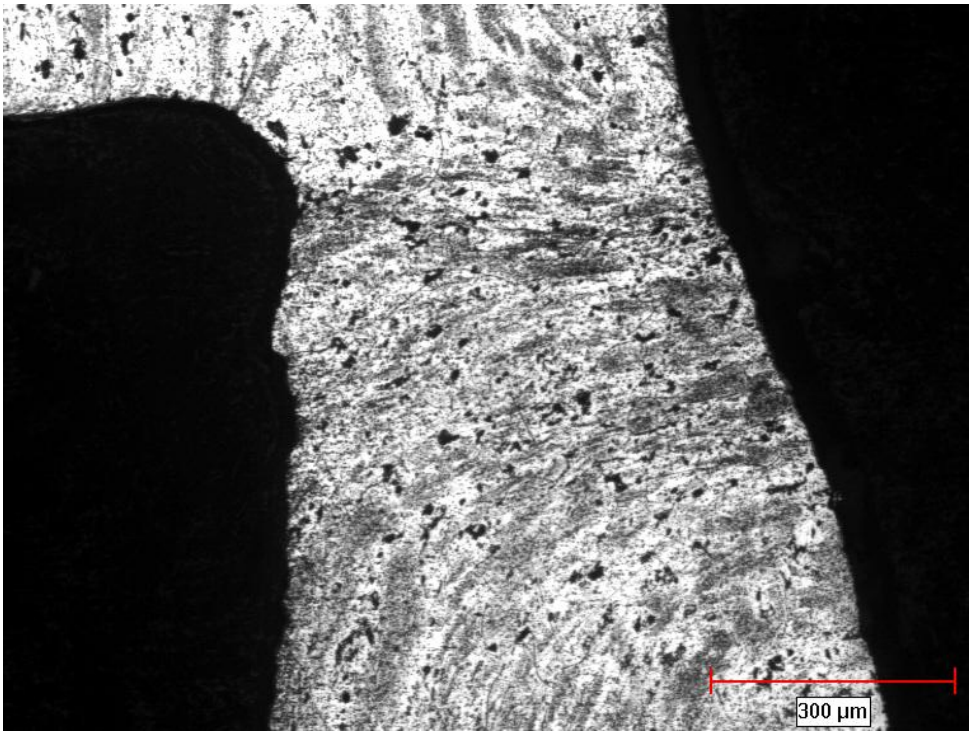

Figure 4.39: Aluminum specimen (10) showing deformed bands at 8° angle of twist

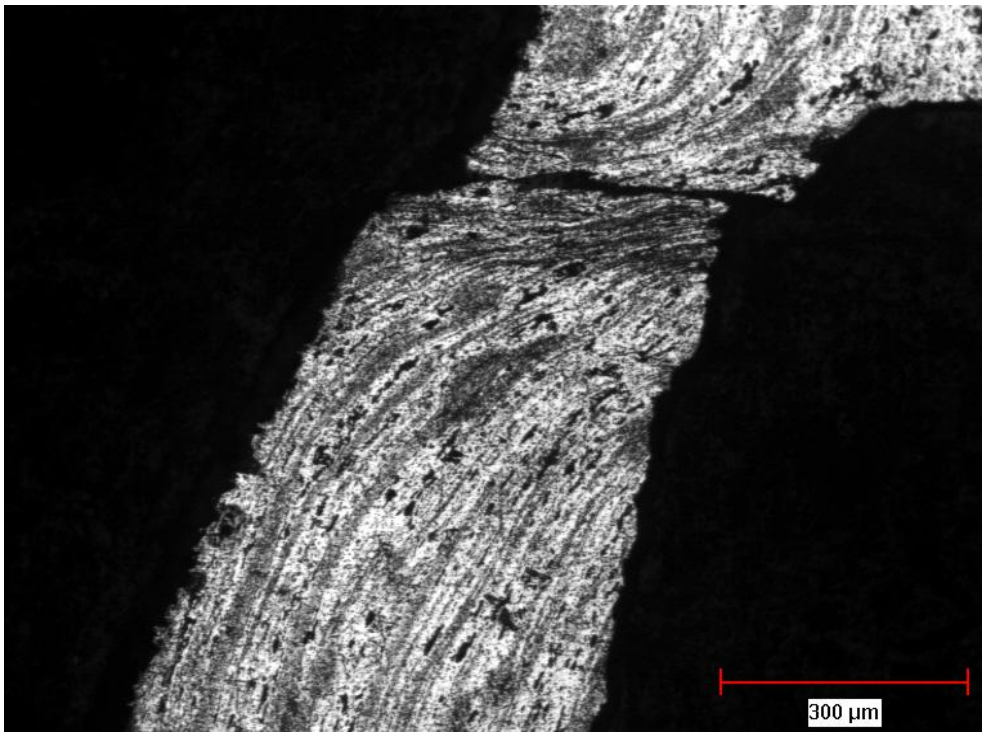

Figure 4.40: Aluminum specimen (10) showing crack at the site of ASB

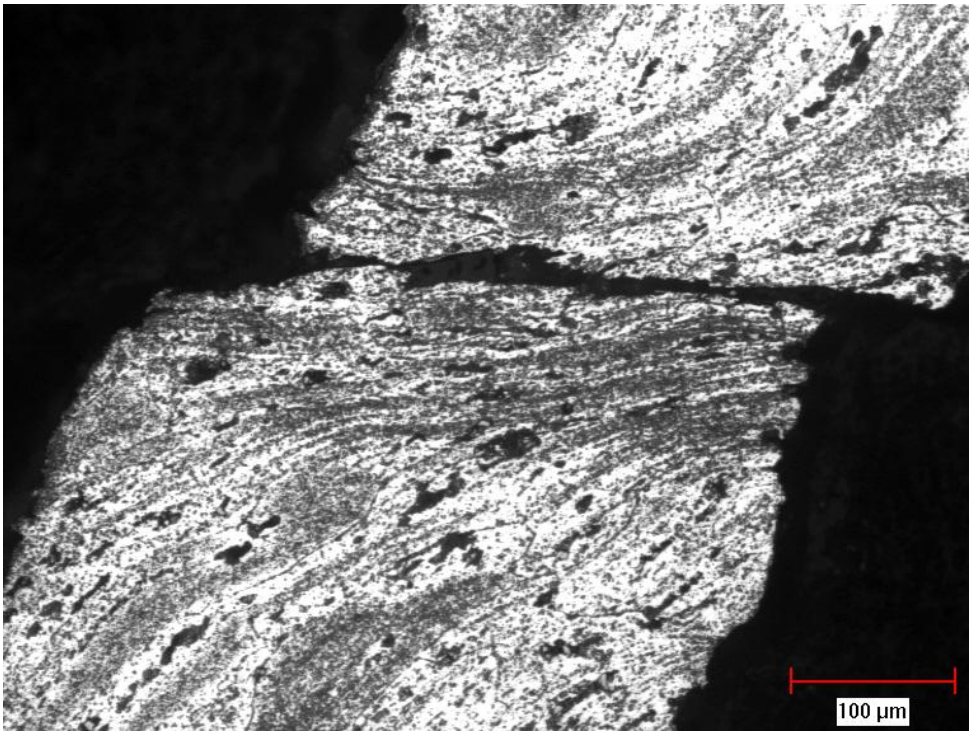

Figure 4.41: Aluminum specimen (10) showing crack at the site of ASB

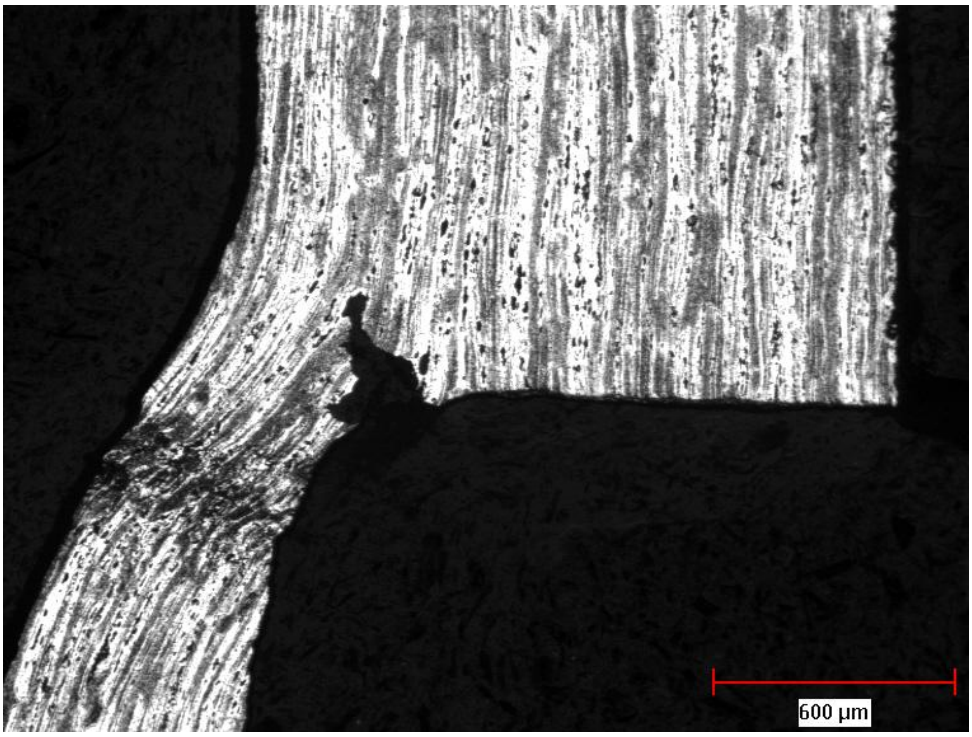

Figure 4.42: Aluminum specimen (11) showing crack initiation

4.4.5 Maraging Steel 300 specimens from torsion loading

Maraging steel 300 (Mars 300) specimens were also subjected to 4°, 6° and 8° angle of twist. Fracture occurred at the thin sections of the hexagonal shaped specimens. None of the specimens investigated using the TSHB showed ASB. Figures 4.43 and 4.44 showed fracture at the thin-walled sections of the specimen.

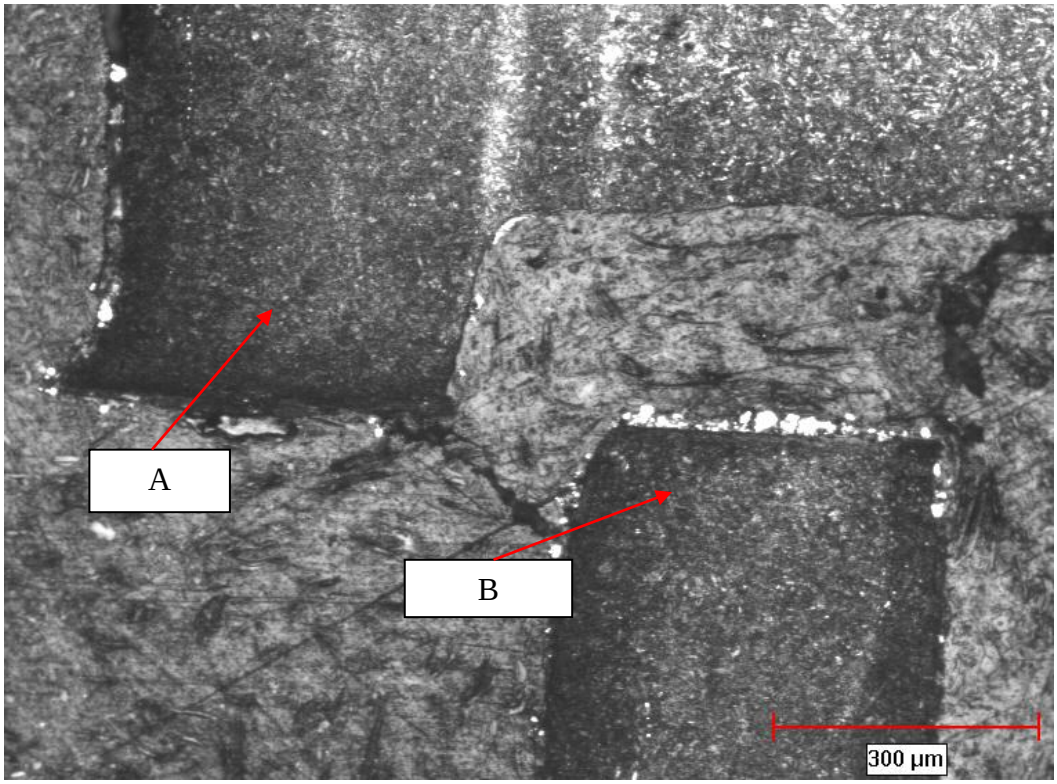

Figure 4.43: Mars 300 specimen (9) showing fracture. Sections A and B are fractured segments of the thin-walled tube specimen

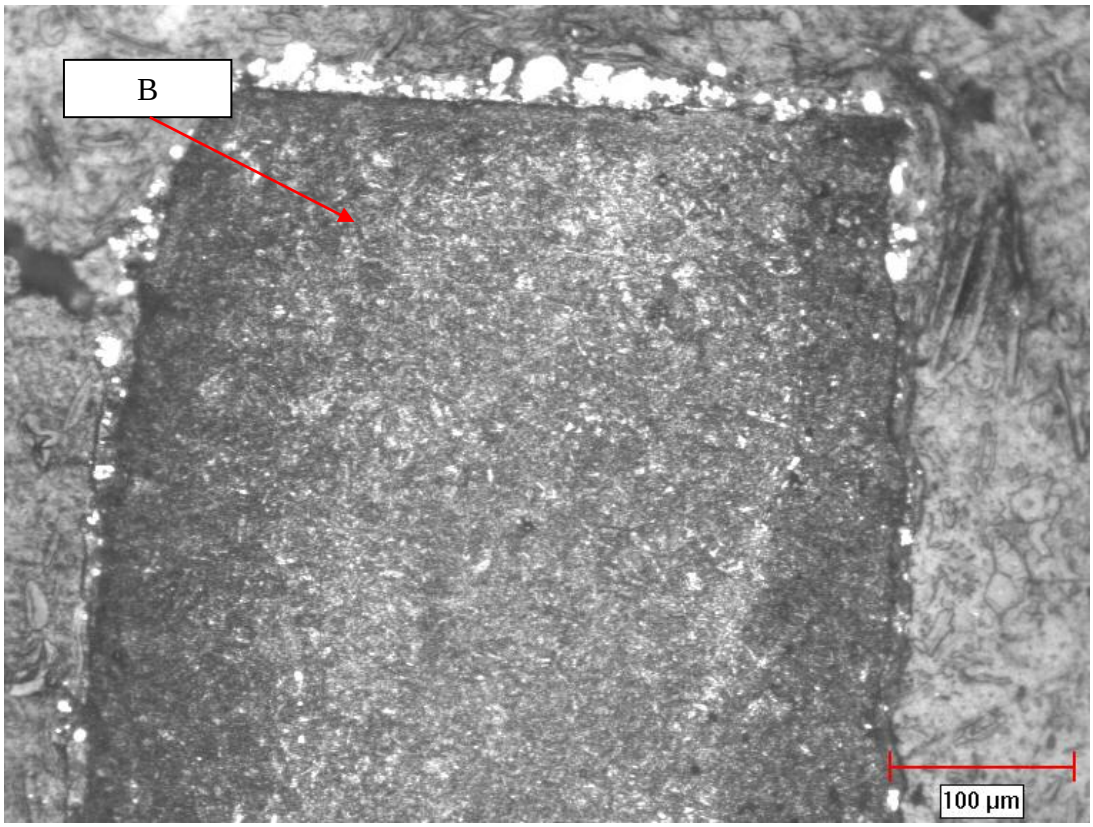

Figure 4.44: Mars 300 specimen (9) at section B of the thin-walled tube specimen

4.5 Microstructural Investigation using Atomic Force Microscopy (AFM)

Microstructural observation of Maraging steel 300 (Mars 300) specimen subjected to an impact momentum of 44.54 kg.m/s revealed the presence of adiabatic shear bands by optical microscopy. As the shear band in Mars 300 appeared thin and more distinctive than HHA samples, using AFM to study the characteristics of such shear band was carried out. The 30μm wide scanning tip of AFM was able to scan sections of the ASB (deformed and white-etching bands). The nital etched specimen was studied at the sections containing deformed and white-etching bands. AFM scans present the topography of the specimen that gives very high accuracy on the surface condition. The preferential etching at the site of shear band and adjacent regions is presented in three dimensions in Figures 4.45 to 4.47. The uneven surface roughness shows densely packed mass in the regions of shear band than in the adjacent regions. The location containing shear bands is marked by hardness indentation and followed by removal of the etching layer using polishing with 30nm colloidal silica solution. The specimen is again studied under AFM at regions of ASB and adjacent regions with no shear bands. From Figures 4.48 to 4.51 features of the microstructure in the regions inside and outside the adiabatic shear bands are observed. Each scan is performed by selecting a region from100μm x 100μm to 5μm x 5μm area. Further analysis is discussed in Chapter 5.

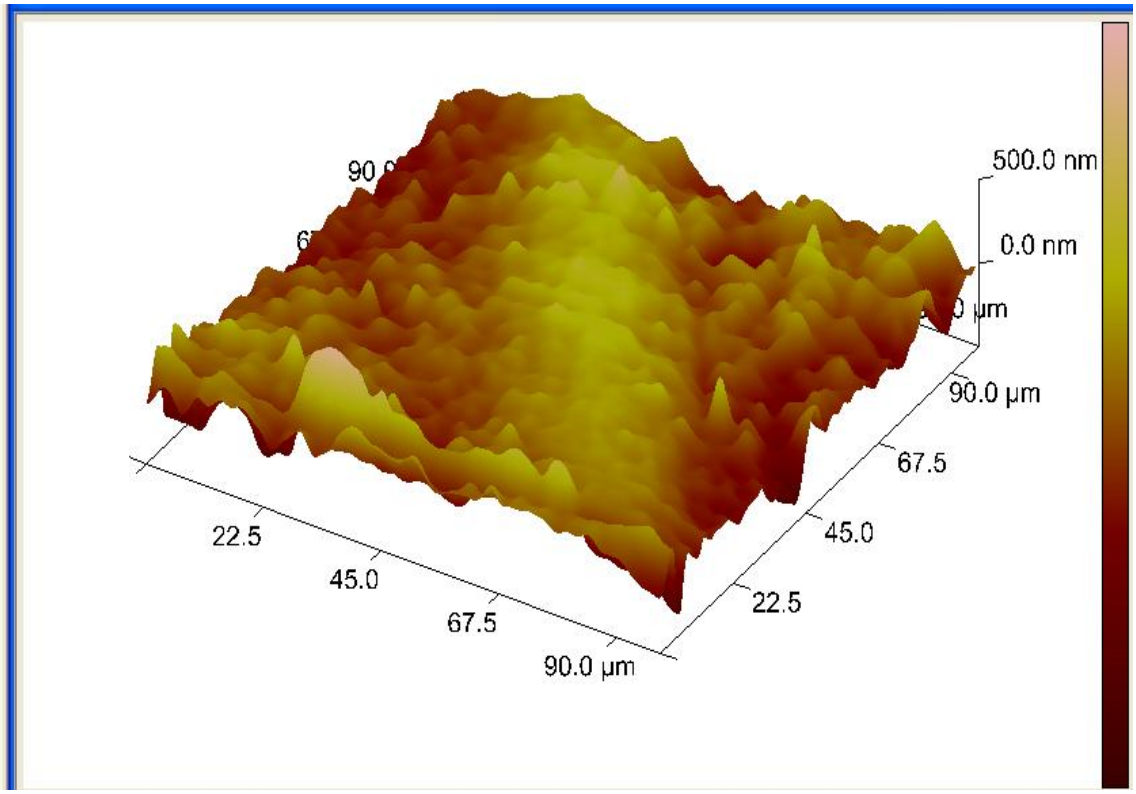

Figure 4.45: A 3-dimensional surface view on the white-etching band region in Mars 300

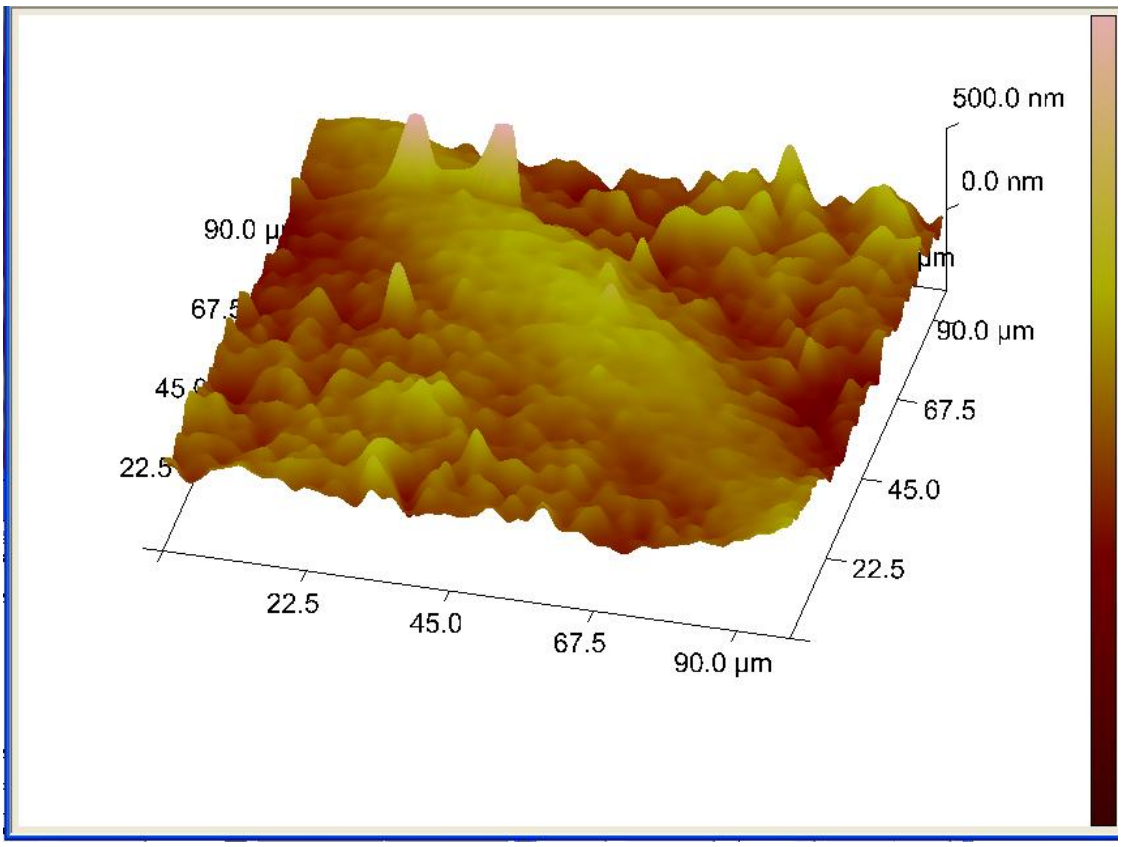

Figure 4.46: A 3-dimensional surface view on the white-etching band region in Mars 300

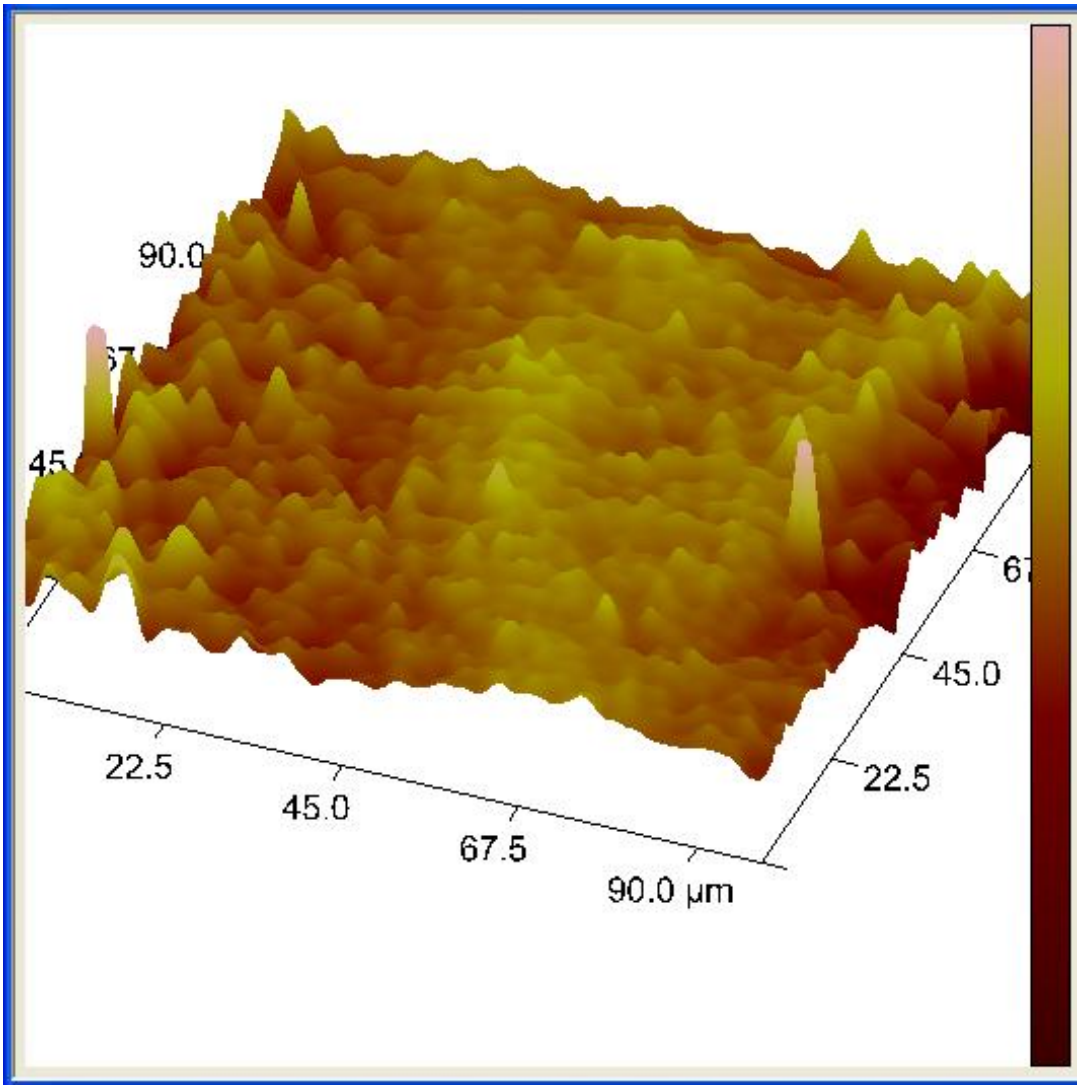

Figure 4.47: A 3-dimensional surface view on the deformed band region in Mars 300

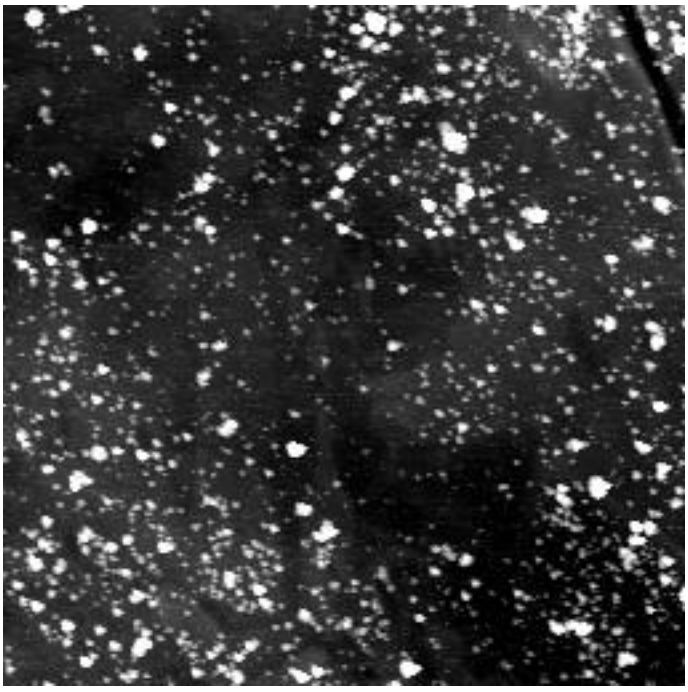

Figure 4.48: Region inside the white-etching bands (scan size 10μm x 10μm)

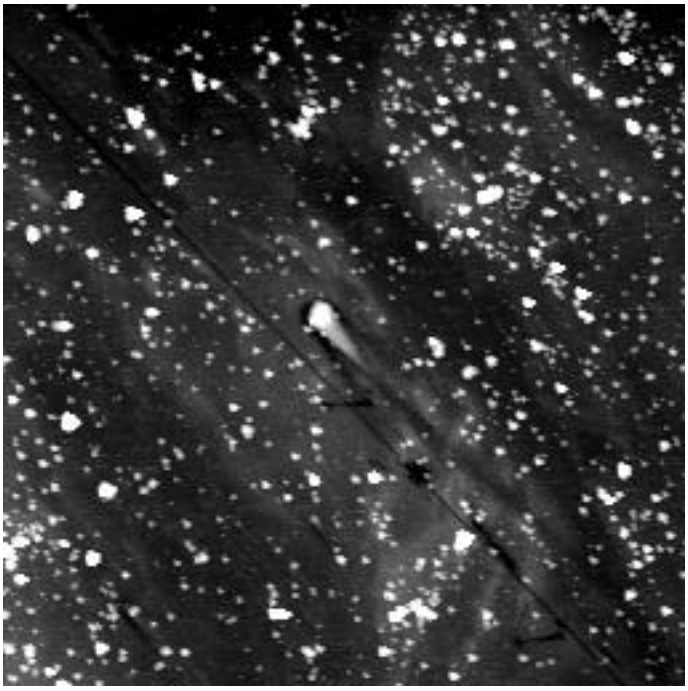

Figure 4.49: Region inside the white-etching bands (scan size 10μm x 10μm)

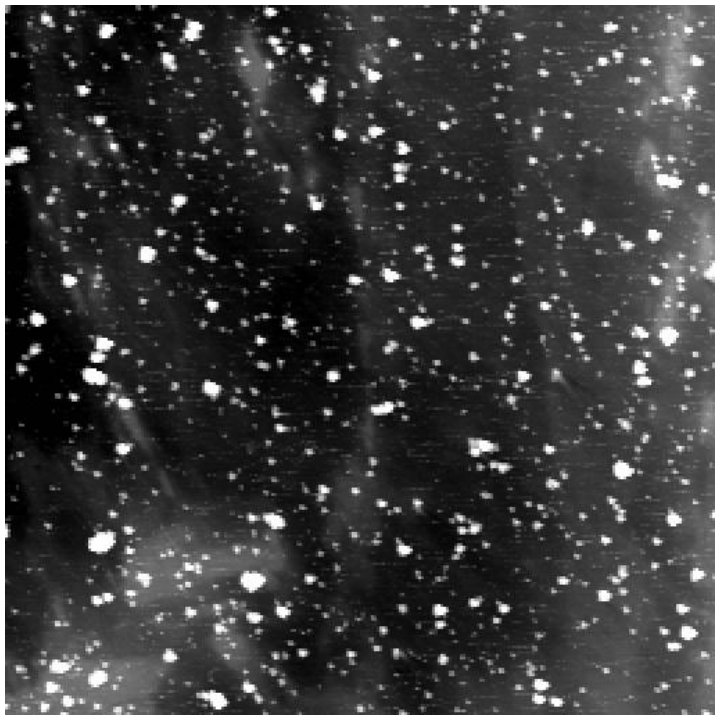

Figure 4.50: Region outside the shear bands (scan size 10μm x 10μm)

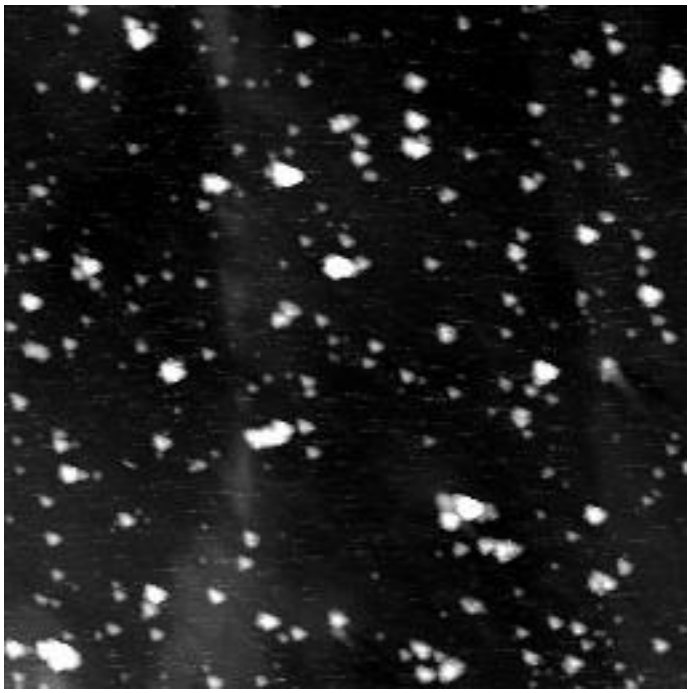

Figure 4.51: Region outside the shear bands (scan size 5μm x 5μm)

4.6 Microstructural Investigation using Scanning Electron Microscopy (SEM)

An analysis of the fractured surface of HHA sample was performed using Scanning Electron Microscopy (SEM). Although Mars 300 samples fractured at impact momentums above 46 kg.m/s, the two halves of the samples were fused due to the rapid heat generated during impact. As shown in Figure 4.52, the HHA samples fractured into two pieces and the following images show the shape of a cone in the propagation of fracture.

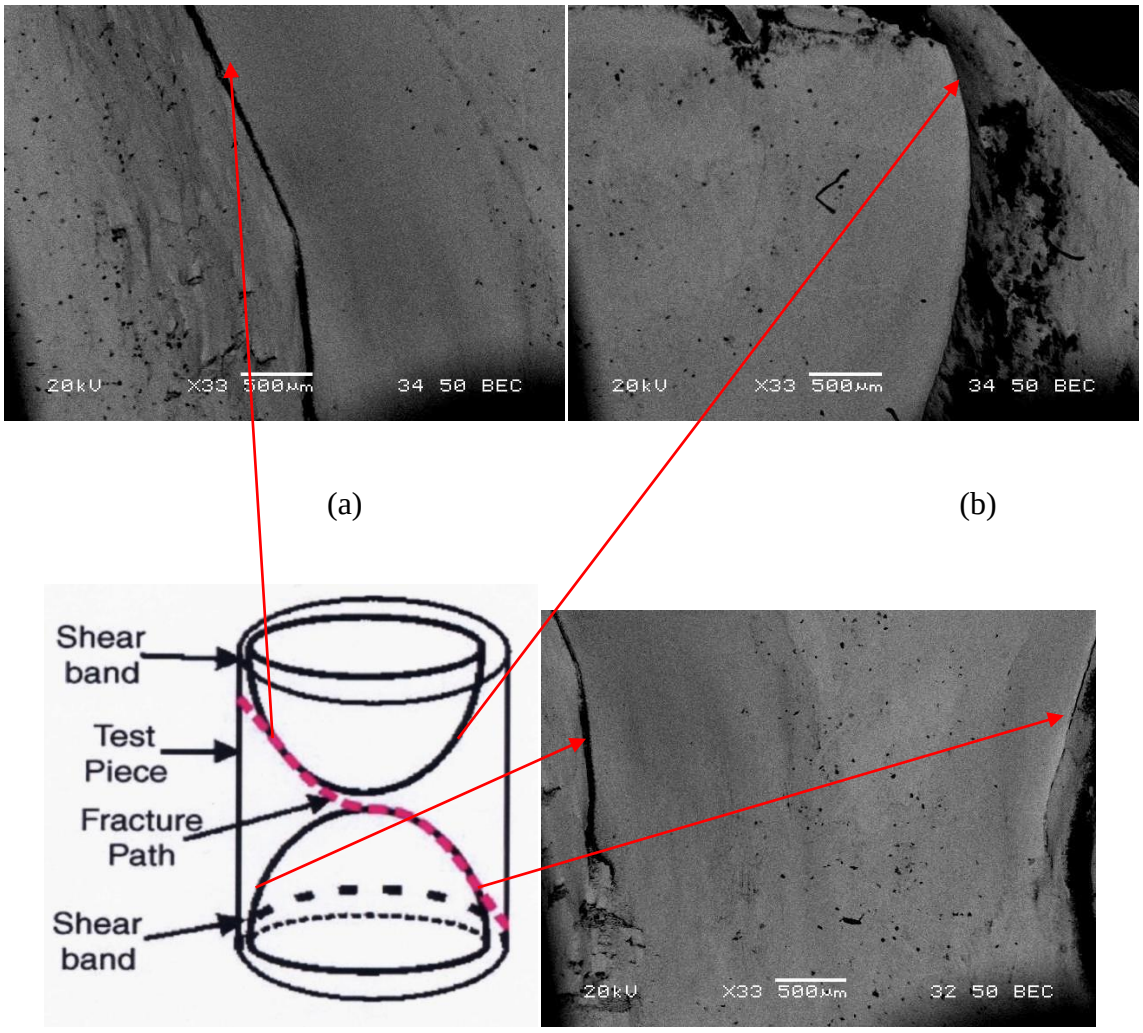

Figure 4.52: The fracture path in HHA specimen subjected to impact loading. Images (a and b) showing the top cone. Image (c) showing the propagation of fracture along the cone (Odeshi, Al-Ameeri and Mirfakhraei, et al. 2006). Image (d) showing the cone at the lower part of the specimen.

CHAPTER FIVE: DISCUSSION

5.1 Discussion of Stress-Strain Curves for Impact Loading

5.1.1 Steel specimens – Maraging Steel 300 and High Hardness Armor

The results of the high strain-rate investigation of Maraging steel 300 (Mars 300), High Hardness Armor (HHA) Steel and Aluminum 5083-H131 Alloy show that plastic deformation at high strain rate is dominated by intense shear strain localisation along Adiabatic Shear Bands (ASBs). The occurrence of ASB is traced to extreme localised heating and the associated thermal softening from high strain-rate impact or torsion loading. The heat is trapped in a localised region and is not conducted away generating a near-adiabatic condition in the materials during shock loading. Thermo-mechanical instability occurs in the microstructure as a result of the dominating effect of thermal softening over strain hardening. The microstructural imperfections caused by the occurrence of adiabatic shear bands eventually lead to failure of the material.

The results from the direct impact experiments are presented in Table 4.1 and Figures 4.1 to 4.6 shows the stress-strain curves of the tested samples with respect to impact momentum. A relationship between the firing pressure of the gun and the impact momentum of the projectile has been established in previous experiments (Mirfakhraei 2008). The values of impact momentum with respect to firing pressure and time taken for projectile to travel are presented in Table 3.1. Typical stress-strain curves for Mars 300 and HHA samples investigated using the Split Hopkinson Pressure Bar – Direct Impact (SHPB) are shown in Figures 4.1 and 4.2. From the stress-strain curves, it is clear that the flow stresses increases rapidly at low strain for both Mars 300 and HHA. It is also

evident that the range of plastic deformation occurs at low strains and the flow stress reaches the maximum stress rapidly. In this region, strain hardening is dominant during plastic deformation. The energy from the high velocity impact of the projectile is transferred as thermal energy to the specimen. Past the maximum stress the effect of strain hardening is outweighed by the effect of thermal softening and the latter dominates the deformation leading to stress collapse as observed in the stress-strain curves.

The sharp v-shaped fluctuation in the flow stress of Mars 300 and HHA at the yield point could be attributed to the yield-point phenomenon. The flow stress increases gradually with increasing elastic strain, fluctuates suddenly and then increases with increasing strain. The yield point has been associated with small amounts of interstitial impurities such as carbon and nitrogen (Dieter 1976).

Microscopic examination revealed that Mars 300 specimens subjected to an impact momentum of 32.91 kg.m/s and 40.04 kg.m/s did not show any ASBs. An optically magnified image from Figure 4.23 (a, b) shows the presence of needle-like particles in the microstructure of Mars 300. These needle-like particles are martensitic structures and are typically present in quench hardened steels. Increasing the impact momentum to 44.54 kg.m/s revealed the presence of ASB in Mars 300. The etching agent, Nital, attacks the surface to show the microstructure comprising of grain boundaries and imperfections. Figures 4.24 and 4.25 shows the initiation site of the deformed band and continuation of shear band as a white etching band. Transmission Electron Microscopy (TEM) studies on the white ASB by Wingrove (1971) showed high density of dislocations with some cell boundaries. The appearance of the white etching (transformed) band is attributed to the phase transformation occurring as a result of

localised heating. Glenn and Leslie (1971) have mentioned that the appearance of white colour is due to the formation of austenite during the localised adiabatic heating that is subsequently transformed to untempered martensite.

Detailed microstructural analysis using Atomic Force Microscopy (AFM) on the shear bands in Mars 300 revealed an elevated densely packed matter in the region of white-etching band (Figures 4.45 and 4.46). The elevation in height is approximately to the order of 200 – 300 nm whereas the adjacent regions had a certain surface roughness below 100 nm. On the other hand, AFM scans on the deformed band region showed the densely packed matter spread over a width of 45 μm and not elevated with its surroundings (Figure 4.47). From the topographical study using AFM, it is clear that the region of white-etching bands appears close packed with large groups of atoms and elevated than its adjacent region. The release of internal stress causes the white-etching bands to appear higher than the surrounding region. Further investigation by removing the etching layer on the surface and studying the microstructure inside and outside the white-etching band revealed the presence of very fine white particles of approximately 100 – 200 nm in the white-etching band region. These very fine white particles had a higher incidence in the region of white-etching band than the adjacent regions. A study by Meyers and Wittman (1990) that the appearance of white transformed bands in steel samples is due to presence of fine Fe_5C_2 Carbide particles and martensite laths and the dissolution of carbide changes the etching characteristics of the shear band. These fine particles could also be precipitates due to the phase transformation caused by impact from the high velocity projectile. It has also been reported by Chen et al. (2005) that

depending on the plate thickness that is struck by a projectile, a temperature rise of 1527 °C could be achieved in the localized zone of a target plate.

The relation between dislocation behaviour and yield-point phenomenon could be explained by the solute atom interaction. The strong elastic interaction in the impurity atmosphere (Carbon and Nitrogen) becomes saturated and condensed into a row of atoms along the core of the dislocation and leads to the formation of new dislocations (Dieter 1976). The dislocations released into the slip plane pile up at grain boundaries (Dieter 1976).

High strain-rate impact testing on HHA specimens also revealed ASB upon microscopic examination. Figures 4.28, 4.29 and 4.31 reveal the appearance of ASB as the impact momentum is increased in HHA specimens. As the impact energy increases, there is also a rapid increase in the thermal energy at the microstructural level in the sample. This causes a greater localised heating region which makes the appearance of ASB thicker when the impact momentum is increased from 32.91 kg.m/s to 45.49 kg.m/s. An increase in impact momentum above 46 kg.m/s resulted in fracture. It is evident that ASB acts as a precursor to failure through the spread of shear bands across the bulk of the material.

Based on the study of Mars 300 and HHA specimens under high strain rate investigation, it is evident that impact momentum is a major factor in the initiation of adiabatic shear bands. According to Bonnet-Lebouvier et al. (2002) there is a threshold impact momentum from which shear bands initiate and propagate. The minimum impact momentum required for the initiation of ASB in HHA samples was 32.91 kg.m/s and

subsequent increase in impact momentum resulted in the appearance of ASB to be more prominent. On the other hand, ASBs in the form of very clear transformed (white-etching) band and trace of deformed band was observed in Mars 300 specimen impact at 44.54 kg.m/s. A further increase in impact momentum above 46 kg.m/s resulted in fracture of Mars 300 and HHA specimens. For Mars 300, the strain rate produced from impact is not high enough to generate shear bands when the impact momentum is below 44.54 kg.m/s. Scanning Electron Microscopy (SEM) examination of fractured HHA specimen (Figures 4.52 to 4.54) shows the conical shape of the fracture path. The conical shape of the cavity is similar to that observed in previous high strain rate studies by Odeshi et al. (2006), and Mirfakhraei (2008). The presence of micro-cracks was observed on the fractured HHA surface and these micro-cracks could be initiation sites of failure when ASBs propagate in the material.

5.1.2 Aluminum 5083 – H131 Alloy specimens

Stress-strain curves of Aluminum 5083-H131 Alloy specimens investigated using the SHPB are presented in Figure 4.3. The presence of a large plastic deformation region before reaching the maximum flow stress is evident for the existence of ductility in aluminum. In comparison with steel specimens, aluminum had lower maximum flow stresses. These are due to the presence of larger plastic deformation region where strain hardening is more distinctive than in steels.

Figures 4.4 and 4.5 show the effect of impact momentum on strain rate and maximum flow stress respectively. Aluminum 5083 – H131 Alloy had higher strain rates

than Mars 300 or HHA. The effect of impact momentum on maximum flow stress is different for Aluminum 5083 – H131 Alloy than for the steel samples. The initial increase of the stress-strain curve to reach the maximum stresses is affected by the increase in impact momentum. As the impact momentum is increased from 30 to 45 kg.m/s for Mars 300 specimens, the maximum flow stress increases slightly. For HHA specimens, the maximum flow stress remains constant between impact momentum of 30 and 40 kg.m/s but decreases beyond 45 kg.m/s. The occurrence of ASB is due to the domination of thermal softening effects over strain hardening that eventually leads to a decrease in maximum flow stress. In general, for both Mars 300 and HHA, increasing the impact momentum above 45 kg.m/s would result in a decrease in the maximum flow stresses and subsequent fracture. However, Aluminum 5083 – H131 alloys behave differently as the maximum flow stress remains fairly constant with an increase in impact momentum. This is because the strain hardening effects are negated by the effects of thermal softening and the occurrence of ASB. Therefore, the combined mechanism of adiabatic heating and occurrence of ASB in Aluminum 5083 – H131 Alloys is influenced by plastic deformation.

Microscopic examination of Aluminum 5083 – H131 Alloys subjected to high strain rate impact testing reveals the appearance of ASBs. Figures 4.33 to 4.35 shows the appearance of shear bands as deformed bands near the edge of the specimen. As the impact momentum is increased, shear bands appear thicker (Figures 4.36 and 4.37). It is worth mentioning that metals with high stacking fault energies such as Aluminum (200 erg/ cm^2) deforms more readily by the mechanism of cross slip (Dieter 1976). A common characteristic of FCC materials such as aluminum is the tendency of the material to

exhibit more plastic flow than the other two types of materials at the same impact momentum investigated in this thesis. The strain hardening effects are highly significant that causes slip on several slip system leading to lattice irregularities (Dieter 1976). Therefore, multiple slips at grain boundaries results in pile-up of dislocations and affect grain orientation. The fact that different slip systems operating in adjacent regions of the same grain result in complex rotations leading to the formation of deformation bands (Dieter 1976). The reorientation of grains perpendicular to the direction of applied stress (Figure 4.33 to 4.37), shows that the mechanism of stacking fault energy contributes to the formation of ASB in Aluminum 5083 – H131 Alloy. This work is in agreement with the work of Mirfakhraei (2008) in the finding of ASB in Aluminum 5083 – H131 Alloy for all range of applied impact momentum.

From the direct impact experiments on Mars 300 and HHA materials, it is now clear that formation of ASBs leads to fracture at very high impact momentums (above 46 kg.m/s). The initiation of ASB is dependent on the material and the impact momentum for the investigated samples. This study reveals that Mars 300 requires a very high strain rate (due to high velocity impact) for the occurrence of ASB whereas deformed bands were found at lower impact momentum in HHA specimens. Therefore, BCC materials (Mars 300 and HHA), are dependent on impact momentum and temperature rise due to strain localization for the formation of ASB. On the other hand, Aluminum 5083 – H131 Alloy when undergoing plastic deformation, forms ASB due to the mechanism of strain hardening which in turn is dependent on the stacking fault energy in FCC materials.

5.2 Discussion of Stress-Strain Curves for Torsion Loading

5.2.1 Aluminum 5083 – H131 Alloy specimens

Aluminum 5083 – H131 Alloy specimens were subjected to torsion loading using a Torsional Split Hopkinson Bar (TSHB). Typical stress-strain curves for the aluminum alloy subjected to 6°, 4° and 8° angle of twisting are presented in Figures 4.7 to 4.9. The maximum flow stresses for Aluminum at 4° and 6° angle of twisting were in the range of 998 – 1051 MPa and 1078 – 1181 MPa respectively. This shows that there is a marginal increase in the maximum flow stresses when the angle is increased by 2°. However, aluminum specimens subjected to 8° angle of twisting had maximum flow stresses in the range of 1096 – 1143 MPa. The experimental results show that the change in the angle of twist from 6° to 8° angle of twisting had no effect on the maximum flow stresses. From referring to Table 4.2 and observing stress-strain curves, it can be seen that the flow stress and strain increases with an increase in the applied angle of twist. The range of strains for adiabatic heating increases as the angle of twist is increased and so does stress collapse occur at large strains. Figures 4.14 and 4.15 show the effect of applied angle of twist on maximum strain rate and maximum shear stress. In comparison with impact loading experiments, aluminum samples subjected to torsion experiments did not show the presence of yield-point phenomenon in the stress-strain curves. The flow stress had a gradual transition into plastic deformation. It should also be noted that the maximum flow stresses for compression samples were significantly lower than torsion samples. This could be due to experimental error when the applied torque for a particular angle of twist is affected by minor slip in incident bar.

Microscopic examination reveals that aluminum specimens subjected to 8° angle of twisting showed the presence of Adiabatic Shear Bands (ASBs) at the thin-walled tube sections of the hexagonal shaped specimen. The reorientation of grains at the thin-walled tube sections of the specimen can be clearly seen from Figures 4.38 and 4.39. The longitudinally aligned grains at thick segments of the specimen are forced to change direction at the thin segments of the specimen under the influence of a torsion load. At the other end of the cross section of the hexagonal specimen as seen from Figures 4.40 and 4.41, fracture occurs at the thin sections of the specimen. These images reveal that fracture or failure of material across the thin-walled tube sections occurs when the deformed bands are in the same direction of the large applied stress. The complexity between the effects of strain hardening and thermal softening leads to thermo-mechanical instability of the material. Armstrong and Zerilli (1994) suggested that a dislocation pile up due to softening and local rise in temperature can cut through a grain boundary and creates a site for shear band initiation and propagation. Figure 4.42 shows the crack initiation site in Aluminum 5083 – H131 Alloy specimen. As discussed in this section on the formation of ASB in Aluminum 5083 – H131 Alloy during impact loading, the significance of strain hardening results in dislocations multiplication. Interactions by cross-slip and dislocation multiplication within the grains occur sooner in high stacking fault materials (Murr, et al. 2002) such as aluminum. At high strain rate, the grains become distorted due to the applied angle of twist. The strain rate at 8° angle of twist is large enough to initiate a crack which propagates through the thin-walled tube specimen.

5.2.2 Maraging steel 300 (Mars 300) specimens

Typical stress-strain curves for Mars 300 at 6°, 4° and 8° angle of twisting are shown in Figures 4.10 to 4.12. The maximum shear flow stresses for Mars 300 were in the range of 1200 – 1400 MPa. In this case, the flow stress reaches the maximum stress at very low strains for Mars 300 specimens due to the visible short range of plastic deformation. The gradual decrease in flow stress during the range of adiabatic heating is due to the effects of thermal softening that reduces the flow stresses until stress collapse occurs. The maximum shear stresses for Mars 300 were higher than Aluminum 5083 – H131 Alloy specimens.

Figures 4.43 and 4.44 show the thin-walled tube sections of Mars 300 that failed at 6° angle of twisting. Microscopic investigation of Mars 300 specimens subjected to torsion loading showed fracture at the thin sections for specimens at 6° and 8° angle of twisting. There was no presence of ASB in Mars 300 at 4° angle of twisting. From this experiment, it is clear that the strain rates produced and the temperature rise during torsion experiments were not high enough to generate adiabatic shear bands. In the context of dislocation theory, strain hardening causes multiple dislocations to be accumulated at the grain boundary interface. These dislocation pile-ups increase the reorientation of grains in a plane leading to the observed grain rotation in Aluminum 5083 – H131 Alloy specimens investigated in TSHB.

Based on the study by Mercier and Molinari (1997) and Wright (2003), the tendency to form ASB's occurs more readily in materials with low strain rate sensitivity than high strain rate sensitivity. From torsion loading experiments and the use of Shen et al. (2006) to calculate strain rate sensitivity, it was found that the strain rate sensitivity for

Mars 300 was lower than Aluminum 5083 – H131 Alloy (refer Table 4.3) specimens. It was also reported that low strain rate sensitivity causes the formation of ASB in tungsten alloy (Kim, Lee and Baek 1998). Though, the strain rate sensitivity was lower in Mars 300, fracture of sample could not be traced to the presence of ASB. Thus a very high rise in temperatures and strain rate are required to initiate shear bands in Mars 300. Through stress-strain curves and microscopic investigation from torsion experiments, we could see that strain hardening at high strain rates contribute to the occurrence of ASBs in Aluminum 5083 – H131 Alloy. In conclusion for torsion loading experiments, Aluminum 5083 – H131 Alloy depends on the mechanism of strain hardening for the formation of ASBs but the lack of high temperatures and strain rates could be a factor for the absence of ASB in Mars 300 before the occurrence of fracture.

This research shows the significance of high strain rate in the use of armor materials. The dislocation mechanisms play a major role in the formation of ASB in Maraging steel 300, High Hardness Armor and Aluminum 5083 – H131 Alloy. The concept of stacking fault energy in FCC materials such as Aluminum 5083 – H131 Alloy contributes to strain hardening that in turn results in the formation of ASBs. On the other hand, Maraging steel 300 and HHA materials require a level of impact momentum to generate high temperatures and strain rates for the formation of ASBs. In all cases, the presence of ASBs is an undesirable phenomenon and consideration has to be taken for its occurrence in the design and use of such materials in armor plates.

CHAPTER SIX: CONCLUSIONS

The occurrence of ASBs in Maraging Steel 300, High Hardness Armor and Aluminum 5083 – H131 Alloy that are used as armor plates for combat vehicles is investigated. These materials were subjected to high strain rate using the Split Hopkinson Pressure Bar – Direct Impact and Torsional Split Hopkinson Bar to produce strain rates between 10^3 to 10^4 s^{-1}. The microstructural evolution as a result of high strain rate deformation is also investigated.

The following conclusions can be drawn from this investigation:

- The formation of ASBs is dependent on the type of material and impact momentum. The failure of these materials at high strain rates can be traced to the presence of ASBs.
- There are two types of ASBs formed as a result of high strain rate:
    - Deformed bands in Aluminum 5083 – H131 Alloy
    - Deformed bands in High Hardness Armor (HHA)
    - White-etching bands and deformed bands in Maraging Steel 300.
- Aluminum 5083-H131 Alloy exhibits deformed bands due to the plastic flow which in turn is based on the strain hardening in the material. The presence of large plastic deformation region in the stress-strain curves could be attributed to strain hardening.
- The deformed bands were present in HHA specimens for impact momentums between 32.91 kg.m/s and 45.49 kg.m/s.

- Maraging steel 300 requires a high impact momentum (44.54 kg.m/s) to generate ASB in the form of white-etching band and deformed band at its tail end.
- Investigation from the topographical study using AFM on the white-etching band in Maraging steel 300 suggests that the region of white-etching bands appears close packed with large groups of atoms and elevated than its adjacent region. The elevation in height of the white-etching band is due to the release of internal stress that causes the region to appear higher than the surrounding region.
- Both Maraging steel 300 and HHA specimens fractured at impact momentum above 46 kg.m/s.
- Maraging steel 300 and HHA behavior is dependent on impact momentum and temperature increase due to strain localization.
- The thin-walled tube sections of the hexagonal Maraging steel 300 specimens subjected to torsion loading experiments fractured at 6° angle of twisting. The fracture in the specimen could not be traced to the presence of ASBs. The strain rate produced and the local increase in temperature are not large enough to generate ASBs in torsion.
- The thin-walled tube sections of Aluminum 5083-H131 Alloy subjected to 8° angle of twisting showed deformed ASBs and subsequent fracture. The fracture at the other end of the specimen occurs when the deformed bands are in the same direction as the applied stress. The occurrence of ASBs is due to the mechanism of strain hardening which in turn is dependent on the stacking fault energy in FCC materials.

REFERENCES

Al-Ameeri, Sahar. "The effect of heat treatment on the adiabatic shear bands in AISI 4340 steel at high strain rate." M.Sc. Thesis, University of Manitoba, 2005.

Anand, L, and S. R. Kalinidi. "The process of shear band formation in plane strain compression of FCC metals: Effects of crystallographic texture." *Mechanics of Materials* 17 (1994): 223 - 243.

Armstrong, R. W., and F. J. Zerilli. "Dislocation mechanics aspects of plastic instability and shear banding." *Mechanics of Materials* 17 (1994): 319 - 327.

Bai, Y., and B. Dodd. *Adiabatic Shear Localization: Occurrence, Theories and Applications.* 1st Edition. 1992.

Bassim, M. N. "Study of the formation of adiabatic shear bands in steels." *Journal of Materials Processing Technology* 119 (2001): 234 - 236.

Bassim, M. N., A. G. Odeshi, S. Al-Ameeri, and Q. Li. "Dynamic shear band propagation and failure in AISI 4340 steel." *Journal of Materials Processing Technology* 169 (2005): 150 - 155.

Bassim, M. N., and A. G. Odeshi. "Microstructural Model for occurrence of Adiabatic Shear Bands." (AES-Advanced Engineering Solution) 2007.

Bonnet-Lebouvier, A. S., A. Molinari, and P. Lipinski. "Analysis of dynamic propagation of adiabatic shear bands." *International Journal of Solids and Structures* 39 (2002): 4249 - 4269.

Callister, William D. *Materials Science and Engineering An Introduction.* Sixth Edition. John Wiley & Sons, Inc., 2003.

Campagne, L., L. Daridon, and S. Ahzi. "A Physically Based Model for Dynamic Failure in Ductile Metals." *Mechanics of Materials* 37 (2005): 869 - 886.

Cepus, E. "Evolution of Adiabatic Shear Bands in High Strength Steels at High Shear-Strain Rates." M. Sc. Thesis, University of Manitoba, 1995.

Chen, X. W., Q. M. Li, and S. C. Fan. "Initiation of adiabatic shear failure in a clamped circular plate struck by a blunt projectile." *International Journal of Impact Engineering* 31 (2005): 877 - 893.

Dao, K. C., and D. A. Schockey. "A method for measuring shear band temperature." *Journal of Applied Physics* 50 (1979): 8244.

Derep, J. L. "Microstructure transformation induced by adiabatic shearing in armored steel." *Acta Metal* 35 (1987): 1245 - 1249.

Dieter, G. E. *Mechanical Metallurgy.* 2nd Edition. McGraw-Hill, Inc., 1976.

"Dimension 3100 Manual." Vol. Version 4.43C. Digital Instruments, Veeco Metrology Group, 2003.

Feng, H., and M. N. Bassim. "Finite element modelling of the formation of adiabatic shear bands in AISI 4340 steel." *Materials Science and Engineering* A266 (1999): 255 - 260.

Glenn, R. C., and W. C. Leslie. "The nature of "White Streaks" in impacted armor steel plate." *Metallurgical Transactions* 2 (1971): 2945 - 2947.

Hartley, A., J. Duffy, and R. H. Hawley. *Journal of Mechanics and Physics of Solids* 35 (1987): 283 - 301.

Kim, Dong-kuk, Sunghak Lee, and Woon Hyung Baek. "Microstructural study of adiabatic shear bands formed by high-speed impact in a tungsten heavy alloy penetrator." *Materials Science and Engineering* A249 (1998): 197 - 205.

Lach, E., and H. Nahme. "Dynamic Behaviour of High Strength Armor Steels." *J. Phys IV France* 7 (1997).

Li, S. X., R. Q. Yang, J. W. Li, and Z. F. Zhang. "Shear Localization in Dynamic Deformation of Copper Single Crystals." *Philosophical Magazine*, 2006: 5769 - 5786.

Marchand, A., and J. Duffy. "An Experimental Study of the Formation Process of Adiabatic Shear Bands in a Structural Steel." *Journal of Mechanics and Physics of Solids* 36 (1988): 251 - 283.

Mechanical Testing and Evaluation. Vol. 8, in *ASM Handbook*, 505 - 515. American Society for Metals International, 2000.

Mercier, S., and A. Molinari. "Role of Rate Effects and of Thermomechanical Coupling in Shear Localization." *Transactions of the ASME*, 1997: 322 - 331.

Meyers, M. A., and C. L. Wittman. "The effect of metallurgical parameters on shear band formation in low carbon (~0.20 Pct) steels." *Metal Trans* 21A (1990): 3153 - 3164.

Meyers, M. A., X. Q. Xue, M. T. Perez-Prado, and T. R. Mcnelley. "Microstructural evolution in adiabatic shear band localization in stainless steel." *Acta Material* 51 (2003): 1307 - 1325.

Mirfakhraei, Sahar. "Deformation of high strength alloys at high strain rates." M. Sc. Thesis, University of Manitoba, 2008.

Mishra, A., V. Richard, F. Gregori, R. J. Asaro, and M. A. Meyers. "Microstructural evolution in copper processed by severe plastic deformation." *Journal of Material Science and Engineering* A 410 - 411 (2005): 290 - 298.

Murr, L. E., E. A. Trillo, S. Pappu, and C. Kennedy. "Adiabatic shear bands and examples of their role in severe plastic deformation." *Journal of Materials Science* 37 (2002): 3337 - 3360.

Nesterenko, V. F., M. A. Meyers, and T. W. Wright. "Self Organization in the Initiation of Adiabatic Shear Bands." *Acta Materialia* 46 (1998): 327 - 340.

Odeshi, A. G., S. Al-Ameeri, and M. N. Bassim. "Effect of high strain rate on plastic deformation of a low alloy steel subjected to ballistic impact." *Materials Processing Technology* 162 (2005): 385 - 391.

Odeshi, A. G., S. Al-Ameeri, S. Mirfakhraei, F. Yazdani, and M. N. Bassim. "Deformation and failure mechanism in AISI 4340 steel under ballistic impact." *Theoretical and Applied Fracture Mechanics* 45 (2006): 18 - 24.

Peirce, D., R. J. Asaro, and A. Needleman. "Material rate dependence and localized deformation in crystalline solids." *Acta Metallurgica* 31 (1984): 1951 - 1976.

Schoenfeld, S. E., and T. W. Wright. "A failure criterion based on material instability." *International Journal of Solids and Structures* 40 (2003): 3021 - 3037.

Shen, Y. F., L. Lu, M. Dao, and S. Suresh. "Strain Rate Sensitivity of Cu With Nanoscale Twins." *Scripta Materialia* 55 (2006): 319 - 322.

Vecchio, Kenneth S, and Richard W. Hertzberg. "The influence of stacking fault energy on ductile fracture micromorphology." *Journal of Materials Science* 23 (1988): 2220 - 2224.

Wingrove, A. L. "A Note on the Structure of Adiabatic Shear Bands in Steel." *The Journal of the Australian Institute of Metals* 16, no. No. 1 (1971): 67 - 70.

Wright, T. W. "On the Speed of an Unconstrained Shear Band in a Perfectly Plastic Material." *International Journal of Solid and Structures* 40 (2003): 871 - 879.

Wright, T. W. "Steady shearing in a viscoplastic solid." *Journal of Mechanics and Physics of Solids* 35 (1987): 269 - 282.

Wright, T. W., and J. W. Walter. "On stress collapse in adiabatic shear bands." *Journal of Mechanics and Physics of Solids* 35 (1987): 701 - 720.

Xue, Q., V. F. Nesterenko, and M. A. Meyers. "Self organization of shear bands in titanium and Ti-6Al-4V alloy." *Acta Materialia* 50 (2002): 575 - 596.

Zener, C., and J. H. Hollomon. "Effect of strain rate upon plastic flow of steel." *Journal of Applied Physics* 15 (1944): 22 - 32.

Zhang, B., W. Shen, Y. Liu, and R. Zhang. "Some factors influencing adiabatic shear banding in impact wear." *Wear* 214 (1998): 259 - 263.

Zurek, A. K. "The study of adiabatic shear bands instability in pearlitic 4340 steel using a dynamic punch test." *Metallurgical and Materials Transactions* 25A (1994): 2483 - 2489.